APPLIED PHYSICS

1`25

ПРИКЛАДНАЯ ФИЗИКА



APPLIED PHYSICS

THE SCIENTIFIC AND TECHNICAL JOURNAL

2025, No. 1	Founded in 1994	Moscow	
	CONTENTS		
GENERAL PHYSICS			
Telegin A. M., Kalaev M. P. and Voro Study of calculation of the induced cur	nov K. E. rent pulse in the measuring grids of a micrometeoroid and space debris ser	nsor 5	
PLA	SMA PHYSICS AND PLASMA METHODS		
9	ev A. A., Poluyanova I. N. and Shkolnik S. M.		
	rrent vacuum arc with copper electrodes	11	
Zolotukhin D. B., Shandrikov M. V. and Ionic composition of the planar magne	tron plasma in gas and vacuum operation mode	16	
-	olotukhin D. B., Klimkin T. O., Nesterenko A. K., Salnikov S. A.	and	
Yushkov Yu. G.			
	position on the mass-to-charge composition of ions in the beam plasma du	_	
the evaporation of an YSZ target by an Panov V. A., Saveliev A. S. and Kuliko		24	
	n the development of pre-breakdown currents in distilled water	31	
	PHOTOELECTRONICS		
Boltar K. O., Burlakov I. D., Iakovl Permikina E. V., Voitsekhovskii A. V.,	eva N. I., Sednev M. V., Trukhachev A. V., Irodov N. A., Lopukhin A	1. A.,	
	IgTe <i>n</i> B <i>n</i> -architecture with superlattice barrier layer	38	
Ponomarenko V. P., Popov V. S., Par Dragunov D. E., Epifanov O. V., Burlakov I. D., Polessky A. V., Start	okov M. A., Khamidullin K. A., Deomidov A. D., Fedorov A. A., Deev G. Lazarev P. S., Mirofyanchenko E. V., Ilyinov D. V., Petrushina V tsev V. V., Brichkin S. B., Spirin M. G., Tovstun S. A., Gapanovich M. ov D. N., Katsaba A. V., Kirichenko A. S., Demkin D. V., Ivanova V	V. A., I. V.,	
Uncooled 640×512 photosensor array	for the spectral range of 0.4–2.0 μm from colloidal quantum dots PbS $\ w$	ith a	
hole transport layer based on <i>p</i> -PbS-EI		45	
Photomermistic switchings in bismuth	Borisenko D. N. and Kolesnikov N. N. selenide crystals	55	
Lopukhin A. A., Permikina E. V., Bary	•		
Characteristics of small-format matrix		60	
Shuklov I. A., Dyomkin D. V. and Vers		64	
Synthesis of colloidal quantum dots of <i>Gruzevich Yu. K., Alkov P. S., Balyasn</i>		64	
•	cal-television underwater imaging systems	70	
	PHYSICAL SCIENCE OF MATERIALS		
Likhomanova S. V. and Kamanina N. Mechanisms of interaction of polyviny	V. I alcohol molecules and carbon nanoparticles in aqueous solutions	78	
Rabadanova A. E., Gadzhimagome			
Murlieva Zh. Kh., Mayorov S. A., Rag		84	

ПРИКЛАДНАЯ ФИЗИКА®

НАУЧНО-ТЕХНИЧЕСКИЙ ЖУРНАЛ

2025, № 1	Основан в 1994 г.	Москва
	СОДЕРЖАНИЕ	
	ОБЩАЯ ФИЗИКА	
Телегин А. М., Калаев М. П., Вороно Исследование модели расчёта микрометеороидов и частиц космич	наведенного импульса тока в измерительных сетках датч	лика 5
ФИЗИ	КА ПЛАЗМЫ И ПЛАЗМЕННЫЕ МЕТОДЫ	
Баринов Ю. А., Забелло К. К., Логач	лев А. А., Полуянова И. Н., Школьник С. М. вакуумной дуги с медными электродами	11
Золотухин Д. Б., Шандриков М. В.,	**	16
Тюньков $A. B.$, A ндронов $A. A.$, G	Золотухин Д. Б., Климкин Т. О., Нестеренко А. К., Сальников С.	. A.,
Влияние состава рабочего газа на мишени электронным пучком	масс-зарядовый состав ионов пучковой плазмы при испарении У	YSZ 24
Панов В. А., Савельев А. С., Куликов Эффект глубины погружения электр	s HO. M. рода на развитие предпробойных течений в дистиллированной воде	31
	ФОТОЭЛЕКТРОНИКА	
Пермикина Е. В., Войцеховский А. В Матричное фотоприемное устройс CdHgTe с барьерным слоем на основ Пономаренко В. П., Попов В. С., Па Драгунов Д. Э., Епифанов О. В., Бурлаков И. Д., Полесский А. В.,	овлева Н. И., Седнев М. В., Трухачев А. В., Иродов Н. А., Лопухин А., Горн Д. И., Михайлов Н. Н. ство средневолнового ИК диапазона спектра с пВп-архитектурой ве сверхрешетки нков М. А., Хамидуллин К. А., Деомидов А. Д., Федоров А. А., Деев Г Пазарев П. С., Мирофянченко Е. В., Ильинов Д. В., Петрушина В. Старцев В. В., Бричкин С. Б., Спирин М. Г., Товстун С. иская А. В., Певцов Д. Н., Кацаба А. В., Кириченко А. С., Дёмкин Д.	38 Ю., . А., . А.,
точек ККТ PbS с транспортным слое	нсор $640{\times}512$ для области спектра $0,4{-}2,0$ мкм из коллоидных квантогем для дырок на основе ККТ $p ext{-PbS-EDT}$	вых 45
Зотов А. В., Панин Γ . Н., Тулина Н. Фотомемристивные переключения в	А., Борисенко Д. Н., Колесников Н. Н. в кристаллах селенила висмута	55
Лопухин А. А., Пермикина Е. В., Бар	ьшева К. В., Гришина А. H.	
Характеристики малоформатных ма Шуклов И. А., Дёмкин Д. В., Вершин		60
синтез коллоидных квантовых точен	с сульфида свинца в децене-1 в качестве растворителя	64
Грузевич Ю. К., Альков П. С., Баляс. Гибридный фотоприемный модуль д	ныи Л. М., Волков Д. В. для оптико-телевизионных систем подводного видения	70
Φ	ИЗИЧЕСКОЕ МАТЕРИАЛОВЕДЕНИЕ	
Лихоманова С. В., Каманина Н. В.	, .	
Рабаданова А. Э., Гаджимагом	* *	
Мурлиева Ж. Х., Майоров С. А., Раго Сверхпроводящая микрокристаллич	имханов Г. Б., Эмиров Р. М. еская керамика YBCO: корреляции структуры и свойств	84

GENERAL PHYSICS

UDC 621.3 EDN: ZGZNQM

PACS: 07.05.Dz, 07.55. Jg, 94.80.+g

Study of calculation of the induced current pulse in the measuring grids of a micrometeoroid and space debris sensor

A. M. Telegin, M. P. Kalaev, K. E. Voronov

A formula is derived to calculate the induced current pulse excited by a grid-electrode during the charged microparticle flight. The data obtained can be used to analyze the velocity and microparticle entry angle into the grid sensor of high-speed microparticles.

Keywords: Micrometeoroids; space debris; Shockley-Ramo theorem; induced current; electrode.

DOI: 10.51368/1996-0948-2025-1-5-10

Introduction

One of the important tasks of space research is to track and characterize high-speed microparticles (micrometeoroids and space debris) [1–4]. Micron-sized particles are monitored using *in-situ* sensors, which are mounted directly on the spacecraft surface. Grid construction sensors [5, 6] are example of such sensors. They determine the velocity vector of high-speed microparticles by

measuring the induced charge on the grid-electrodes in proportion to the particle's velocity and electrical charge (Figs. 1, 2).

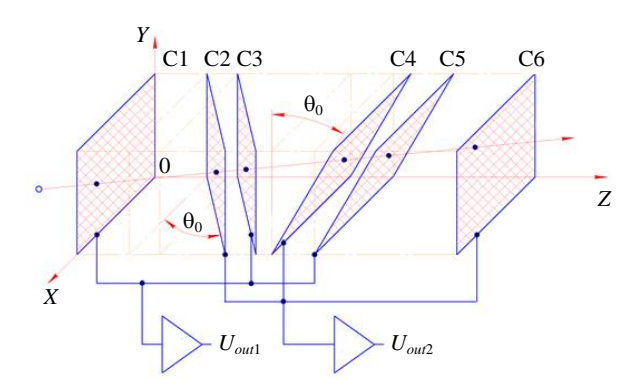


Fig. 1. Structure diagram of the grid sensor

Aleksey M. Telegin^{1,2}, Senior Staff Scientist,
Associate Professor, Candidate of Physical and
Mathematical Sciences
E-mail: talex85@mail.ru
Mikhail P. Kalaev^{1,2}, Senior Staff Scientist,
Associate Professor, Candidate of Technical Sciences
Konstantin E. Voronov^{1,2}, Director, Associate
Professor, Candidate of Technical Sciences
¹ Samara University, Space Instruments Engineering
Institute (IKP-214)
34a, Moscow highway, Samara, 443086 Russia
² Samara University
34, Moscow highway, Samara, 443086 Russia

Received July 30, 2024 Revised November 6, 2024 Accepted February 1, 2025 Scientific specialty code: 1.3.2



Fig. 2. Photograph of the grid construction sensor: C1, C2, C3, C4, C5, C6 – six grids are positioned as shown in Fig. 1

The authors developed and evaluated a prototype grid sensor (Figs. 1, 2), that consists of six grid measuring electrodes arranged in tilted pairs at different angles to measure three velocity vector projections $(\vec{V} = \vec{1}_x \cdot Vx + \vec{1}_y \cdot Vy + \vec{1}_z \cdot Vz$, where $\vec{1}_x$ – unitary vector on-axis 0X, \vec{l}_{v} – unitary vector on-axis 0Y, $\vec{1}_{z}$ – unitary vector on-axis 0Z) of a microparticle (Fig. 1). To effectively design devices based on the induced charge measurement, it is to understand the signal waveform from the measuring electrode. This knowledge is crucial for developing a processing method for the obtained experimental data [7-9]. Previous research [10–12] established a method for estimating the induced current pulse in a plane-parallel capacitor. However, in the prototype we have developed, some grids are not arranged in parallel configuration.

In this paper, we analyzed the motion of a microparticle within a planar geometry, under the condition that the particle does not fly by the grid edges.

The objective was to determine the shape of the induced current pulse waveform of non-parallel measuring grids.

Model of induced current disregarding the influence of the input measuring circuit

Figure 3 shows the projections of two non-parallel planes angled θ_0 towards each other, corresponding to the first two grids of the sensor shown in Figures 1 and 2. A charged microparticle (a micrometeoroid or space debris) flies through the first measurement grid at point M0 (x0,0) and flies out the second grid at point M1(x1, z1). We define the intermediate position of the microparticle at time point t as point M(x, z).

Given the under study microparticle's velocity is much less than the electromagnetic wave velocity, we use the steady-state approximation of the Shockley-Ramo

theorem to determine the induced current pulse on the electrode [10–13]:

$$i(t) = Q \cdot (\vec{V} \cdot \vec{E}_k), \tag{1}$$

where \vec{E}_k is the effective (weighted) field intensity at the point of charge Q at time point t. It's calculated by removing the charge, setting the measuring electrode's potential to 1, setting the remaining electrode potentials to 0. $(\vec{V} \cdot \vec{E}_k)$ is the dot product of the velocity vector and effective strength.

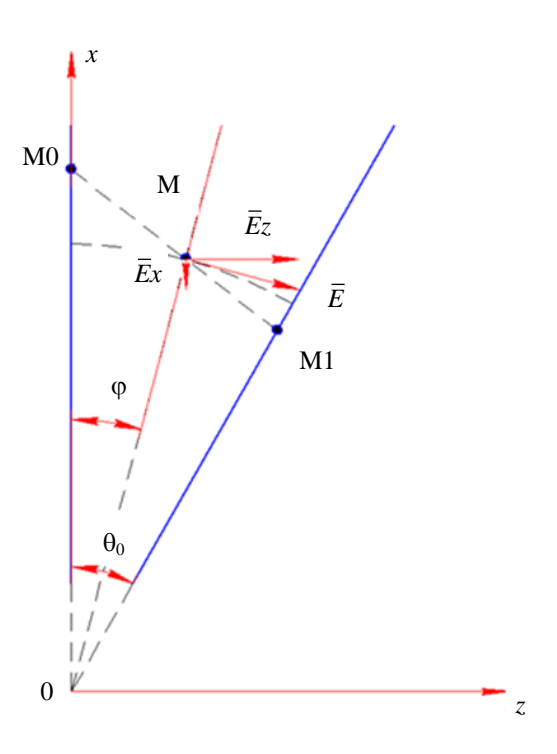


Fig. 3. Relative positions of inclined measuring grid electrodes

The electric field intensity between non-parallel plane electrodes can be calculated using the following formula in polar coordinate system [14]:

$$E = \frac{U}{r \cdot \theta_0},\tag{2}$$

where U is the voltage across the measuring electrode (assumed to be 1V), r is the distance from point 0 to point M, and θ_0 – is the angle between the two grid electrode planes.

We will assume that the first grid C1 is at 0 potential, and the signal is measured from the second grid C2.

The coordinates of a microparticle in the Cartesian coordinate system are calculated using formulas:

$$z = r \cdot \sin(\varphi), \quad x = r \cdot \cos(\varphi),$$
 (3)

$$x1 = x0 - Vx \cdot t, \quad z1 = Vz \cdot t. \tag{4}$$

Given
$$tg(\alpha) = \frac{Vx}{Vz}$$

the intensity vector projections Ex, Ez in the Cartesian coordinate system are calculated using formulas:

$$Ex = E \cdot \sin(\varphi), \quad Ez = E \cdot \cos(\varphi),$$

$$tg(\varphi) = \frac{z}{x} = \frac{Vz \cdot t}{x0 - Vx \cdot t} = \frac{t}{x0 / Vz - tg(\alpha) \cdot t}.$$
 (5)

The induced current according to the Shockley-Ramo theorem is calculated using formulas:

$$i = Q \cdot (\vec{V} \cdot \vec{E}) = Q \cdot (\vec{V}x \cdot \vec{E}x + \vec{V}z \cdot \vec{E}z) =$$

$$= \frac{U \cdot Q}{z \cdot \theta_0} (Vx \cdot \sin^2(\varphi) + Vz \cdot \cos(\varphi) \cdot \sin(\varphi)) =$$

$$= \frac{U \cdot Q}{\theta_0} \left(\frac{x0/Vz}{(x0/Vz - tg(\alpha) \cdot t)^2 + t^2} \right) =$$

$$= i(t = 0) \cdot \left(\frac{x0^2}{(x0 - tg(\alpha) \cdot t \cdot Vz)^2 + (t \cdot Vz)^2} \right),$$
(6)

where
$$i(t=0) = \frac{U \cdot Q}{\theta_0} \left(\frac{Vz}{x0}\right) = \frac{1 \cdot Q}{\theta_0} \left(\frac{Vz}{x0}\right)$$
 is the current at time point when the microparticle flies by the point M0.

The time of flight of the second grid C2 (at point M1) is determined by the solution of the of equation:

$$\begin{cases} x1 = x0 - Vx \cdot t_1, \\ z1 = Vz \cdot t_1, \\ tg\left(\theta_0\right) = \frac{z1}{x1}. \end{cases}$$
 (7)

The solution of the of equations presented is expressed as:

$$t_{1} = \frac{x0}{V_{Z} \cdot \left(\frac{1}{tg(\theta_{0})} + tg(\alpha)\right)}$$
(8)

where t_1 is the microparticle time of flight of the second grid C2.

The velocity vector component Vz can be determined by measuring the microparticle time of flight of C1 and C6 grids (Fig. 1) [5]. The velocity vector component Vx can be calculated using formula:

$$Vx = \frac{x0}{t_1} - \frac{Vz}{tg(\theta_0)}.$$
 (9)

Then the induced current at the microparticle time of flight of the second grid C2 can be calculated using formula:

$$i(t=t_{1}) = \frac{U \cdot Q}{\theta_{0}} \left(\frac{x0/Vz}{\left(\frac{1}{tg(\theta_{0})} + tg(\alpha)\right)^{2} + \left(\frac{x0/Vz}{\left(\frac{1}{tg(\theta_{0})} + tg(\alpha)\right)}\right)^{2} + \left(\frac{x0/Vz}{\left(\frac{1}{tg(\theta_{0})} + tg(\alpha)\right)^{2}}\right)^{2}} \right) = i(t=0) \cdot \left(\frac{\left(ctg(\theta_{0}) + tg(\alpha)\right)^{2}}{ctg^{2}(\theta_{0}) + 1} \right).$$

$$(10)$$

The entry angle of a microparticle into the first grid C1 can be calculated using formula:

$$tg(\alpha) = \sqrt{i(t=t1)\cdot(ctg^{2}(\theta_{0})+1)/i(t=0)} - \frac{1}{(11)}$$
$$-ctg(\theta_{0}).$$

At $\alpha = 0$ ($tg(\alpha) = 0$) we obtain a formula for the induced current at the moment of the microparticle passing the grid C2:

$$i(t=t_1) = i(t=0) \cdot \left(\frac{1}{1+tg^2(\theta_0)}\right) =$$

$$= i(t=0) \cdot \cos^2(\theta_0).$$
(12)

Given the microparticle's charge Q and velocity Vz, we can calculate the coordinate x0 of its passage through grid C1:

$$x0 = \frac{U \cdot Q}{\theta_0} \left(\frac{Vz}{i(t=0)} \right). \tag{13}$$

Model of induced current considering the influence of the input measuring circuit

High-speed microparticle sensors shall consider the impact of input measurement

circuit parameters like input capacity, amplifier resistance, and wiring parasitic inductance [12]. The differential equation derived from the radiotechnical model needs to be solved (Fig. 4) [10, 15]:

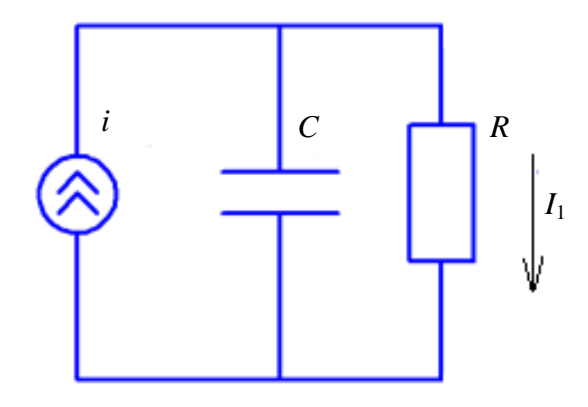


Fig. 4. A radiotechnical model of the input circuit: C – input capacity; R – input resistance

By solving the differential equation, we can determine the expression that describes the current I_1 , flowing through the input resistance [10, 12]:

$$C \cdot R \cdot \frac{dI_1}{dt} + I_1 = i. \tag{14}$$

To simplify the analytical solution of this differential equation, we will expand the induced current formula using Taylor's theorem and limit it to the first three terms of the series (the error of such approximation shall not exceed 0.5 %):

$$i = i(t = 0) \times$$

$$\times \left(1 + \frac{2 \cdot Vx}{x0} \cdot t + \left(3 \cdot \left(\frac{Vx}{x0}\right)^2 - \left(\frac{Vz}{x0}\right)^2\right) \cdot t^2\right) = (15)$$

$$= i(t = 0) \cdot \left(1 + A_1 \cdot t + A_2 \cdot t^2\right),$$

where
$$A_1 = \frac{2 \cdot Vx}{x0}$$
, $A_2 = \left(3 \cdot \left(\frac{Vx}{x0}\right)^2 - \left(\frac{Vz}{x0}\right)^2\right)$.

We will apply the initial time point during which the microparticle passes the first grid (C1), $I_1(t=0)=0$, when solving the differential equation. Therefore, the formula for the current flowing through the resistor is:

$$I_{1} = i\left(t = 0\right) \times \left[\left(1 - A_{1} \cdot \tau + 2 \cdot A_{2} \cdot \tau^{2}\right) \cdot \left(1 - e^{-t/\tau}\right) + \left[+\left(A_{1} - 2 \cdot \tau \cdot A_{2}\right) \cdot t + A_{2} \cdot t^{2}\right],\right],$$

$$(16)$$

where $\tau = R \cdot C$ is the input time constant.

At $\tau \to 0$ the formula changes to a formula disregarding the influence of the input measuring circuit. The presented formula can also be expanded using a Taylor's theorem, but only at $t/\tau <<1$, otherwise a sufficient number of terms of the series shall be included for accuracy.

Figs. 5, 6 show the dependency diagrams of current change in time. For convenience of analysis, we will plot the graph of the specified current and time functions coordinates:

$$I_{NORM1} = I_{1} / i(t = 0) =$$

$$= \begin{bmatrix} (1 - A_{1} \cdot \tau + 2 \cdot A_{2} \cdot \tau^{2}) \cdot (1 - e^{-t/\tau}) + \\ + (A_{1} - 2 \cdot \tau \cdot A_{2}) \cdot t + A_{2} \cdot t^{2} \end{bmatrix},$$
(17)

$$t_{norm} = t / t_1. \tag{18}$$

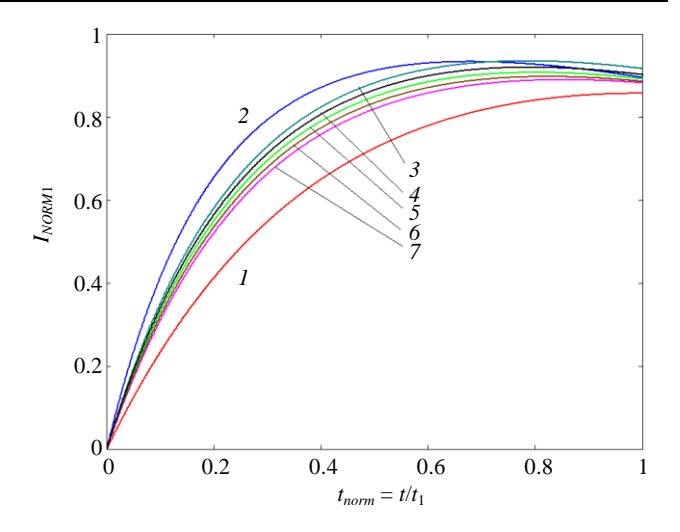


Fig. 5. The specified current pulse graph between the first and second grid at Vz = 1000 m/s, $\tau = 10^{-5}$ s: 1 - x0 = 0.1 m, $\alpha = 0$; 2 - x0 = 0.2 m, $\alpha = 0$; 3 - x0 = 0.15 m, $\alpha = -10^{\circ}$; 4 - x0 = 0.15 m, $\alpha = -5^{\circ}$; 5 - x0 = 0.15 m, $\alpha = 0^{\circ}$; 6 - x0 = 0.15 m, $\alpha = 5^{\circ}$; 7 - x0 = 0.15 m, $\alpha = 10^{\circ}$

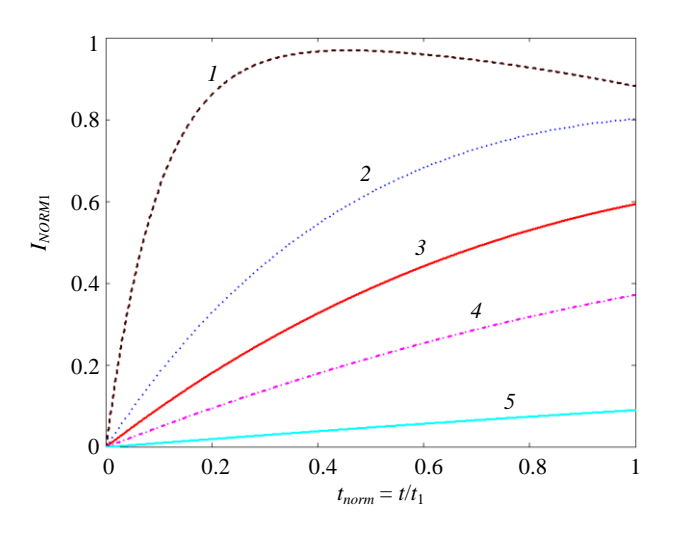


Fig. 6. The specified current pulse graph between the first and second grid at x0 = 0.15 m, $\alpha = 0$ °, Vz = 1000 m/s: $1 - t_1/\tau = 10$; $2 - t_1/\tau = 2$; $3 - t_1/\tau = 1$; $4 - t_1/\tau = 0.5$; $5 - t_1/\tau = 0.1$

Conclusion

We propose an analytical model to describe the induced current in a sensor with non-parallel measuring grids, designed to measure the velocity vector of micrometeoroids and space debris. A large input circuit time constant causes a decrease in the input current amplitude, which can lead to a decrease in the sensor's ability to fast microparticles. accurately measure On the other hand, the discharge of the input capacity causes a drop in current amplitude when measuring slow microparticles. It was noted that the angle at which the microparticle enters the first grid also influences the measured signal waveform. The obtained data can be used in selecting the geometrical dimensions of a high-speed microparticle sensor.

REFERENCES

- 1. Wang W., Xue W., Wu S., Mu Z., Yi J. and Tang A. J., Materials **15** (3871), (2022).
- 2. Batanov A. F. and Khakhanov Yu. A. Ideas K.E. Tsiolkovsky in theories of space exploration: Materials of the 58th Scientific Readings dedicated to the development of the scientific heritage and the development of ideas of K. E. Tsiolkovsky, Kaluga, September 19–21, 2023. Kaluga: IP Streltsov I. A., 2023, pp. 109–112 [in Russian].
- 3. Veniaminov S. S. and Chervonov A. M., Space debris is a threat to humanity, Moscow, IKI RAS, 2012 [in Russian].

- 4. Usovik I. V. and Morozov A. A., Bulletin of the Moscow Aviation Institute **30** (4), 202–209 (2023) [in Russian].
- 5. Telegin A. M., Voronov K. E. and Shestakov D. A., Engineering physics, No. 1, 49–57 (2024) [in Russian].
- 6. Auer S., Rev. Sci. Instrum. **46** (2), 127–135 (1975).
- 7. Thomas E., Auer S., Drake K., Horányi M., Munsat T. and Shu A., Planetary and Space Science **89**, 71–76 (2013).
- 8. Sukhachev K. I., Telegin A. M., Grigoriev D. P., Shestakov D. A. and Dorofeev A. S., Instruments and Experimental Techniques **66** (2), 228–233 (2023).
- 9. Telegin A. M., Usp. Prikl. Fiz. (Advances in Applied Physics) **11** (6), 540–552 (2023) [in Russian].
- 10. Gershtein G. M. Modeling of fields by the method of electrostatic induction: (Induced current). The science. Ch. ed. physics and mathematics lit., 1970.
- 11. Inovenkov A. N., Konstantinov O. V. and Pirogov V. I., ZhTF **63** (9), 1–5 (1993).
- 12. Poklonsky N. A., Vyrko S. A. and Kocherzhenko A. A., ZhTF **74** (11), 75–78 (2004).
- 13. Shockley W., Journal of Applied Physics **9** (10), 635–636 (1938).
- 14. Jones T. B. and Bliss G. W., Journal of Applied Physics **48** (4), 1412–1417 (1977).
- 15. Semkin N. D. and Telegin A. M., Measurement Techniques **59** (12), 1304–1309 (2017).

PLASMA PHYSICS AND PLASMA METHODS

UDC 533.9.082, 537.52 PACS: 52.70.Kz

EDN: ZTNBKN

Studying emission of the short high current vacuum arc with copper electrodes

Y. A. Barinov K. K. Zabello, A. A. Logachev, I. N. Poluyanova, S. M. Shkolnik

The work provides for the measurement of emitted power of the high current vacuum arc burning on copper electrodes. The emission measurement range was $100 \text{ nm} \le \lambda \le 1.100 \text{ nm}$. The developed measurement method allowed for analyzing the change of the emitted power depending on the arc current in visible and ultraviolet spectrum parts and in the vacuum ultraviolet region. Analysis of the obtained results demonstrated that the emitted power spectrum redistributes in the vacuum arc with a high anode activity. The obtained results allowed the possibility to evaluate the emission fraction in the arc power balance.

Keywords: vacuum arc; emitted power; low temperature plasma; electromagnetic emission; electric arc.

DOI: 10.51368/1996-0948-2025-1-11-15

Introduction

The high current vacuum arcs studies are foremost related to development of the vacuum arc-damping equipment. Therewith, the electromagnetic emission means a lot in the vacuum arc power balance. With the increasing arc current and relatively increasing plasma density, the emission role becomes more significant [1]. It is quite a

difficult task to determine the arc power balance considering the emission.

The electromagnetic emission is generally not considered under mathematical simulation of the vacuum arc. However, some approximate calculations were made considering the arc emission [2–4]. When studying the plasma emission experimentally, the spectroscopic methods are mainly used [5]. In our works [6–8] we measured the

Yuri A. Barinov¹, Senior Staff Scientist, Candidate of Physical and Mathematical Sciences

E-mail: yury@mail.ioffe.ru

Konstantin K. Zabello¹, Staff Scientist,

Candidate of Physical and Mathematical Sciences

E-mail: zabellok@mail.ioffe.ru

Aleksandr A. Logachev¹, Staff Scientist

E-mail: logatchev@mail.ioffe.ru

Irina N. Poluyanova², Department Head

E-mail: pin@tavrida.com

Sergey M. Shkolnik¹, Candidate of Physical and

Mathematical Sciences

E-mail: shkolnik@mail.ioffe.ru

¹ Ioffe Physical-Technical Institute

26, Polytekhnicheskaya st., St. Petersburg, 194021 Russia

² Switchgear Design Office

12, 1905 Revolution st., Sevastopol, 299003 Russia

Received September 12, 2024 Revised October 11, 2024 Accepted February 1, 2025 Scientific specialty code: 1.3.9

© Y. A. Barinov, K. K. Zabello, A. A. Logachev, I. N. Poluyanova, S. M. Shkolnik, 2025

emission flow created by the entire plasma volume. These works provide for the results of emission measurement of the high current vacuum arc with the copper chromium composition (CuCr30) electrodes used in the advanced arc-damping chambers. In the previous works, the authors studied $200 \text{ nm} \le \lambda \le 1100 \text{ nm}$ spectrum range. It emerged that a major part of emission was concentrated within $\lambda < 400$ nm range, and the emitted power fraction in the arc with the anode activity was nearly 25 % of the total arc power. These measurements along with the measurements of discharge current and arc voltage can be used to determine the basic plasma parameters [9].

Upon achievement of a certain current density, the developed high current arc demonstrates the anode activity, and there are quite large areas of a material fusion on both electrodes. Such fusion temperature reaches 2.000 K [10]. Therewith, the copper melting point is 1.356.55 K, and the chromium one is 2.130 K. At such temperatures, evaporation from the copper electrodes surface would be significant, which means the basic material in the interelectrode gap would be copper vapors. Within the vacuum ultraviolet range (100–200 nm), there are quite many intensive lines of copper atoms and ions. Thus, it can be suggested that the power emitted from the arc within this range would be significant. To assess contribution of each electrode component (Cu, Cr) to emission, we have measured emitted power of the vacuum arc burning on copper electrodes at this stage of the study.

Experimental procedure

The high current vacuum arc emission was measured within $100 \text{ nm} \le \lambda \le 1.100 \text{ nm}$ range, this range also includes the vacuum ultraviolet (VUV) region. The arc was ignited in the cathode center by an auxiliary discharge between an electrode and a needle with current withdrawn from it. The arc was

fed by the rectangular current pulse with the duration of 9 ms. The interelectrode gap was 4 mm. The current varied within 10-25 kA, which provides the average current density variation of $1.5 \text{ kA/cm}^2 \le j \le 3.5 \text{ kA/cm}^2$ in the completely developed arc. The end electrodes diameter was 30 mm. The electrodes material was oxygen-free copper (OFC Cu).

The experimental plant layout was previously described in [6]. Assessment of the high current vacuum arc emitted power based on the emission flow intensity registered with the photo receiver has been based on [11]. We will mention the basic plant parameters and critical auxiliary modifications here. The electrodes were located in the vacuum chamber under continuous exhaust ($\sim 10^{-4} \, \mathrm{Pa}$). To stabilize the discharge, a uniform axial magnetic field (AMF) was applied, the AMF induction was ~ 10 mT/kA. Thus, arching in diffusion mode was ensured. To register emission, three photodiodes FDUK8-UVS with the active area size of 3.5 mm were used. The typical sensitivity $S(\lambda)$ of the photodiode within 100 nm $\leq \lambda \leq 1.100$ nm range is shown in Figure 1.

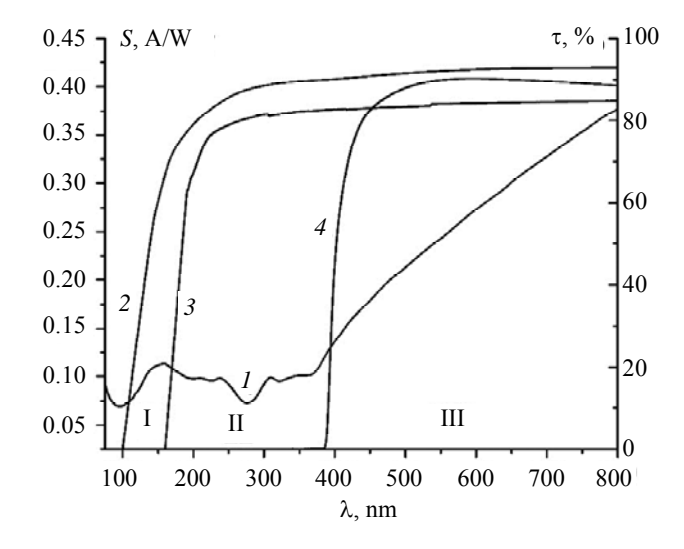


Fig. 1. Dependency of the photodiode sensitivity – 1 and filters transmission coefficients: $2 - MgF_2$; 3 - KU-1; 4 - ZhS-10

All three photodiodes were located inside the vacuum chamber, which allowed us for registering emission in the vacuum

ultraviolet. To divide the range registered by the photodiodes into regions (marked as I, II, III in Fig. 1), the light filters were used. transmits emission MgF_2 glass $\lambda \ge 100$ nm, KU1 quartz glass transmits light with $\lambda \ge 175$ nm, and Zh-10 color glass 9411-91) transmits (GOST $\lambda \ge 400 \text{ nm}$. Figure 1 shows the light filters transmission coefficients $\tau(\lambda)$ in addition photodiodes sensitivity. Within 100-400 nm range, the spectrum sensitivity characteristic of the photodiode changes insignificantly, so the emitted power in this region can be assessed quite easily within the narrow spectrum regions: 100–175 nm (Region I) 175–400 nm (Region II). The photodiode sensitivity characteristic in $\lambda > 400$ nm region (Region III) increases with the increasing wavelength, while the arc emission in the long wave region has a low sensitivity. Therefore, the authors calculated Region III sensitivity as an average within the range, which would not result in large error of the

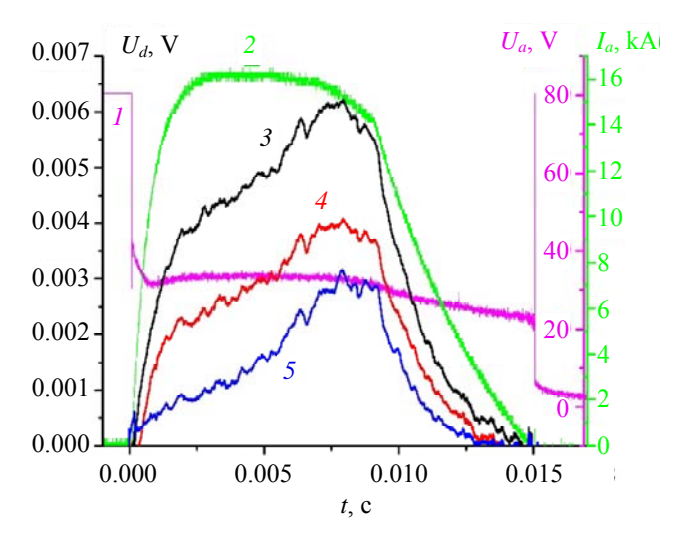


Fig. 2. Measurement results. $I_a \approx 16 \text{ kA}$. 1 - arc voltage; 2 - arc current; signals from photodiodes with filters: $3 - \text{MgF}_2$; 4 - KU1; 5 - ZhS-10

When the current reaches $I_a \approx 16 \text{ kA}$ (Fig. 2), and the first signs of anode activity occur on the electrodes, the signals from the diodes increase respectively. Regardless of the current pulse having a long-standing plateau, the signals from the diodes increase linearly, and become at least twice higher by

emitted power assessment. To limit the maximum signals registered by the photodiodes, the diaphragms of different diameters (from 1 mm for ZhS-10 filter to 0.5 mm for the others) were used.

Experiment results and discussion

the relatively small At current $I_a \approx 10 \text{ kA}$, when the arc burns in the diffusion mode without anode activity, the shape of the registered signals from the photodiodes approximately follows the discharge current shape. The registered signal is low, especially through ZhS-10 filter. Examples of the electrical measurement results under two large currents are shown in Figures 2 and 3. It can be observed that with the increasing current pulse amplitude, the photodiode pulse value and shape (and the emitted plasma power respectively) change significantly.

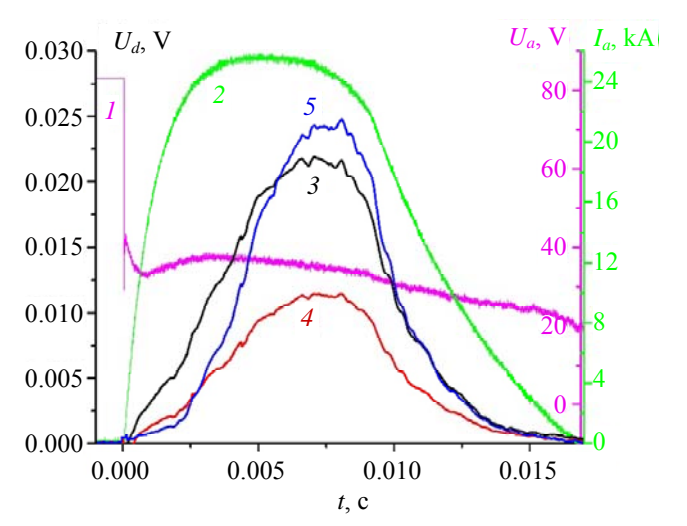


Fig. 3. Measurement results. $I_a \approx 25 \text{ kA}$. 1 - arc voltage; 2 - arc current; signals from photodiodes with filters: 3 - MgF2; 4 - KU1; 5 - ZhS-10

the pulse end, and for ZhS-10 filters, the triple increase is observed. Further current increase results in significant change of the diodes signals shape. At the pulse end, the signals emerge to increase rapidly, and at the currents of $I_a \approx 18 \text{ kA}$ (at such currents, significant fusion of surfaces is observed on

both electrodes), they increase at least fourfold by the pulse end. Therewith the signal received through MgF₂ filter starts increasing earlier than the others, but increase of the signal on the photodiode received through ZhS-10 filter is much higher than increase of the signals on other photodiodes.

Further current increase up to $I_a \approx 25 \text{ kA}$ (Fig. 3) does not result in change of the diode signals shape, but causes their significant increase. At the maximum current, both electrodes surfaces are melted completely.

Significant change of the shape of the signal from a photodiode at the currents significantly exceeding 15 kA correlates with occurrence of the anode activity. The anode activity results in increase of the plasma density and thereby in increase of the emission role significance.

By virtue of simultaneous emission registration with three photodiodes through different filters we can observe the dependency of emitted power P on discharge current within spectrum Region I (~ 100–175 nm), Region II (~ 175–400 nm) and Region III ($\lambda \ge 400$ nm) at different time after the arc ignition. These dependencies are shown in Figure 4.

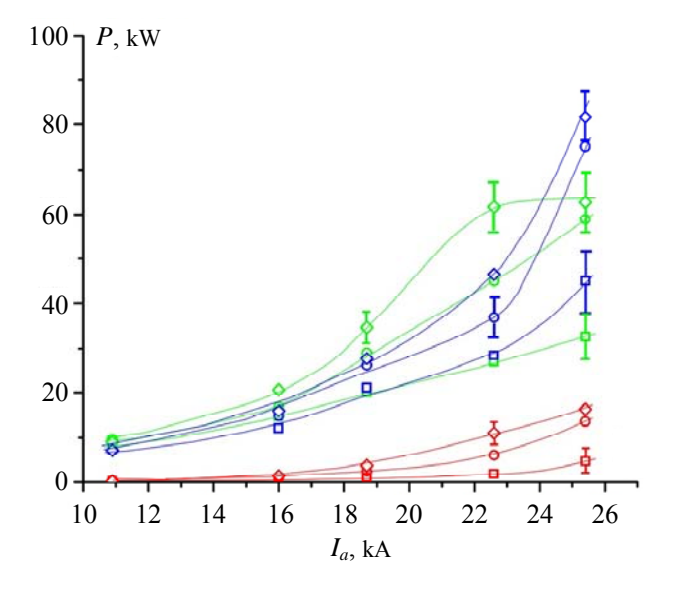


Fig. 4. Dependency of emitted power on current in different spectrum regions: blue - Region I; green - Region II; red - Region III. Time instants: square - 3.5 ms; round - 5.5 ms; diamond - 7.5 ms

Based on the shown dependencies, it can be observed that the emitted power in all observed spectrum regions reaches the maximum by the pulse end (7.5 ms). However, the change of the emitted power with the increasing current upon achievement of the limit currents, when activity on the anode is already high enough $(I_a > 20 \text{ kA})$, is not the same for different regions of the spectrum.

In Region III, the emitted power in the arc with the developed anode activity increases by an order of magnitude, as compared to the arc in the diffusion mode without anode activity. In addition, the emitted power increases significantly with the increasing current in the vacuum ultraviolet region (Region I). Therewith, at the limit currents, the increase speeds up and achievement of the maximum emission is observed faster.

There is a different story in the medium (Region II). spectrum region Before occurrence of the anode activity, the emitted power increases in step with the vacuum ultraviolet region, but at the current of ~ 22.5 kA, the power increases rapidly and reaches the value above the power in the vacuum ultraviolet region, although at the current pulse end (7.5 ms). While at a higher $(\sim 25 \text{ kA})$ the emitted current magnitude in Region II nearly does not increase, as compared to emission in Region I. Therewith emission to Region II reaches its saturation as early as in the middle of the current pulse.

Emission in Region I is generally determined by ionic, also resonance, copper lines. The significant part of emission in Region II would be determined by atomic lines so far (two resonance lines of the copper atom are located there as well). At the currents of $I_a > 20$ kA, the authors observe the both electrodes completely fused, which means that copper is evaporated from the surface intensively. With increasing current, the atoms evaporated from the surface would

be ionized actively, and emission would increase respectively.

Conclusion

Emission plays a substantial role in the developed vacuum arc. At 25 kA arc current, about 900 kW power would be emitted in the discharge. Based on our assessment, about 150 kW would escape from the arc at the emission within $\sim 100-1.100$ nm, that is up to 15 % of the total discharge power would be emitted by the end of arcing at the high current densities. Therefore, calculation of power balance in high current vacuum arcs should consider emission. Therewith the emitted power increases faster with the increasing current in the vacuum ultraviolet region. At the current of 25 kA (current density $j \le 3.5 \text{ kA/cm}^2$), emission in vacuum ultraviolet reaches 80 kW by the pulse end. In 175-400 nm spectrum region, the maximum is achieved at the lower current $(I_a = 22 \text{ kA})$ and amounts -60 kW. The analysis demonstrates that the emitted is redistributed to the vacuum ultraviolet in the developed vacuum arc with anode activity. It means measurements should be also taken in the shorter waves region ($\lambda \le 100 \text{ nm}$).

REFERENCES

- 1. Raizer Yu. P., Gas Discharge Physics, Berlin Heidelberg, Springer, 1991.
- 2. Schade E. and Shmelev D. L., IEEE Trans. Plas. Sci. **31** (5), 890–901 (2003).
- 3. Wang L., Jia S., Liu Y., Chen B., Yang D. and Shi Z., J. Appl. Phys. **107** (11), 113306 (2010).
- 4. Wenzel N., Kosse S., Lawall A., Renz R. and Hartmann W., Proc. 25th Int. Symp. Discharges Electr. Insul. Vac. (ISDEIV), 2012, pp. 321–324.
- 5. Ochkin V. N., Spectroscopy of Low Temperature Plasma, Weinheim, John Wiley & Sons, 2009.
- 6. Barinov Yu. A., Zabello K. K., Logachev A. A., Poluyanova I. N., Sherstnev E. V. and Shkol'nik S. M., Tech. Phys. Lett. **47** (2), 118–121 (2021).
- 7. Barinov Y. A., Zabello K. K., Logachev A. A., Poluyanova I. N., Sherstnev E. V., Bogdanov A. A. and Shkol`nik S. M., IEEE Trans. Plasma Sci. **50** (9), 2729–2735 (2022).
- 8. Barinov Yu. A., Zabello K. K., Logachev A. A., Poluyanova I. N. and Shkol'nik S. M., Proc. 30th Int. Symp. on Discharges and Electr. Insul. in Vac. (ISDEIV), 2023, pp. 235–237.
- 9. Lapshin V. F., Applied Physics, No. 3, 10–17 (2023) [in Russian].
- 10. Zabello K. K., Poluyanova I. N., Logachev A. A., Begal D. I. and Shkol'nik S. M., IEEE Trans. Plas. Sci. **47** (8), 3563–3571 (2019).
- 11. Lapshin V. F., Applied Physics, No. 5, 25–31 (2022) [in Russian].

PLASMA PHYSICS AND PLASMA METHODS:

UDC 537.525 PACS: 52.50.Dg EDN: CDTYKW

Ionic composition of the planar magnetron plasma in gas and vacuum operation mode

D. B. Zolotukhin, M. V. Shandrikov, G. Yu. Yushkov

The results of experimental study and numerical simulation of the fractional content of argon and copper ions in plasma generated in the direct current planar magnetron with the copper target in gas mode (at the argon pressure of 0.1 Pa) and vacuum mode (at the residual gas pressure of 0.04 Pa) are provided. It is demonstrated that the copper ions fractions in gas and vacuum modes at the discharge current sufficient to maintain the self-sputtering mode (10 A) are quite similar and amount to 97% and 100% respectively. The results of experiments and numerical evaluations evidence the possibility to perform stable operation of continuous discharge and obtain the metal ions flow in high vacuum of the planar magnetron without effects of thermal evaporation or sublimation of the copper target.

Keywords: planar magnetron; self-sputtering mode; vacuum operation mode.

DOI: 10.51368/1996-0948-2025-1-16-23

Introduction

Today magnetron sputtering is the most common method of physical deposition of protective and functional coatings.

Denis B. Zolotukhin, Senior Staff Scientist, Doctor of Physical and Mathematical Sciences E-mail: zolotukhinden@gmail.com

Maksim V. Shandrikov, Senior Staff Scientist, Candidate of Engineering Sciences

Georgy Yu. Yushkov, Chief Staff Scientist, Doctor of Engineering Sciences

High Current Electronics Institute of the Siberian Branch of the Russian Academy of Sciences 2/3, Akademicheskiy Ave., Tomsk, 634055 Russia

Received October 21, 2024 Revised December 10, 2024 Accepted February 1, 2025 Scientific specialty code: 1.3.5

© D. B. Zolotukhin, M. V. Shandrikov, G. Yu. Yushkov, 2025

Meanwhile the free length of sputtered atoms is compatible or even lower than the relevant distances from the sputtered magnetron target to the substratum under standard values of the operating pressure during magnetron sputtering (0.5–10 Pa) [1, 2].

Collisions with the operating gas particles in the space between the target and the substratum result in the sputtered atoms power dissipation and reduction, which affect the created coating quality and properties [3–5]. With the increasing pressure of the operating gas, the created coating becomes porous and has the prevailing column-type structure [6, 7].

Elimination of the above-mentioned deficiencies is possible in so-called self-sputtering mode, in which the discharge is maintained by virtue of ionization of the sputtered material of the target, but not the

one of the operating gas [8, 9]. Under sufficient discharge energy and therefore the amount of the sputtered metal atoms in the ionization area, such discharge is able to transfer to a continuous form and operate without the operating gas supply at the operating pressure determined by the vacuum exhaust system only [10–12].

Regardless of the fact that this type of discharge has been previously implemented in the experiment, today there is a lack of works related to simulation of the processes taking place in it, including the mass-to-charge plasma composition.

This work provides the results of experimental study and numerical simulation of the fractional content of argon and copper ions in plasma generated in the direct current planar magnetron with the copper target, under gas mode (at the argon pressure of 0.1 Pa) and vacuum mode (at the residual gas pressure of 0.004 Pa).

Experimental procedure and method

The planar magnetron with the directly cooled copper target 100 mm in diameter was used in the experiments. The initial target thickness was 4 mm. The intensive watercooling system (20 l/min as a minimum) ensured the possibility of the magnetron discharge operation in continuous mode, with the power output up to 8 kW. The magnetic field of 100 mT on the target surface in the intensive sputtering area was ensured by NdFeB magnets of N35 grade placed in the water jacket at the maximum operating temperature of + 80 °C. The circular electrode (for creation of the round cross section of the particles flow) with the diameter of 100 mm that had the potential of the grounded vacuum chamber walls and was located 8 cm away from the cathode target edge, was used as the magnetron anode. The discharge voltage in the vacuum mode was 590–610 V at 8–12 A magnetron discharge current. The voltage was approximately 50–60 V lower in the gas mode, with the same discharge current (probably due to more efficient sputtering of the copper target with argon ions as compared to copper ions [8]).

By virtue of a large internal volume of the vacuum chamber (about 65 liters) and water cooling of the target, the temperature of the external target surface (from the discharge did not exceed 200 °C side) experiment with the magnetron operating at 8 kW. The surface of the heated target can have the higher gas temperature but the lower concentration, though it is true generally for all types of particles (neutrals and ions of both argon and copper), and therefore it hardly affects the trends of the curves. Thus, it was considered that the target was not the source of the operating gas heating, and the temperature thereof was assumed as the room temperature in the assessment. Pressure in the chamber was maintained constant, with the equal processes of argon supply close to the target and exhaust thereof with the pump through an aperture located in the outermost area of the vacuum chamber.

To study the mass-to-charge composition of the plasma ions, the modified quadrupole mass-spectrometer RGA-200 (Stanford Research Systems) was used, the input aperture of which was located 25 cm magnetron the target. spectrometer collector was located under the "ground" potential, like the grounded walls of The the vacuum chamber. magnetron discharge plasma was diffused into the cylindrical expander, the end of which was cut-off with the fine-structure non-magnetic stainless-steel mesh. The potential gradient for ions acceleration into the spectrometer

was ensured by an individual power source between the magnetron anode and grounded walls of the vacuum chamber. The optimum value of the bias potential was 30–50 V. The detailed description of the discharge cell of the planar magnetron and the equipment for measurement of the mass-tocharge composition of ions used in the experiment can be found in Experimental peaks of the ionic mass spectrum were integrated for more specific determination of the fractional ratio of ionic components in plasma.

Numerical model

The discharge processes in the described previously magnetron were simulated based on the following provisions. It was assumed that the flat cathode target of the magnetron had the disk shape with the diameter D, the discharge plasma occupied the internal volume between the target and the annular anode with the height h. Opposite to the model described in [13], the abovementioned model did not account for the electron beam injection into the discharge area, there was no additional reflecting electrode, and the discharge was initiated and maintained with the voltage U_d between cathode and anode. The operating gas in the model was argon at p_{Ar} pressure and permanent $T_{Ar} = 300 \text{ K}$ temperature; weight of the atom thereof, ionization potential and ionization cross section within the energy range of 0 to 3.000 eV (that reaches the maximum of $\sim 4 \times 10^{-16} \text{ cm}^2$ at $\sim 31 \text{ eV}$) [14, 15] were considered. Under the ion impact of the copper target surface, its sputtering took place which was determined by sputtering coefficient γ_{sp} depending on the ion energy [8, 16], and copper atoms entered

the argon plasma, which were further ionized in it with the energized electrons, taking into account the potential and ionization cross section for copper [14], without consideration (for simplification) of any target alloying by the incoming ions of any type. The sputtering coefficient was approximated with the following formula:

$$\gamma_{sp}\left(\varepsilon_{iAr}\right) = \frac{0.06}{\varepsilon_{t}} \sqrt{Z_{x}} \left(\sqrt{\varepsilon_{iAr}} - \sqrt{\varepsilon_{th}}\right)$$

where 0.06 is the constant with the dimension of $(eV)^{-1/2}$ [17], ε_{iAr} is the energy of argon ions accelerated in the cathode potential fall, ε_t is the target material bond energy, the threshold and ε_{th} is ion energy from which sputtering is started, $Z_x = 2Z_{\text{Cu}} / ((Z_{\text{Ar}}/Z_{\text{Cu}})^{2/3} + (Z_{\text{Cu}}/Z_{\text{Ar}})^{2/3})$ mentioned atomic number determined by atomic numbers of the operating gas Z_{Ar} (argon) and the target Z_{Cu} (copper).

The fraction of copper $n_{i\text{Cu}}$ and argon $n_{i\text{Ar}}$ ions in the plasma was determined based on the ratio of concentrations thereof to the total concentration of ions in the plasma $n_i = n_{i\text{Ar}} + n_{i\text{Cu}}$. The above-mentioned values were determined as a result of the following equations solution:

$$n_{i,Ar} = I_d \left(n_{Ar} \sigma_{i,Ar} \left(U_d \right) \times \left(U_d / W_{i,Ar} \right) h \right) / \int 0.4 \left(1 + \gamma_{ie} \right) e \sqrt{2kT_e / M_{Ar}} S_c \right], \tag{1}$$

$$n_{i\text{Cu}} = I_d \left[n_{\text{Cu}} \left(\gamma_{sp} \right) \sigma_{i\text{Cu}} \left(U_d \right) \times \left(U_d / W_{i\text{Cu}} \right) h \right] / \left[0.4 \left(1 + \gamma_{ie} \right) e \sqrt{2kT_e / M_{\text{Cu}}} S_c \right]$$
(2)

where I_d is discharge current; $n_{Ar} = p_{Ar}/kT_{Ar}$ is the concentration of neutral argon atoms; $n_{Cu}(\gamma_{sp})$ is the concentration of neutral copper atoms knocked out from the copper atoms target depending on γ_{sp} under established U_d

and I_d ; $\sigma_{iAr}(U_d)$, $\sigma_{iCu}(U_d)$ is the cross section of argon and copper atoms ionization with $W_{iAr} \approx 2\varphi_{iAr} \approx 30 \text{ eV},$ discharge electrons; $W_{i\text{Cu}} \approx 2\varphi_{i\text{Cu}} \approx 15 \text{ eV}$ is the potential of ionelectron pair formation for argon and copper $(\varphi_{iAr}, \varphi_{iCu})$ are their ionization potentials) [18]; ion-electron emission is the coefficient (for the energies below 1 keV) [19]), M_{Ar} , M_{Cu} is the mass of argon and copper atom, $S_c = \pi D^2/4$ is the cathode target area. To simplify the calculations, it was assumed that the electrons temperature in the plasma T_e has adopted the typical value of 5 eV. The rest of the model equations are provided in details in [20]. The multipliers $(U_d/W_{iAr})h$ of (1) and (2) expressions have the meaning of the number of ionization processes per the discharge span length, consideration of the without electron multiplication avalanche in the plasma volume (due to rarity of such events and the need of more sensitive additional experiments confirm significance of the mentioned process under the reviewed experimental conditions).

Equations (1) and (2) have been recorded under approximation of the absence of electron multiplication in the layer, as it is well known that there is no electron multiplication in the cathode layer of the low-pressure magnetron discharge (especially in its high current form because the layer is collision-free) [21–23].

The concentration of copper and argon ions was calculated based on the balance that ions generation in the discharge determined by the numerators of expressions (1) and (2) has been compensated by Bohm flow of ions away from the plasma, which is described by the denominator of these expressions. Applicability of the Bohm equation, that describes that the density of the ionic flow from the plasma border is proportional to the

ions concentration and does not depend on their temperature and the applied voltage, is justified by the fact that the directed velocity of the magnetron discharge plasma ions is less than the Bohm velocity (that depends on electrons temperature in the plasma).

The degree of the plasma ionization was calculated based on two approximations: (1) given all plasma components – both neutrals and ions of copper and argon (α_{tot}) , and (2) taking into account the metal (copper) ions and neutrals (α_m) only, according to the following expressions:

$$\alpha_{tot} = 100 \% \times [(n_{iAr} + n_{iCu})/(n_{Ar} + n_{Cu})],$$
 (3)

$$\alpha_m = 100 \% \times \left[\left(n_{iCu} \right) / \left(n_{Cu} \right) \right] \tag{4}$$

The degree of ionization determined based on equation (3) considers all plasma components (residual atmosphere, operating gas and sputtered target atoms), and therefore allows for characterizing the plasma to the fullest extent possible, while the direct experimental determination thereof can be complicated by the presence of multiple components in the plasma which are able to condensate on the measuring equipment elements and effect on the measurements accuracy.

Ionization degree (4) that considers the metal component of the plasma only can be generally measured directly with the use of electric [24] or magnetic [25] condensation probes and therefore comparison of the two methods of ionization degree assessments is of the large significance for the analysis of experimental measurements correctness.

The calculations results and comparison thereof with the experiment and the analysis are provided below.

Results and their discussion

Comparison of experimental and calculated fractions of argon and copper ions in the plasma is shown in Fig. 1*a*.

The calculated curves of ion fractions demonstrate satisfactory consistence with the experiment, which may be an indirect evidence of correctly calculated absolute values of the plasma ionic components concentrations and ionization thereof. According to the numerical simulation results, increase of the copper ions fraction (up to 97% in gas mode and up to 100% in vacuum mode) with the increasing discharge current is related to intensification of sputtering which is justified both by increase of the number of ions in the flow, and by the increase of the sputtering coefficient γ_{sp} of the copper target with the ions accelerated by the cathode voltage drop U_d .

Figure 1*b* shows the calculated values of ionization degree α_{tot} , α_m of the plasma in gas and vacuum modes. It shows that the ionization degree increases in line with the discharge current (from ~ 2 % at 3 A current in gas mode, up to ~ 15 % at 12 A current in vacuum mode), which is consistent with the experiment [26]. Some difference of about

1 % is observed between α_{tot} and α_m in gas mode only, when the argon ions and neutrals fraction are notable. In vacuum mode, when the fraction of these particles becomes negligible, the values of ionization degree α_{tot} , α_m are nearly the same, and can be equally used to assess the plasma ionization degree.

Figure 2 shows the calculated concentrations of argon and copper neutrals and ions in gas and vacuum modes.

From among calculated all concentrations in both modes and at the maximum values of the magnetron current, the maximum value is reached by the copper ions concentration due to intensive copper sputtering. The minimum value under the same conditions is taken by the argon ions concentration due to its lower ionization cross section and ionization potential exceeding the copper one. The relatively rapid increase both ion types concentration with the increasing discharge current is notable mode and at small currents (up to 3–4 A). With further increase of the discharge current, dependency of both ionic and neutral components of the plasma transfers to saturation in both gas and vacuum modes.

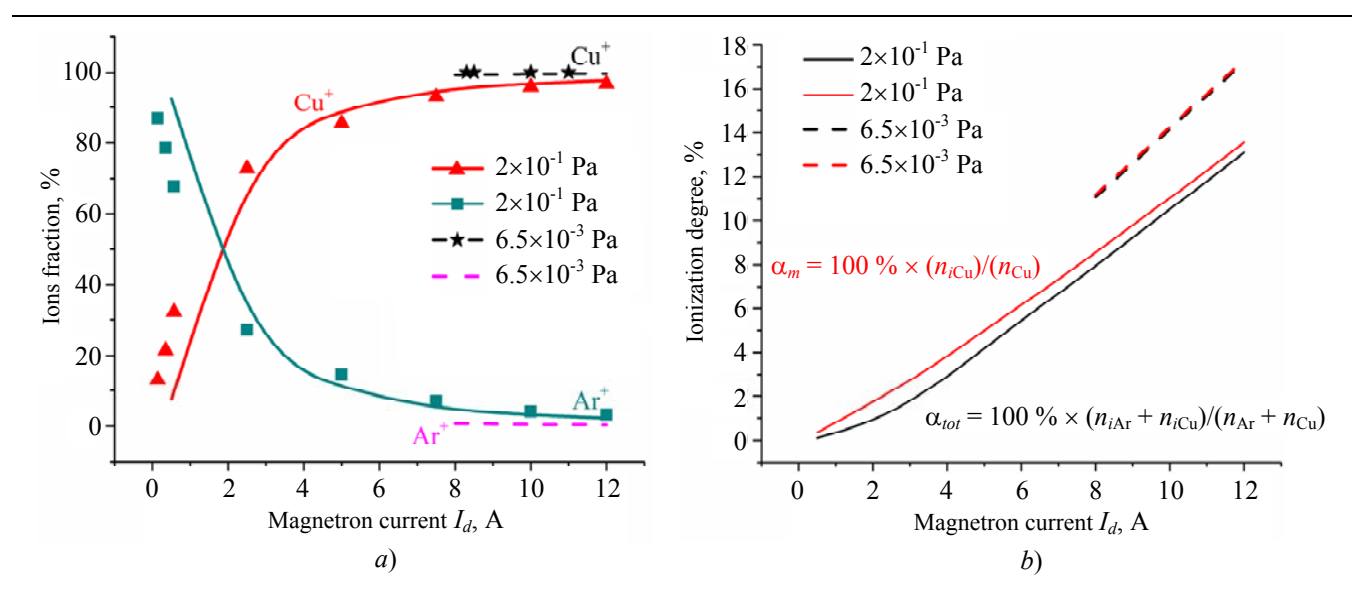


Fig. 1. a) – Calculated and experimental fractions of copper and argon ions in plasma versus the magnetron current, and b) – calculated ionization degrees α_{tot} and α_m of the plasma in gas (at argon pressure of 0.2 Pa) and vacuum (at argon pressure of 0.0065 Pa) modes

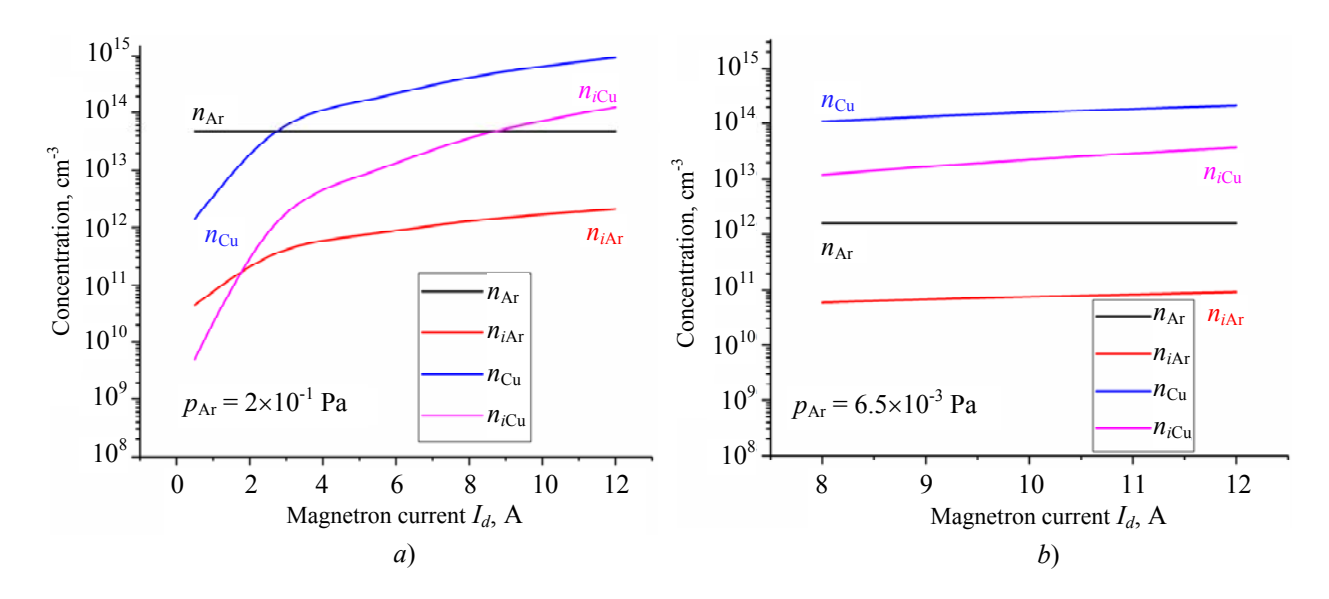


Fig. 2. Calculated concentrations of neutral and ionic components of argon and copper in gas (a) and vacuum (b) modes

Given the cathode layer is collision-free in the low-pressure (up to 0.004 Pa in this case) discharge, and its width in the intensive sputtering area on the target surface does not exceed 1 mm at the discharge current of 10 A, and that the ionic compositions of the plasma at such current value in gas and vacuum modes is nearly the same (97 and 100 %, respectively), it can be suggested that the differences of the potential distribution (due

to different burning voltage in gas and vacuum modes) would not significantly affect the concentration growth mechanism.

Conclusion

The results of experimental study and numerical simulation of ionization processes in plasma generated in the direct current planar magnetron with the copper target in gas and vacuum modes allow for explaining the mass-to-charge composition of the plasma ions in different operation modes of the discharge. The obtained magnetron assessments of the sputtered target material degree have insignificant ionization difference for gas and vacuum modes, which is explained by the prevailing metal ion component in plasma at relatively high values of the discharge current independently of its operation mode.

The numerical simulation allows for calculation of the numerical values of neutrals and ions concentrations of operating gas, target material and the degree of ionization of the discharged gas metal plasma. As it comes from the simulation results, the process of ionic spurring is sufficient to operate the magnetron discharge in the vacuum self-spurring mode without involving any auxiliary effects of thermal evaporation and sublimation of the magnetron target.

One of the main conclusions obtained in this work is that the proposed model allows for assessing the degree of the sputtered material ionization consistently with the experiment (the parameter which is one of the key parameters in sputtering the coatings, as it justifies the level of ionic effect on the electrical bias surface). The obtained results are of scientific and practical interest in terms of comparison of the vacuum mode with any other modes magnetron sputtering of (DC, HIPIMS).

The studies have been supported by the Russian Science Foundation (Project No. 24-19-00031).

REFERENCES

1. Mitin D. M. and Serdobintsev A. A., Technical Physics Letters **43** (17), 78–85 (2017). http://dx.doi.org/10.21883/PJTF.2017.17.44950.16804 [in Russian].

- 2. Cuomo J., Kaufman H. R. and Rossnagel S. M. Hollow cathode enhanced magnetron sputter device, US Patent 4,588,490. 1985.
- 3. Helmer J. C. and Wickersham C. E., Journal of Vacuum Science & Technology A **4** (3), 408–412 (1986). https://doi.org/10.1116/1.573892.
- 4. Wu S., Chen H., Du X. and Liu Z., Spectroscopy Letters **49** (8), 514–519 (2016). https://doi.org/10.1080/00387010.2016.1212244.
- 5. Thomas III J. H., Journal of Vacuum Science & Technology A **21** (3), 572–576 (2003). https://doi.org/10.1116/1.1564027.
- 6. Thornton J. A., Journal of Vacuum Science & Technology **11** (4), 666–670 (1974). https://doi.org/10.1116/1.1312732.
- 7. Thornton J. A. and Penfold A. S. Thin Film Processes. New York, Academic, 1977.
- 8. Anders A., Andersson J. and Ehiasarian A., Journal of Applied Physics **102** (11), 113303 (2007). https://doi.org/10.1063/1.2817812.
- 9. Huo C., Lundin D., Raadu M. A., Anders A., Gudmundsson J. T. and Brenning N., Plasma Sources Science and Technology **23** (2), 025017 (2014). https://doi.org/10.1088/0963-0252/23/2/025017.
- 10. Kukla R., Krug T., Ludwig R. and Wilmes K., Vacuum **41** (7–9), 1968–1970 (1990). https://doi.org/10.1016/0042-207X(90)94147-I.
- 11. Posadowski W., Surface and Coatings Technology **49** (1–3), 290–292 (1991). https://doi.org/10.1016/0257-8972(91)90071-4.
- 12. Shandrikov M. V., Oks E. M., Oskirko V. O. and Cherkasov A. A., Technical Physics Letters **49** (22), 19–22 (2023). https://doi.org/10.61011/PJTF.2023.22.56594.19716 [in Russian].
- 13. Zolotukhin D. B., Plasma Physics Reports **49** (2), 296–299 (2023).

https://doi.org/10.1134/S1063780X2260195X.

- 14. Bartlett P. L. and Stelbovics A. T., Physical Review A **66**, 012707 (2002). https://doi.org/10.1103/PhysRevA.66.012707.
- 15. Golyatina R. I. and Maiorov S. A., Atoms **9**, 90 (2021). https://doi.org/10.3390/atoms9040090
- 16. Lieberman A. and Lichtenberg A. J. Principles of Plasma Discharges and Materials Processing, New York, Wiley, 2005.
- 17. Zalm P. C., J. Vac. Sci. Technol. B 2(2) **2** (2), 151–152 (1984).

https://doi.org/10.1116/1.582936.

- 18. Bates D. R. Atomic and Molecular Processes. New York, Academic, 1962.
- 19. Kaminsky M. Atomic and ionic collisions on a metal surface. Moscow, Mir, 1967 [in Russian].
- 20. Zolotukhin D. B., Journal of Physics: Conference Series **2291**, 012024 (2022). https://doi.org/10.1088/1742-6596/2291/1/012024.

- 21. Buyle G., Depla D., Eufinger K., Haemers J., De Bosscher W. and De Gryse R., Vacuum **74** (3–4), 353–358 (2004).
- 22. Gudmundsson J. T., Plasma Sources Science and Technology **29** (11), 113001 (2020).
- 23. Costin C. and Minea T. M., Scientific Reports **13** (1), 15883 (2023).
- 24. Gavrilov N. V., Emlin D. R. and Kamenetskikh A. S., Vacuum **233**, 114040 (2025). https://doi.org/10.1016/j.vacuum.2025.114040
- 25. Tyunkov A. V., Andronov A. A., Oks E. M., Yushkov Yu. G. and Zolotukhin D. B., Vacuum **208**, 111722 (1–4) (2023). https://doi.org/10.1016/j.vacuum.2022.111722.
- 26. Semenov V. A., Oks E. M., Solovyev A. A. and Shandrikov M. V., Vacuum **230**, 113649 (2024). https://doi.org/10.1016/j.vacuum.2024.113649.

PLASMA PHYSICS AND PLASMA METHODS

UDC 533.9.08 PACS: 52.70.-m

EDN: ESIXGW

The influence of the working gas composition on the mass-to-charge composition of ions in the beam plasma during the evaporation of an YSZ target by an electron beam

A. V. Tyunkov, A. A. Andronov, D. B. Zolotukhin, T. O. Klimkin, A. K. Nesterenko, S. A. Salnikov, Yu. G. Yushkov

The paper presents the results of a study on the mass-to-charge composition of ions in the beam plasma generated during the evaporation of a solid-state ceramic target made of yttria-partially stabilized zirconia (YSZ) in an environment of inert and reactive gases by an electron beam in the forevacuum pressure range. Monitoring of the mass-to-charge composition of beam plasma ions was carried out using a modernized RGA-300 residual atmosphere mass analyzer. The influence of the working gas composition on the mass spectra of ions of the evaporated target material is shown.

Keywords: type of working gas; mass-to-charge composition; beam plasma; YSZ.

DOI: 10.51368/1996-0948-2025-1-24-30

Introduction

A distinctive feature of forevacuum plasma electron sources is that they generate beam plasma with a concentration of up to 10^{11} cm⁻³ during beam transport through the volume of a vacuum chamber [1]. The electron beam formed at forevacuum pressures is an effective tool to modify the

surface of non-conductive materials [2, 3], and the generated plasma is used, for example, to initiate plasma-chemical reactions [4].

In addition to assisting and initiating any processes in the plasma, the generated ions are used directly for surface modification [5]. When a negative potential is applied to the substrate, the beam plasma ions accelerate

Andrey V. Tyunkov, Senior Staff Scientist, Candidate of Technical Sciences Artem A. Andronov, Junior Staff Scientist

Artem A. Andronov, Junior Staff Scientist E-mail: artem.andronov.98@bk.ru

Denis B. Zolotukhin, Leading Staff Scientist, Doctor of Physical and Mathematical Sciences

Timur O. Klimkin, Junior Staff Scientist

Alexey K. Nesterenko, Junior Staff Scientist

Sergey A. Salnikov, Junior Staff Scientist

Yury G. Yushkov, Head of the Laboratory, Doctor of Technical Sciences

Tomsk State University of Control Systems and Radioelectronics

40, Lenina Ave., Tomsk, 634050 Russia Received September 17, 2024

Revised October 16, 2024 Accepted December 8, 2024 Scientific specialty code: 1.3.5

© A. V. Tyunkov, A. A. Andronov, D. B. Zolotukhin, T. O. Klimkin, A. K. Nesterenko, S. A. Salnikov, Yu. G. Yushkov, 2025

and bombard it. By changing the magnitude of the negative potential, it allows to control the magnitude of the ion energy, consequently, manage the processes activation, cleaning or sputtering of the treated surface. Accordingly, knowledge of the ion composition of the beam plasma is important when forming coatings performing other types of surface modification of products.

Today, mass spectrometric studies of beam plasma in the forevacuum range are complicated, since the ion path lengths do not exceed units of centimeters. To solve this problem, the authors [6] modernized the RGA-100 quadrupole residual atmosphere analyzer and also conducted research on the analysis of the ion composition of beam plasma of various gases.

The study of the influence of the type of working gas on the mass-to-charge composition of ions in the process of evaporation of a target partially stabilized with yttrium oxide zirconium dioxide (YSZ) a kev role in improving characteristics of the resulting coating. The choice of working gas directly affects the temperature of the beam plasma electrons, generation, transportation, and focusing of the electron beam, as well as other parameters of the beam and plasma [7], which, in turn, determines the efficiency of evaporation and the uniformity of the distribution of the material over the surface of the product. Different gases can result in the formation of ceramics with different physical and performance properties.

Thus, the study of the influence of the type of working gas on the parameters of beam plasma in the context of electron beam evaporation with subsequent ionization of YSZ ceramic vapors is an important step towards the creation of high-quality materials with the necessary properties and the improvement of their production technologies. This paper presents the results of a study of the mass-to-charge composition of ions generated as a result of evaporation of a solid YSZ target in an atmosphere of various gases.

Experimental technique and methodology

The scheme of experiments for studying the mass-charge composition during the evaporation of a solid target is presented in Figure 1. A fragment of zirconium ceramics partially stabilized with yttrium oxide YSZ (target) was placed on a crucible made of carbon. The electron beam was formed by a forevacuum source with a plasma cathode, after which it passed through an atmosphere of working gas (helium, a mixture of helium with argon, a mixture of helium with oxygen) to the target. During transportation, the beam electrons ionized the working and residual gases. Using a focusing and deflection system, a low-power electron beam (U_{acc} = 3 kV, I_{em} = 23 mA) was positioned on a ceramic target and preheated it to prevent explosive cracking. The electrode system and the operating principle of the electron source are described in detail in [8].

At the same time, monitoring of the gas atmosphere was carried out using a modernized RGA-300 residual atmosphere analyzer (spectrometer) [9] according to the method [6]. The appearance of the upgraded analyzer is shown in Figure 2.

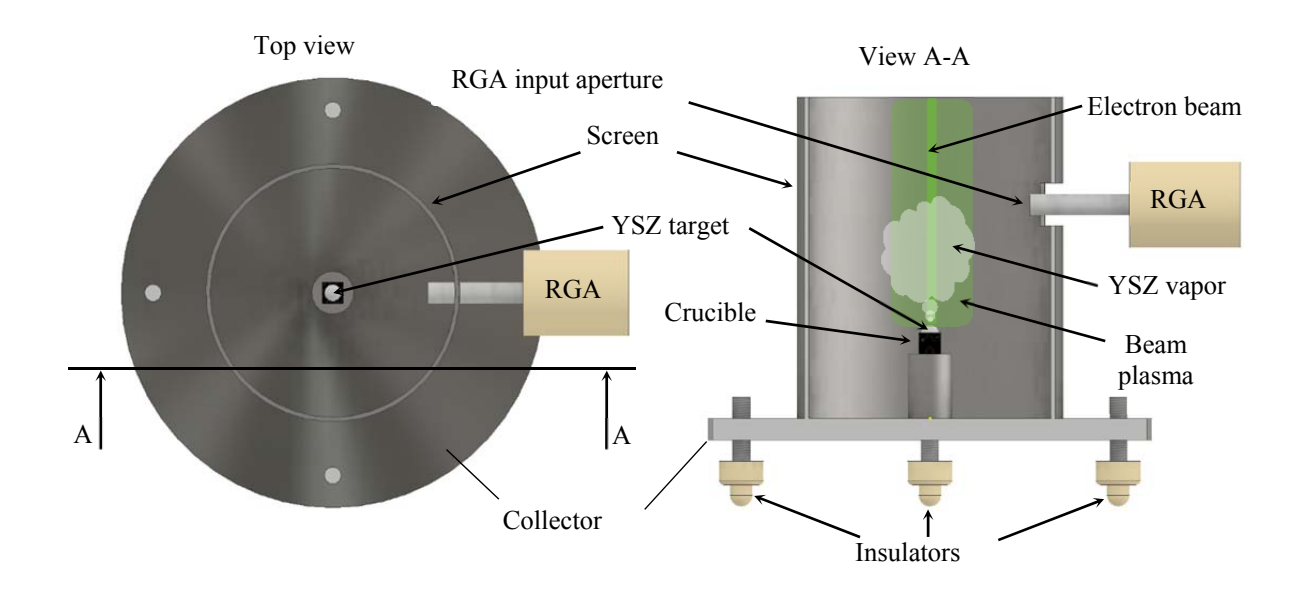


Fig. 1. Experimental scheme

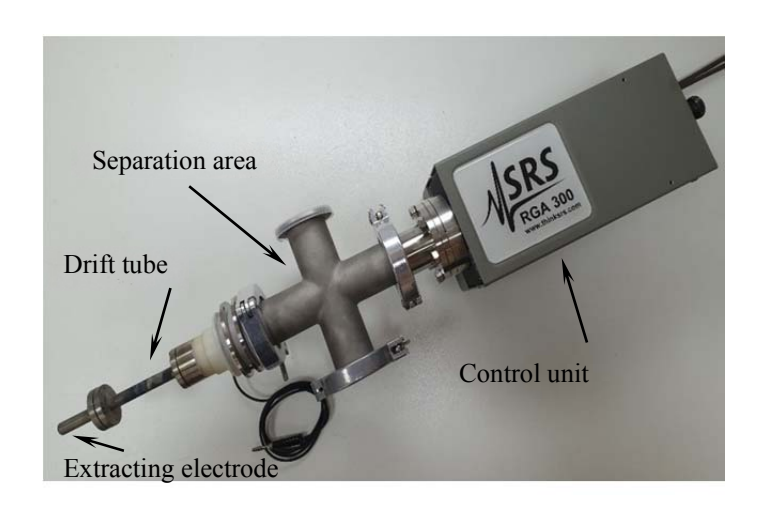


Fig. 2. Upgraded quadruple mass analyzer RGA-300

To control the ion flow into the ion separation area, the crucible and target were placed on the electron beam collector. The collector is made in the form of a massive stainless-steel disk, 10 mm thick and The 200 mm in diameter. disk was electrically connected to a thin-walled cylinder with a diameter of 130 mm. A technological hole was made in the cylinder to introduce the input aperture of the spectrometer. The collector was electrically isolated from the grounded walls of the vacuum chamber and other electrical parts of the unit, and was supplied with a positive potential of 50 V relative to ground. The target to be evaporated was located 4 cm from the input aperture of the mass analyzer, both in the vertical and horizontal directions.

After monitoring the gas atmosphere, the target was gradually heated to a temperature sufficient for its evaporation. At the same time, the mass-to-charge composition of plasma ions was monitored throughout the entire duration. The maximum parameters of the electron beam were as follows: accelerating voltage $U_{acc} = 13 \text{ kV}$,

emission current $I_{em} = 70$ mA. The residual pressure in the vacuum chamber was 1 Pa and was provided by a two-stage vacuum unit based on a vane-rotor pump and a Roots pump. The working pressure was maintained at 5.7 Pa. Helium was supplied through the hollow cathode of the electron source to a chamber pressure of 3.92 Pa. Then, additional gas (helium, argon, oxygen) was supplied directly into the chamber to the required value (5.7 Pa).

Results of experiments and discussion

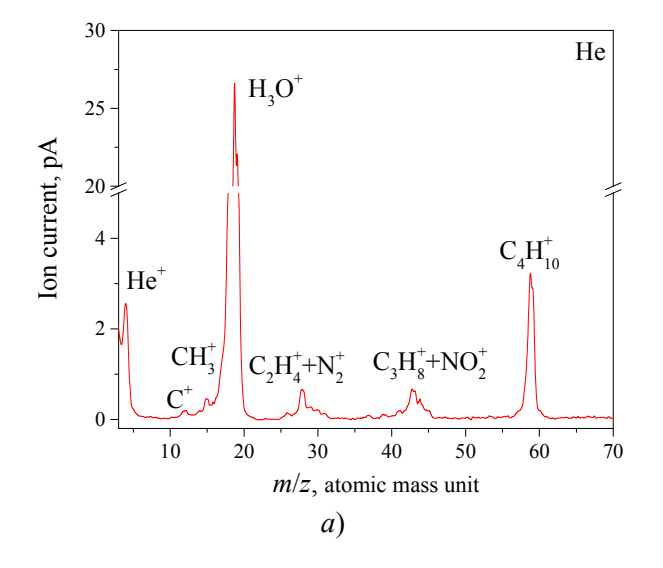
Figure 3 shows the ion spectra when using helium plasma gas before evaporation of the YSZ target material (a) and during intense evaporation (b).

During the heating of the ceramic target up to the evaporation temperature, the spectra (Fig. 3a) record ions of the residual atmosphere, mainly ions of water vapor and

hydrocarbons, as well as ions of the working gas (helium).

By increasing the power density of the electron beam to the level required for intensive evaporation of the target, ions of all stable isotopes of the target material (Fig. 3b), their oxides and dioxides can be detected in the spectra. It should be noted that the amplitude of the water vapor peak decreases as the target evaporation rate increases, while the amplitude of the target material ion peaks increases. The dominant ions of the target material at the initial stage of evaporation, when a melt pool only appears in the beam impact zone, are their dioxides. However, with a further increase in the beam power density, up to maximum values, the peaks of the target material oxides dominate, while the amplitude of the dioxide peaks decreases.

Figure 4 shows the ion spectra when using helium-argon mixture plasma gas before evaporation of the target material (a) and during intense evaporation (b).



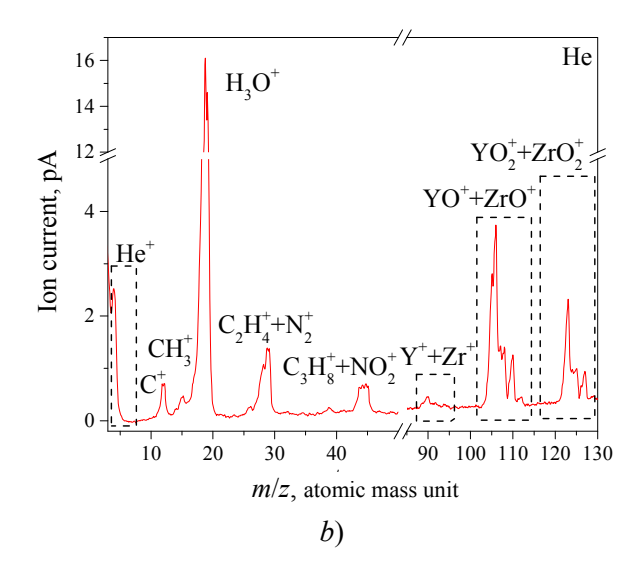
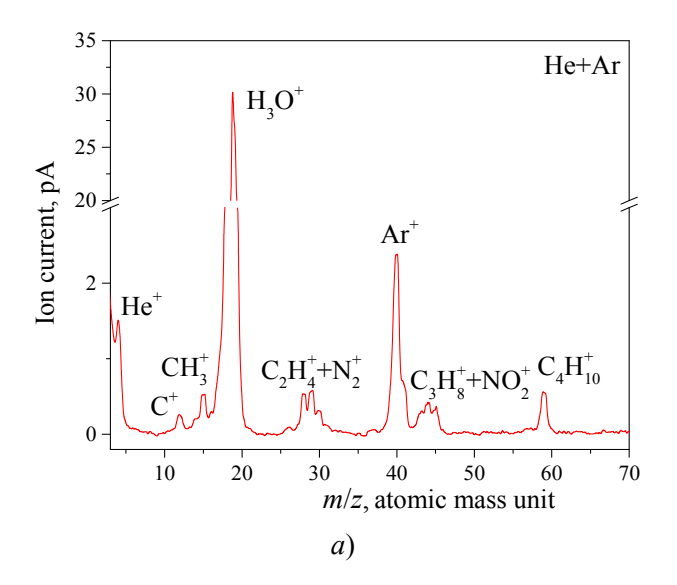


Fig. 3. Beam plasma ion spectrum before YSZ target evaporation (a) and during YSZ target evaporation (b): working gas – helium

Similar to the spectra where only helium was used as the working gas, the amplitude of the argon ion peaks does not exceed the amplitude of the water vapor peak. A possible

reason for the dominance of water vapor ion peaks is the excess of their number in the neutral state over the number of argon atoms. The adsorption of a large number of water molecules on the walls of the vacuum chamber is facilitated by the low pumping speed of the forevacuum pump and the absence of preliminary heating of the chamber. Since argon is inert and has a significant atomic mass, when it collides with the walls of the vacuum chamber, it desorbs water molecules, which are subsequently ionized by the electron beam. Thus, partial

replacement of helium with argon does not lead to significant changes in the ion spectra, except for the appearance of additional argon ions in the spectra. At the same time, an increase in the power of the electron beam and, consequently, the intensity of evaporation of the ceramic target ensures a further increase in the peaks of the target material oxides in the spectra.



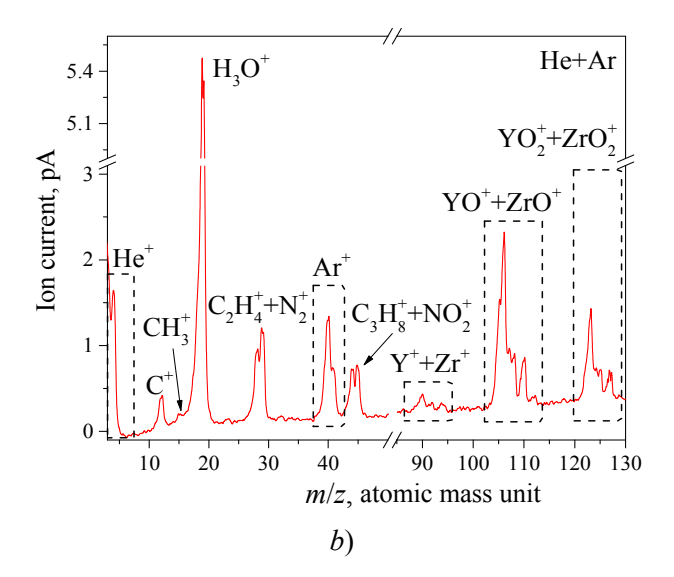


Fig. 4. Beam plasma ion spectrum before YSZ target evaporation (a) and during YSZ target evaporation (b): working gas – mixture of helium and argon

Figure 5 shows the ion spectra when using a mixture of helium and oxygen plasma-forming gas before evaporation of the target material and during intense evaporation. As it shown on Figure 5, the addition of oxygen significantly transforms the ion spectrum. At low electron beam power, the spectrum is dominated by the peak of molecular oxygen ions, which is explained by the large number of neutral oxygen molecules in the vacuum chamber and the close potentials and ionization cross-sections of oxygen and water molecules. Atomic oxygen ions are also recorded, indicating partial dissociation of oxygen molecules and ionization of decay products. However, when the target material evaporates intensively, the

of amount oxygen ions decreases significantly, and the peak of water vapor ions becomes dominant. The peaks of target material isotopes (pure Y, Zr) were not detected in the spectra. Only their oxides and dioxides have been recorded. In this case, the peaks of the isotopes of the target material dioxides are predominant, in contrast to the spectra when inert gases are introduced. Increasing the power of the electron beam does not lead to the dominance of oxide ions in the spectra, as when using inert gases. A decrease in the peak of molecular oxygen ions indicates the interaction of target material ions with oxygen ions, which ensures the predominance of dioxide ions at any electron beam power.

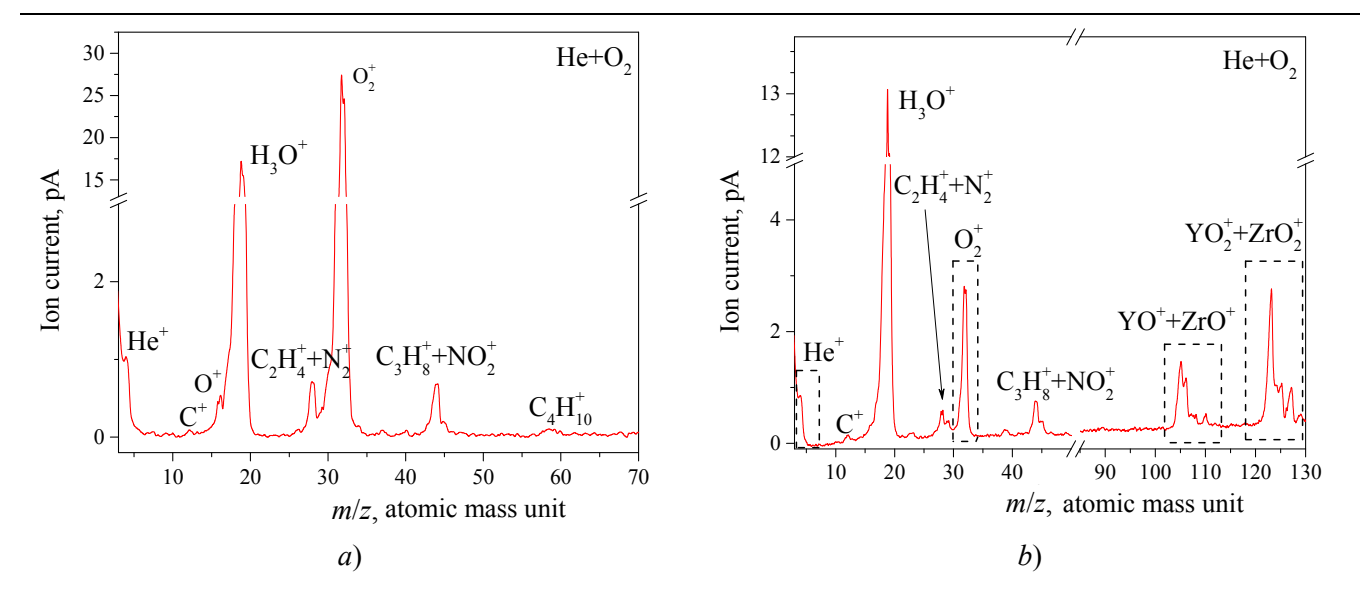


Fig. 5. Beam plasma ion spectrum before YSZ target evaporation (a) and during YSZ target evaporation (b): working gas – mixture of helium and oxygen

A qualitative explanation for these experimental facts may be as follows. When adding inert gases to a vacuum chamber, the dominance of dissociation or oxidation processes is determined by the partial pressure of oxygen and the vapor pressure of the target material [10]. At the initial stage of evaporation, at low beam power, the vapor pressure of the target material is lower than the partial pressure of oxygen, which leads to the dominance of oxidation processes and, consequently, of dioxide ions of the target material. As the evaporation rate increases, the vapor pressure increases as well, which leads to dominance of dissociation processes and oxide ions. However, when chemically active oxygen is added to the chamber, the total partial pressure of oxygen increases, which prevents the predominance of dissociation and ensures the dominance of dioxide ions in the spectra, regardless of the power of the electron beam.

It is known [11] that after deposition of YSZ coatings by the electron beam method from the vapor phase in a high vacuum, further annealing of the samples is carried out

for several hours at a temperature of 700 °C furnace in an air atmosphere. This technological operation is carried out to restore the color of the ceramic coating surface lost during oxygen deposition. Therefore, from the point of view of coating deposition, the use of a mixture of helium and oxygen as a plasma-forming gas looks very promising, since the surface of the coatings is subject to additional oxidation directly during deposition. a result, As no additional annealing operation of the samples required.

Conclusion

Thus, as a result of the experimental studies, it was established that the use of different gases during the evaporation of the YSZ target at the forevacuum pressures changes the ratio of the amplitudes of the peaks of ions of the target materials oxides and dioxides in the mass. When using helium or a mixture of helium and argon as the working gas, the peaks of target material oxides dominate in the target material ion

spectra. Moreover, their signal increases with the increase in the power of the electron beam. The use of helium and oxygen as a working mixture ensures the dominance of target material dioxide ions at any electron beam power.

The work was carried out with the financial support of the Russian Science Foundation, grant 24-79-10026

(https://rscf.ru/en/project/24-79-10026/)

REFERENCES

- 1. Yushkov Yu. G., Oks E. M., Corbella C., Tyunkov A. V. and Zolotukhin D. B., Ceramics International **46** (4), 4519–4525 (2020).
- 2. Yushkov Y. G., Oks E. M., Tyunkov A. V., Zolotukhin D. B., Yushenko A. Y. and Yushkov A. Y., Ceramics International **46** (13), 21190–21195 (2020).

- 3. Golosov D. A., Zolotukhin D. B., Nikonenko A. V., Oks E. M., Tyunkov A. V., Yushkov Y. G. and Yakovlev E. V., Surface and Coatings Technology **383**, 125241-1–125241-8 (2020).
- 4. Zolotukhin D. B., Lomaev M. I., Oks E. M., Tyunkov A. V. and Yushkov Y. G., Plasma Sources Science and Technology **28** (3), 035018-1–035018-11 (2019).
- 5. Tyunkov A. V., Zolotukhin D. B., Yushkov Yu. G. and Yakovlev E. V., Vacuum **180**, 109573-1–109573-5 (2020).
- 6. Zolotukhin D. B., Tyunkov A. V., Yushkov Yu. G. and Oks E. M., Rev. Sci. Instrum. **86**, 123301 (2015).
- 7. Tyunkov A. V., Yushkov Yu. G. and Klimov A. S. Applied Physics, No. 1, 96–99 (2016) [in Russian].
- 8. Burdovitsin V. A. and Oks E. M., Laser and Particle Beams **26** (4), 619–635 (2008).
- 9. Tyunkov A. V., Burdovitsin V. A., Oks E. M., Yushkov Yu. G. and Zolotukhin D. B., Vacuum **163**, 31–36 (2019).
- 10. Kulikov I. S., Thermal dissociation of compounds. Izd. 2, Moscow, Metallurgy, 1969.
- 11. Kachanov E. B. and Tamarin Yu. A., Technology of light alloys, No. 2, 16–28 (2010).

PLASMA PHYSICS AND PLASMA METHODS

UDC 532.5, 537.39 PACS: 68.03.Hj

EDN: DUFCPP

Effect of electrode immersion depth on the development of pre-breakdown currents in distilled water

V. A. Panov, A. S. Saveliev, Yu. M. Kulikov

This experimental and numerical study covers the velocity field in distilled water, occurring at the pre-breakdown stage when a voltage pulse is applied to a needle electrode at various immersion depths. The obtained results are analyzed in terms of the extremum (maximum) of the flow velocity achieved in the observation area in close proximity to the high-voltage electrode. Satisfactory ratio was obtained between the experimental and numerical dependencies of the velocity extremum over time and the calculations. It showed that the maximum value of velocity in the emerging current is achieved at later times with increasing immersion depth. Decreasing the immersion depth leads to the occurrence of an electric discharge when the high-voltage electrode loses contact with the water due to the stream occurring near it. The conducted study shows the further direction of development of the constructed physical and mathematical model.

Keywords: liquid; electrical breakdown; EHD flows.

DOI: 10.51368/1996-0948-2025-1-31-37

Introduction

The interaction of liquids with plasma generated by electric discharge is a promising area of research, both from a fundamental

Vladislav A. Panov, Senior Staff Scientist, Candidate of Physical and Mathematical Sciences

E-mail: panovvladislav@gmail.com

Andrei S. Saveliev, Senior Staff Scientist, Candidate of Physical and Mathematical Sciences

Yury M. Kulikov, Senior Staff Scientist, Candidate of Physical and Mathematical Sciences

Joint Institute for High Temperatures of the Russian Academy of Sciences

Bd. 2, 13, Izhorskaya st., Moscow, 125412 Russia

Received December 20, 2024 Revised January 20, 2025 Accepted January 27, 2025 Scientific specialty code: 1.3.13 perspective and for numerous practical applications, which include the deposition of functional coatings [1, 2], surface treatment of materials [3, 4], synthesis of nanoparticles and fine powders [5, 6], plasma reactors [7, 8], and purification systems [9].

In many studies, the main plasmaforming medium is a one percent solution of sodium chloride in water. In particular, studies in [10, 11] investigated the parameters of plasma generated by a high-frequency frequency discharge (with a f = 13.56 MHz) between a jet electrolytic electrode and a metal electrode: the chemical composition (including concentration) and thermodynamic properties (rotational and vibrational temperatures of hydroxyl radicals). For a similar electrolyte, experimental studies were conducted to

investigate a discharge with a liquid electrolyte cathode in [12] within a current range of 50-100 mA and an interelectrode distance of 3-4 mm. The occurrence of current pulsations was recorded, which were studied under the assumption of droplet transfer of matter and charges from an aqueous solution into the discharge plasma. Based on the analysis of current oscillograms, the sizes of the resulting drops were estimated. The influence of the bubble structure on the nature of current and voltage pulsations in the discharge was studied in [13]. The authors presented results of experimental studies of an alternating current electric discharge at industrial frequency in a gas-liquid electrolyte medium with bubbles for interelectrode distances of 50-150 mm inside a dielectric tube. Based on the analysis of experimental data, the authors proposed a mechanism for the development of an alternating current electric discharge in a medium with microbubbles.

Experimental studies of alternating current discharge [14] of industrial frequency in a gas-liquid medium made it possible to determine a qualitative mechanism for the development of breakdown and discharge at low pressures. It was found that a gas-liquid medium, saturated with small gas bubbles ranging in size from 1 to 3 mm is formed with a decrease in pressure as a result of boiling and electrolysis. This, in turn, results in a breakdown and rapid ignition of a discharge in the porous medium near the solid electrode. The transition of an electrical discharge with microdischarges into volumetric discharge at reduced pressures has been established.

Paper [15] proposes a physical mechanism for the formation of ring-shaped and semi-ring-shaped plasma structures around an electrolyte jet in a high-frequency discharge with liquid jet electrodes. It is shown that the electric field strength in the region of jet stream decay can reach values of 1–10 MV/m, at which field emission is

possible, leading to the appearance of primary electrons in the vicinity of the jet, which leads to ionization and excitation of molecules of the surrounding gas environment.

In [16], it was determined that the effect of an atmospheric-pressure glow discharge on water results in the formation of hydrated electrons, the generation rate of which increases with the discharge current, while the energy yield remains constant at 0.13 ± 0.01 particles per $100 \, \text{eV}$. Using the acceptor method, the generation rates and energy yields of hydrated electrons in water under the influence of an atmospheric pressure glow discharge were found.

Paper [17, 18] contains measurements of the electrical and spectral characteristics of a discharge with a liquid electrolyte cathode at atmospheric pressure in air within a current range of 20-90 mA. The dependences of the field strength on the magnitude of the discharge current were found for aqueous solutions with different compositions and different pH values, but with the same specific electrical conductivity of 300 µS/cm. It was found that the measured intensity of the glow of the second positive nitrogen system near the surface of the solution in the solutions with discharge for different compositions, different pH values, and electrical conductivity decreases with an increase in the discharge current in the current range from 20 to 100 mA. The rotational and vibrational temperatures determined molecular nitrogen are the same for all experiments and are 2400 and 3800 K, respectively.

An analysis of the completed work shows that the main attention of researchers is focused on the electrophysical and spectral characteristics of discharges, pre-breakdown electrohydrodynamic effects have received much less attention. The development of an electrical breakdown is possible not only as a result of a change in the physical and chemical properties of the stationary environment in which it develops, but also in combination with the phenomena of its transfer and redistribution in the space near the electrodes. The consequence of such a phenomenon may be abnormally low breakdown voltage values [19, 20].

The aim of this work is an experimental and numerical study of the velocity field in distilled water that occurs when a voltage pulse is applied to the needle electrode at different immersion depths. The obtained results are analyzed in terms of the extremum (maximum) of the flow velocity achieved in the observation area in close proximity to the high-voltage electrode.

Experimental setup

In this study, the experimental unit used was described in detail in [21, 22], so only the parameters are presented here. main A cylindrical metal electrode with a diameter of d = 0.85 mm was immersed at different depths in distilled water contained in an optically transparent cube-shaped container with an edge of 8 cm. Using a high-voltage circuit, a pulse with an amplitude of 10 kV was applied to the electrode, causing current to flow through the water, with a rise time of about 100 ns and a duration of less than 1 ms. This caused the formation of a non-stationary liquid flow near the electrode surface. Using the Particle **Image** Velocimetry method, the distribution of two components of the velocity vector of this flow in the plane of the electrode axis was determined. Measurements were carried out for four values of immersion depth h: 1d, 2d, 4d, 8d.

Numerical modeling

Numerical modeling of this problem requires the joint solution of equations belonging to different sections of physics. This circumstance imposes additional requirements on the calculations, namely: the use of a small-time step, splitting into physical processes, and the use of iterative

solvers (Newton's methods with relaxation). The finite element method was used for spatial discretization. Electrostatic effects were described using the equation for electric potential:

$$\nabla \times \vec{D} = \rho_v, \ \vec{E} = -\nabla V, \ \vec{D} = \varepsilon E,$$
 (1)

Where ρ_{v} is the volume density of electric charges, \vec{D} is the electric induction vector, V is the electric potential, \vec{E} is the electric field strength, and ε is the relative penetrability. In the problem under consideration, in addition to bound charges, there are also free charges (anions and cations of water formed during the equilibrium electrolytic dissociation process). To calculate the movement of ions, equations for concentration were solved:

$$\frac{\partial c_i}{\partial t} + \nabla \times (\vec{j} + \vec{u}c_i) = 0, \tag{2}$$

$$\vec{J} = -D_i \nabla c_i - z_i u_{m,i} F c_i \nabla V, \qquad (3)$$

 c_i is concentration of a certain type of particles, \vec{j} is particle flow associated with concentration diffusion of ions and their drift in an electric field, \vec{u} is convective transfer into a liquid flow, D_i is diffusion coefficient, z_i is ion charge, and F is Faraday number. The distribution of free and bound charges determines the volumetric force \vec{F}_{es} acting on the liquid.

$$\vec{F}_{as} = \nabla \times \mathbf{T} + \rho_{v} \vec{E}, \tag{4}$$

$$T_{ij} = -\frac{\varepsilon \varepsilon_0 E^2}{2} \delta_{ij} + \varepsilon \varepsilon_0 E_i E_j$$
 (5)

where **T** is the Maxwell stress tensor, ε_0 is the penetrability of vacuum, and δ_{ij} is the symbol for the Kronecker tensor.

The value of the electrostatic force allows us to find the distribution of velocity

and pressure based on the equations of motion of a viscous incompressible medium

$$\rho \frac{\partial \vec{u}}{\partial t} + \rho (\vec{u} \times \nabla) \vec{u} = \nabla \times [-p\mathbf{I} + \mathbf{K}] + \vec{F}_{es}$$
 (6)

$$\frac{\partial \rho}{\partial t} + \nabla \times (\rho \vec{u}) = 0, \tag{7}$$

which are supplemented by relations for the barotropic fluid $\rho(p) = \frac{p}{c^2} + \rho_0$, of the stress

tensor
$$\mathbf{K} = \mu \left(\nabla \vec{u} + (\nabla \vec{u})^T \right) - \frac{2}{3} \mu \left(\nabla \times \vec{u} \right) \mathbf{I}.$$

Splitting by physical processes leads to the following algorithm for calculating unknowns at the new time layer: (1) – the speed and pressure are found using the known electric field and charge distribution, (2) – the concentration of positive ions is calculated, (3) – the concentration of negative ions is found. Based on the new velocity field and the distribution of free charges, a new distribution of the electric field is determined (4).

For time iteration, an implicit method with second order approximation and variable step is used. To find a solution to a linearized system of equations, Newton's method is used. For each group of unknowns, the parameters of the Newton method are adjusted individually to ensure accelerated convergence.

Results and discussion

Experiments and calculations were carried out at the same values of the electrode immersion depth (h = 1d, 2d, 4d, 8d).

Figure 1 shows the dependence of the maximum average velocity in the observed region, normalized to the value at late times of the flow. It is evident that the velocity recorded in the experiment (curves 1 and 3) in the initial interval of flow development up to 30 µs significantly exceeds the values

obtained as a result of numerical modeling (curves 2 and 4). One of the reasons for the differences may be the influence of the moving interphase boundary (water-air), while in the calculation the interface surface of the media is fixed. The significant discrepancy at the initial moment of time may probably also be a consequence of the fact that the PIV method has difficulty measuring the velocity in a small vicinity of the electrode due to the relatively small number of particles in this region. When the electrode was immersed to a depth of h = d at times exceeding 256 µs after the start of the current pulse, a drop in the water level below the electrode was observed, which led to the formation of an air gap between them and a spark discharge, which significantly altered the flow pattern near the electrode. A similar effect was observed at longer time values during immersion to a depth of h = 2-4d. In this regard, time measurements are limited to 1 μ s.

With an increase in the immersion depth to h = 2d (see Fig. 1, curves 3 and 4), satisfactory agreement between the curves observed at late calculation A distinctive feature of curve (2) is the velocity oscillations, which are caused by the existence of large-scale vortices propagating downwards through computational the domain. These vortices are one of the features of the axially symmetric model, since in the experiment, when moving away from the rod, three-dimensional evolution of these structures is observed (leading to the disintegration of vortices into smaller ones).

Figure 2 shows an instantaneous picture of water flow near the electrode at a time of 256 μ s. The axis x = 0 coincides with the axis of the electrode, and the straight line y = 46.5 mm coincides with its edge. The color shows the modulus of the velocity vector normalized to the maximum flow velocity, which is achieved at later times, and the arrows show the direction of fluid movement. It is evident that the flow in the

near-electrode region at the end of the rod is vortex, and, due to the presence of some arbitrary vorticity field in the liquid, as well as the non-uniformity of the distribution of the electric potential in the vicinity of the end of the rod, it is three-dimensional.

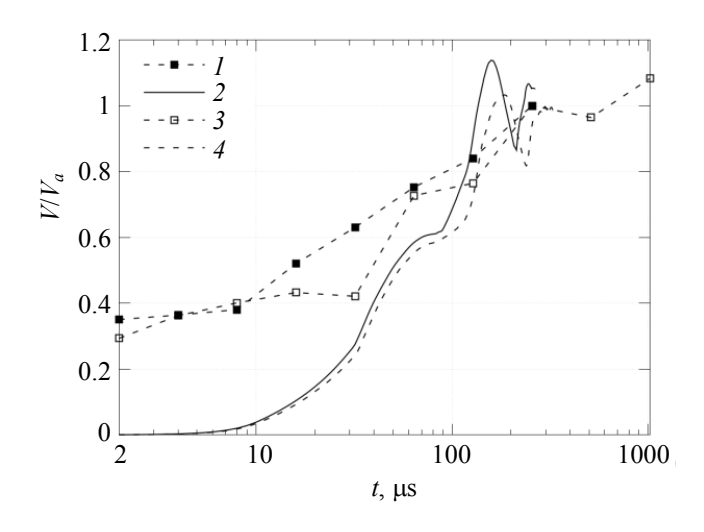


Fig. 1. Reduced maximum flow velocity at rod immersion depth h = 1d: experiment (1) and modeling (2), and depth h = 2d: experiment (3) and modeling (4)

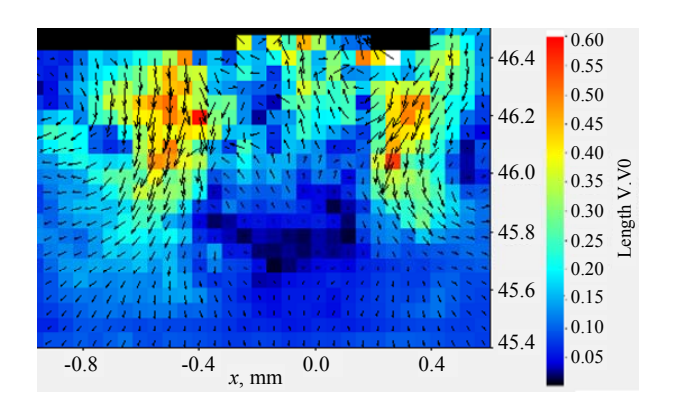


Fig. 2. Velocity field near the needle surface at 256 µs after the current pulse is applied

The best agreement between the modeling results and the experiment in the vicinity of $t = 100 \,\mu s$ is observed for the case of h = 4d (Fig. 3), while the calculated curve of the reduced velocity similarly experiences oscillations. For the case of h = 8d, the reduced velocity obtained in the calculation exceeds the experimental result.

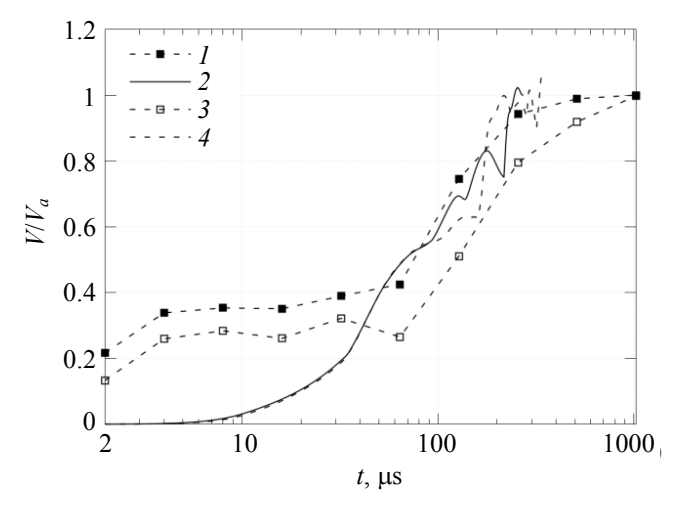


Fig. 3. Reduced maximum flow velocity at rod immersion depth h = 4d: experiment (1) and simulation (2), and depth h = 8d: experiment (3) and simulation (4)

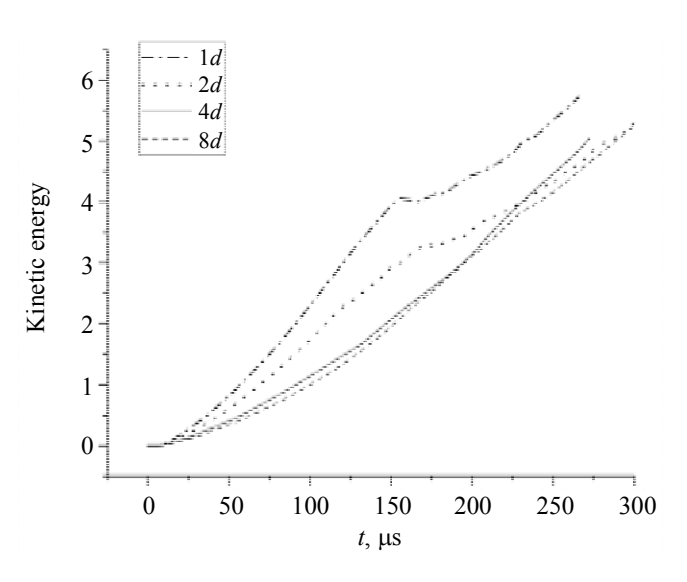


Fig. 4. Dependence of the reduced kinetic energy of the flow on time at different rod immersion depths. Processing of modeling results

The experimental results were obtained in the vicinity of the electrode, which makes it difficult to introduce integral quantities often considered in theory. Therefore, the behavior of kinetic energy, one of the integrals of the system, is considered based on the results of numerical modeling. Figure 4 shows the values of kinetic energy reduced to the value for h = 8d at t = 100 µs (the end of the interval of regular behavior of the curves). It is evident that increasing the depth

of immersion of the rod leads to a decrease in the kinetic energy of the system. This can be explained as follows. A shallow immersion depth leads to a higher concentration of the electric field around the electrode tip, and thus to a greater electrostatic force acting on an elementary volume of liquid, resulting in a faster acceleration of the fluid. In this case, the maximum value of velocity in the emerging current is achieved at later times with increasing immersion depth.

Conclusion

An important role in the process of movement of the horizontal interphase boundary in the vertical electric field is played by disturbances in the water, propagating at the speed of sound when voltage is applied. These disturbances deform the water-air interface, which leads to the emergence of a large-scale flow directed from the bottom up along the This experimental fact requires considering the mobility of this boundary and the effects of surface tension. The double layer that forms around the metal electrode even before voltage is applied requires special attention. This layer results in small-scale (on the order of 100 nm) and highly significant (40–45 times) non-uniformity in the dielectric penetrability of water, which additional requirements on the grid resolution of the near-electrode zone. Applying voltage to the electrode leads to charge separation in near-electrode region and the deprotonation, and also activates a number of nonlinear effects in areas of particularly strong electric fields on the sharp edges of the electrode, which are characteristic of polar liquids in general and water in particular, non-equilibrium electrolytic dissociation of water, and non-linear transport of protons. In addition, it is very difficult to consider the penetration of atoms and microscopic fragments of the electrode into the nearelectrode layers of the liquid.

The model proposed in the study is essentially non-linear both in space (in the near-electrode layer) and in time and forms a system with positive feedback: applying a high-voltage potential to the electrode needle results in an increase of the ion concentration (by several orders of magnitude during the calculation time) and shielding. Shielding, in turn, results in an increase in the electric field and its gradients, and, ultimately, to an increase in the amplitude of the volume force acting on the liquid. However, in order to break this connection, as well as to consider the propagation of disturbances along the boundary, it is recommended to further develop a special "near-electrode" model of a compressible continuous medium that correctly considers the various nonlinearities listed.

REFERENCES

- 1. Paulmier T., Bell J. M. and Fredericks P. M., Thin Solid Films **515**, 2926 (2007).
- 2. Quan C. and He Y., Surf. Coat **269**, 319 (2015).
- 3. Meletis E. I., Nie X., Wang F. L. and Jiang J. C., Surf. Coat. Technol. **150**, 246 (2002).
- 4. Ishijima T., Nosaka K., Tanaka Y., Uesugi Y., Goto Y. and Horibe H., Appl. Phys. Lett. **103**, 142101 (2013).

https://doi.org/10.1063/1.4823530

- 5. Wüthrich R. and Allagui A., Electrochim. Acta 55, 8189 (2010).
- 6. Abdul K. T. and Kaliani A., Ionics **18**, 315 (2012).
- 7. Becker K. H., Schoenbach K. H. and Eden J. G., J. Phys. D: Appl. Phys. **39**, R55 (2006).
- 8. Gao S. Z., Ma D., Lu Q., Li Y., Li X. and Yang W., Plasma Chem. Plasma Process. **30**, 873 (2010).
- 9. Son E. E., Sadriev R. Sh., Gaisin Al. F., Bagautdinova L. N., Gaisin F. M., Shakirova E. F., Akhatov M. F., Gaisin Az. F. and Kayumov R. R., High Temperature **52**, 939 (2014).
- 10. Gaisin A. F., Gaisin F. M., Zheltukhin V. S. et al., Plasma Phys. Rep. **48**, 48 (2022).
- 11. Kayumov R. R., Kuputdinova A. I., Mirkhanov D. N. et al., Plasma Phys. Rep. **50**, 115 (2024).

- 12. Tazmeev G. K., Tazmeev A. K. and Tazmeev K. K., Applied Physics, No. 3, 33 (2023) [in Russian].
- 13. Valiev R. I., Khafizov A. A., Bagautdinova L. N. et al., High. Temp. **60**, Suppl. 1, 127–130 (2022).
- 14. Khafizov A. A., Valieva R. I., Bagautdinova L. N., Gaisin Az. F., Gaisin Al. F., Gaisin F. M., Sond E. E. and Fakhrutdinova I. T., High Temp. **60** (4), 570 (2022).
- 15. Zheltukhin V. S., Gaisin A. F. and Petryakov S. Y., Technical Physics Letters, No. 9, 22 (2022).
- 16. Khlyustova A. V. and Titov V. A., Applied Physics, No. 6, 48 (2015) [in Russian].
- 17. Chistolinov A. V., Tyuftyaev A. S. and Gadzhiev M. Kh., Applied Physics, No. 5, 5 (2021) [in Russian].

- 18. Chistolinov A. V., Yakushin R. V. and Perfilieva A. V., Applied Physics, No. 1, 12 (2022).
- 19. Panov V. A., Kulikov Yu. M., Pecherkin V. Ya., Vasilyak L. M. and Saveliev A. S., Applied Physics, No. 6, 5 (2023) [in Russian].
- 20. Panov V. A., Kulikov Yu. M., Vetchinin S. P., Pecherkin V. Ya. and Vasilyak L. M., Plasma Sources Sci. Technol. **32** (9), 095020 (2023).
- 21. Panov V. A., Saveliev A. S., Pecherkin V. Ya., Vasilyak L. M. and Kulikov Yu. M., Journal of Communications Technology and Electronics **68**, Suppl. 2, 170–175 (2023).
- 22. Panov V. A., Saveliev A. S. and Kulikov Yu. M., Applied Physics, No. 4, 89 (2024) [in Russian].

= PHOTOELECTRONICS =

UDC 621.383.4/5 PACS: 42.79.Pw, 85.60.Gz, EDN: GYMBFM 07.57.Kp, 85.60.Dw

MWIR focal plane array based on CdHgTe nBn-architecture with superlattice barrier layer

K. O. Boltar, I. D. Burlakov, N. I. Iakovleva, M. V. Sednev, A. V. Trukhachev, N. A. Irodov, A. A. Lopukhin, E. V. Permikina, A. V. Voitsekhovskii, D. I. Gorn, N. N. Mikhailov

Medium wavelength IR focal plane array (FPA) based on CdHgTe nBn-architecture with superlattice barrier layer has been developed and investigated. The FPA consists of 64×64 elements with 40 µm pith, hybridized with silicon readout integrated circuit (ROIC). The photosensitive assembly of FPA and ROIC was measured in a vacuum cryostat filling liquid nitrogen. The spectral and photoelectric parameters of CdHgTe FPAs based on nBn architecture with superlattice barrier layer have been measured under optimal bias conditions. The average detectivity value was of $D^*\sim7\times10^{10}$ cm $W^{-1}Hz^{1/2}$, the average voltage sensitivity value was of $S_u\sim6\times10^7$ V/W.

Keywords: FPA, *n*B*n*, heterostructure; MWIR; HgCdTe; MCT; photosensitive element; spectral response.

DOI: 10.51368/1996-0948-2025-1-38-44

1. Introduction

The development of epitaxial growth methods of $Cd_xHg_{1-x}Te$ material, primarily molecular beam epitaxy (MBE), has enabled to solve a number of technological problems in creating high-operating-temperature focal plane arrays (FPAs) and photodetectors [1, 2], including the development of design and topology for CdHgTe multilayer barrier heterostructures with superlattices as the barrier.

The layer with a unipolar conductivity type, forming *n*B*n* heterostructures, ensure the minimal dark currents of photosensitive elements [3–5]. Based on *n*B*n* heterostructure FPAs with photosensitive elements, separated by the mesa-etching method to individual

elements, do not contain any *p*-type regions, while the array elements operate like ordinary photodiodes, by applying bias to the base and contact layers.

The development of new barrier architectures based on CdHgTe unipolar *n*B*n* heterostructures including superlattices as the barrier for MWIR and LWIR FPAs and photodetectors, is considered as a very important problem [6, 7], which solving could improve the production of new type devices with a small number of defects, increase operating temperature and make better performance.

The paper discusses the concept of MWIR FPA design based on CdHgTe *n*B*n* heterostructure with superlattice as a barrier. CdHgTe FPAs with various topologies

Table 1

including absorbing *n*-layers were manufactured on the basis of barrier nBn heterostructures with superlattices spectral and photovoltaic barriers. The characteristics of MWIR CdHgTe devices based nBnheterostructures with on superlattices barriers as have been investigated.

2. Architecture of CdHgTe-based nBn barrier structures

Cd_xHg_{1-x}Te multilayer nBn heterostructures were grown using the MBE method on optically transparent GaAs (013) substrates at the Institute of Semiconductor Physics of the Siberian Branch of the Russian Academy of Sciences [8, 9]. A ZnTe buffer layer (~ 30 nm), a relaxing CdTe buffer layer (5.5 μ m), and a graded-gap Cd_xHg_{1-x}Te layer (1 μ m) were successively formed on the substrate. The active working region of the

 $Cd_xHg_{1-x}Te$ nBn structure consisted of an absorbing layer, a barrier layer, and a contact layer (Fig. 1). The absorbing $Cd_xHg_{1-x}Te$ layer was of approximately 3–4 µm thickness. The CdTe composition in the barrier layer and in the contact layer of ~ 1 µm thickness has been selected in accordance with the operating spectral range.

Contact n+-layer CdHgTe, thickness 0.5 µm

Superlattice based barrier layer

Absorbing n-layer CdHgTe, thickness 3–4 µm

Graded-gap base CdHgTe

CdTe buffer layer, thickness 5.5 µm

ZnTe buffer layer, thickness 0.03 µm

Optically transparent GaAs (013) substrate

Fig. 1. Layer-by-layer configuration of CdHgTe nBn-barrier structure with a superlattice

The layer-by-layer configuration of MWIR CdHgTe barrier *n*B*n* structure with a superlattice is presented in Table 1.

Parameters of layers of nBn heterostructure based on CdHgTe

Name of the layer in the structure	Concentration, cm ⁻³	Composition, mole fraction	Thickness, μm
n-Cd _{x} Hg _{1-x} Te contact layer	$n \sim (1-3) \times 10^{16}$	0.3	0.5
<i>n</i> -Cd _x Hg _{1-x} Te contact layer		0.03 (well) / 0.75 (barrier).	0.004 (barrier) / 0.010 (well); 10 periods 0.140 (total)
Cd_xHg_{1-x} Te absorbing n -layer	$n \sim (3-5) \times 10^{15}$	0.3	3.0-4.0
Graded-gap base CdHgTe	_	1.0-0.3	1.0
CdTe buffer layer	-	-	5.5
ZnTe buffer layer	_	_	0.03
GaAs (013) substrate, Ø 50.8 mm			600

During the growing process, the doping of the working area was carried out with a donor indium impurity, the concentration of the impurity in the absorbing and barrier layers was approximately the same, and in the contact layer it was several times higher.

The composition profile of the CdHgTe nBn heterostructure with the barrier region

consisting of 10-period superlattice, is shown in Fig. 2.

As shown in Figure 2, in the $Cd_xHg_{1-x}Te$ multilayer heterostructure, from left to right starting from the absorbing layer of composition x = 0.28 mole fraction, there is a 10-periods superlattice consisting of $HgTe/Cd_xHg_{1-x}Te$ layers, while the

wide-band layer is $Cd_xHg_{1-x}Te$ of composition x = 0.72 mole fraction, the well layer is formed by a semi-metallic HgTe binary compound, the barrier layer is approximately

4 times smaller thickness than the HgTe layer, and a contact layer of composition x = 0.3 mole fraction is grown on top of the barrier layer.

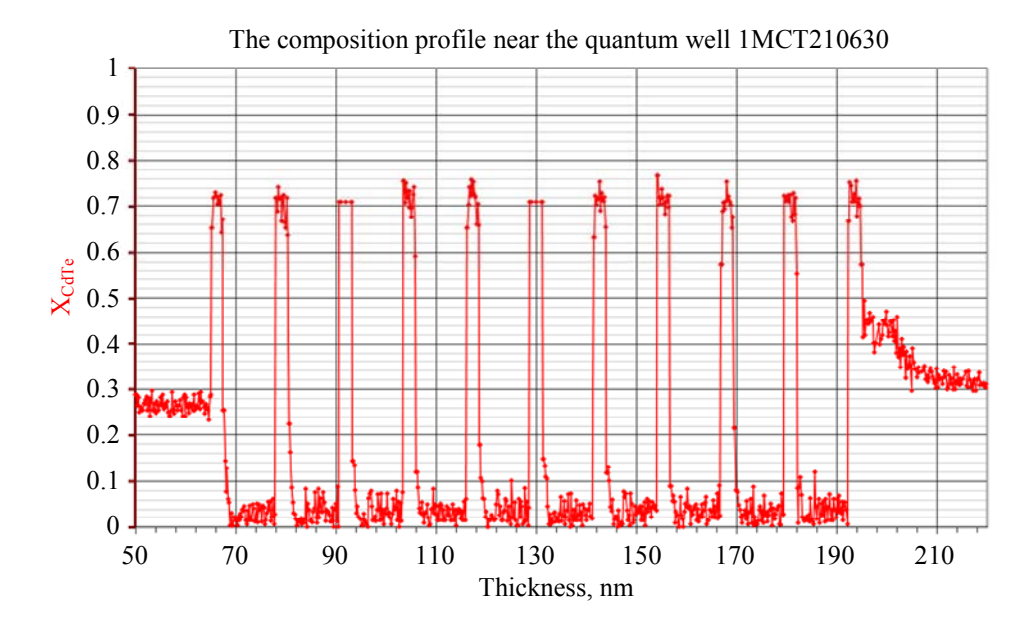


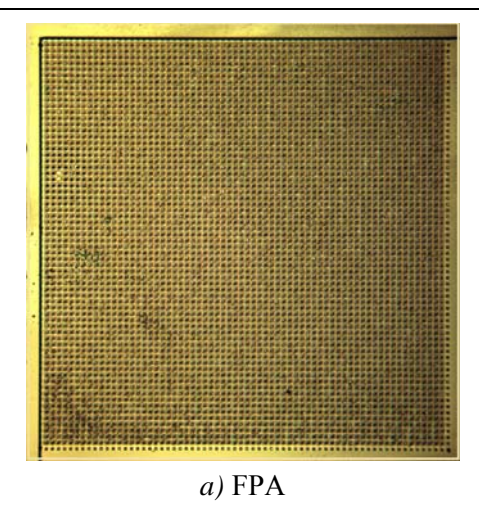
Fig. 2. The composition profile in the CdHgTe nBn heterostructure with the 10-period superlattice barrier.

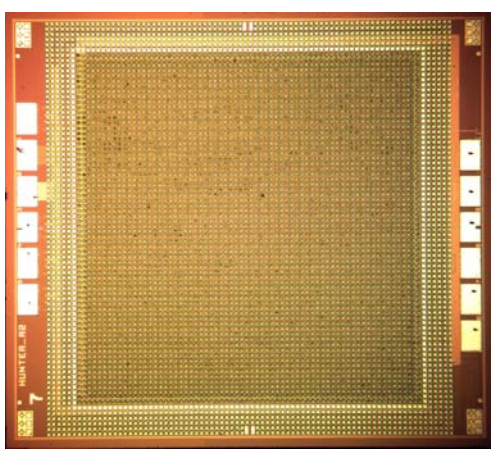
3. Research and discussion of results

MWIR FPAs and matrix photodetectors were fabricated on the basis of CdHgTe nBn heterostructures with superlattices as the barrier. The 64×64 format with a 40 µm pitch arrays of photosensitive elements were mesa-etching formed using method. The crystal with the 64×64 element array had overall dimensions of ~2.74×2.74 mm (Fig. 3a). The local size of the contact nregion was 0.02×0.02 mm, and an ohmic In fabricated for microcontacts were photosensing element by photolithography method.

A silicon ROIC (Fig. 3b) intending for reading, pre-analog processing and output signals from a 64×64 element array provided an accumulation of photocurrent on integrating capacitors and multiplexing of signals into 2 analog outputs. The hybrid assembly of FPA and ROIC obtained by the flip-chip method was located in a vacuum cryostat for detecting a photosignal at an operating temperature of T = 77 K.

The current-voltage characteristics of test array elements were measured at T = 300 K (Fig. 4), and the relative spectral response have been measured at T = 77 K (Fig. 5).





b) 64×64 element ROIC

Fig. 3. 64×64 element with 40 µm pitch FPA and 64×64 element ROIC

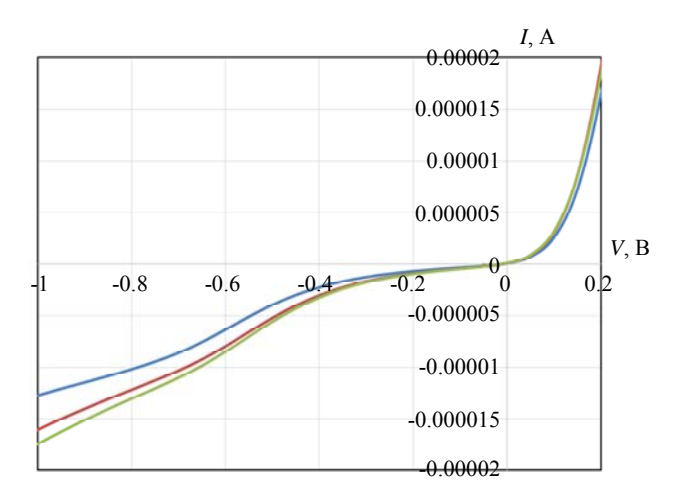


Fig. 4. Current-voltage characteristics of test elements of a 64×64 element FPA with of 40 μ m pitch for the MWIR spectral range (3–5 μ m) at $T=300~{\rm K}$

The current-voltage characteristic of MWIR FPA (Fig. 4) differs from current-voltage characteristic of n/p photodiode due to its unipolar nature. The presented current-voltage characteristic under forward bias voltage determines the dark current generated in the collector volume, while under reverse bias voltage, it is generated in the base layer volume. In the absorption region, the doping level was of $N_d \sim 3 \times 10^{15}$ cm⁻³, the lifetime was of $\sim 10^{-5}$ s, and the absorption region thickness was of $\sim 3-4$ µm. The flat-band voltage was approximately $V_{fb} \approx -0.2$ V. The generation-recombination current in the depletion region appeared at bias voltages

 $V > V_{fb}$, while the tunneling current occurred at bias voltages $V > V_{fb} + E_{g} \approx (0.2 + 0.25) \text{ V}$. The tunneling mechanism is caused by traps with a trap concentration of approximately $N_{t} \sim 10^{11} \text{ cm}^{-3}$.

The components of the dark current for the FPA based on an *n*B*n* structure with a barrier layer are identical to the current components that determine the behavior of charge carriers in a photodiode, except for the tunneling current, which changes due to the presence of the barrier (it is small at low biases but increases with higher bias voltages).

The relative spectral response of the test PSE at T = 77 K is shown in Figure 5.

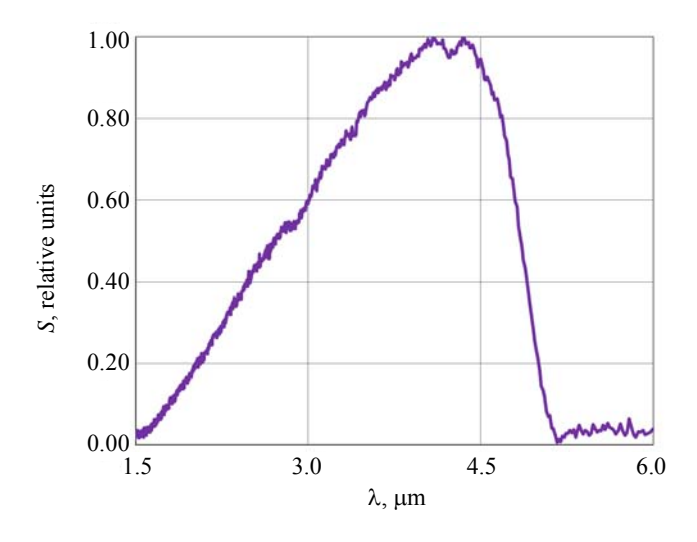


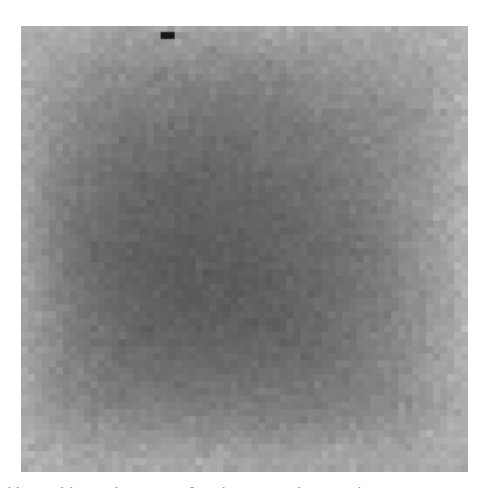
Fig. 5. Relative spectral response of the test array element at T = 77 K, $\lambda_{gr} = 4.88$ μ m

The long-wavelength cutoff of the spectral response at a 0.5 level for MWIR FPA was of $\lambda_{gr} = 4.88 \, \mu m$, it was formed by the choice of the $Hg_{1-x}Cd_xTe$ composition, and the short-wavelength cutoff at a 0.5 level was of $\lambda_k = 2.72 \, \mu m$, that determined by the absorption of radiation in the graded-gap layer of the nBn heterostructure with $\sim 1 \, \mu m$ thickness.

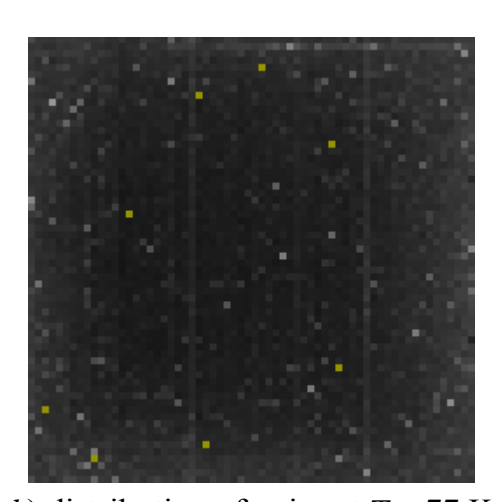
To measure the performance of 64×64 FPA with a 40 µm pitch based on nBn heterostructures, an computer-aided and processing system was used, which allowed to the automatic measurement of the noise

and photosignal voltages of each array element and the following performance calculation. Measurements of the photosignal and noise voltages of MWIR FPA were carried out; the distributions of the photosignal and noise are presented in Figure 6 *a*, *b*.

The performance of the 64×64 MWIR FPA with 40 µm pitch based on CdHgTe *n*B*n* heterostructures were compared with the performance of the InSb FPA based on bulk material with a relative aperture of the cooled diaphragm of 1:0.9 (Table 2).



a) distribution of photosignal at T = 77 K



b) distribution of noise at T = 77 K

Table 2

Fig. 6. Signal and noise distributions of the MWIR 64×64 FPA with 40 µm pitch based on the HgCdTe nBn heterostructure

Performances of the 64×64 FPAs with 40 μm pitch

FPA No.	Integration time, µs	Cutoff wavelength, µm	Volt sensitivity, S_u , V/W	Detectivity D^* , cm·Hz ^{1/2} ·W ⁻¹
FPA1	99	4.88	5.2×10 ⁷	6.7×10^{10}
FPA2	99	4.92	6.4×10 ⁷	7.4×10 ¹⁰
FPA-InSb	120	5.48	1.0×10 ⁸	8.8×10 ¹⁰

From the table and graphs it is evident that the diagrams of distribution of signal and noise voltage for 64×64 arrays, as well as the average values of the main performance, confirm the possibility of creating FPAs and

PDs based on HgCdTe *n*B*n* heterostructures with superlattices as a barrier. The low values of the detectivity, obtained at the first stage of the research, indicate the need to redesign and the further development of the technology

both in mesa-array passivation and in growing HgCdTe *n*B*n* heterostructures with wide-gap barriers.

4. Conclusion

Using the molecular beam epitaxy method, CdHgTe multilayer nBn heterostructures with an absorbing n-layers and with superlattices as a barriers were obtained for the production of focal plane arrays of a new design and topology. The photodetectors and 64×64 FPAs and with $40~\mu m$ pitch have been manufactured and investigated.

The current-voltage characteristics of the test elements of MWIR FPAs at the low-voltage bias were measured at normal climatic conditions. The results of the current-voltage characteristic measurements at T = 300 K showed that the components of the dark current for a FPA based on an nBn structure with a barrier layer are identical to the components that determine the behavior of charge carriers in a p/n photodiode, except for the tunnel current, which changes under the influence of the barrier layer. The spectral responses of the MWIR FPAs with a long-wave cutoff of $\lambda_{0.5} \sim 4.9 \,\mu\text{m}$, which corresponds to the atmospheric transparency window.

The average value of detectivity for the FPA1 was of $D_1^* = 6.7 \times 10^{10} \text{ cm} \cdot \text{W}^{-1} \cdot \text{Hz}^{1/2}$. The average value of the volt sensitivity S_u for the FPA1 was of $S_{u1} = 5.2 \times 10^7 \text{ V/W}$. The average value of detectability for the FPA2 was $D_1^* = 7.4 \times 10^{10} \text{ cm} \cdot \text{W}^{-1} \cdot \text{Hz}^{1/2}$. The average value of the volt sensitivity S_u for the FPA2 was $S_{u2} = 6.4 \times 10^7 \text{ V/W}$. The difference in number of defects and detectivity values D_1^* for different FPAs are connected with the quality of FPA surface passivation. To improve the performance,

further development of the technology both in FPA production and in growth processes improvement of HgCdTe *nBn* heterostructures with a superlattice as a barrier are required.

The study was supported by a grant from the Russian Science Foundation No. 23-62-10021, https://rscf.ru/project/23-62-10021.

REFERENCES

- 1. Boltar K. O., Burlakov I. D., Iakovleva N. I., Vlasov P. V., and Lazarev P. S., Usp. Prikl. Fiz. (Advances in Applied Physics) **10** (2), 170–182 (2022) [in Russian].
- 2. Piotrowski J. and Rogalski A. High-Operating-Temperature Infrared Photodetectors, SPIE Press, Bellingham, 2007.
- 3. Izhnin I. I., Kurbanov K. R., Voitsekhovskii A. V., Nesmelov S. N., Dzyadukh S. M., Dvoretsky S. A., Mikhailov N. N. and Sidorov G. Y., Appl. Nanosci. **10**, 4571–4576 (2020).
- 4. Akhavan N. D., Umana-Membreno Gu. R., Antoszewski J. and Faraone L., IEEE Trans Electron. Dev. 65, 591–598 (2018).
- 5. Itsuno A. M., Phillips J. D. and Velicu S., Journal of Electronic Materials **40** (8), 1624–1629 (2011).
- 6. Voitsekhovskii A. V., Nesmelov S. N., Dzyadukh S. M., Vasil'ev V. V., Varavin V. S., Dvoretsky S. A., Mikhailov N. N., Yakushev M. V. and Sidorov G. Yu., Applied Physics, No. 4, 83–86 (2016) [in Russian].
- 7. Kopytko M. et al., J. Electron. Mater. **44** (1), 158–166 (2015).
- 8. Voitsekhovskii A. V., Nesmelov S. N., Dzyadukh S. M., Dvoretsky S. A., Mikhailov N. N., Sidorov G. Yu. and Yakushev M. V., Infr. Phys. and Techn. **102**, 103035 (1–4) (2019).
- 9. Varavin V. S., Sabinina I. V., Sidorov G. Yu., Marin D. V., Remesnik V. G., Predein A. V., Dvoretsky S. A., Vasilyev V. V., Sidorov Yu. G., Yakushev M. V. and Latyshev A. V., Infrared Phys. Technol. **105**, 103182 (2020).

doi: 10.1016/j.infrared.2019.103182.

Konstantin O. Boltar^{1,2}, Head of Scientific and Technical Complex, Doctor of Physical and Mathematical Sciences, Professor

Igor D. Burlakov^{1,3}, Deputy Director General for Innovations and Science, Doctor of Technical Sciences, Professor

Natalia I. Iakovleva¹, Chief Staff Scientist, Doctor of Technical Sciences

E-mail: niiakovleva@mail.ru

Mikhail V. Sednev¹, Head of the Site, Candidate of Technical Sciences

Anton V. Trukhachev¹, Lead Engineer

Nikita A. Irodov¹, Head of the Site

Alexey A. Lopukhin¹, Head of the Site, Candidate of Technical Sciences

Elena V. Permikina¹, Lead Process Engineer Alexandr V. Voytsekhovsky⁴, Head of Department, Doctor of Physical and Mathematical Sciences Dmitry I. Gorn⁴, Head of the Laboratory, Candidate of Physical and Mathematical Sciences E-mail: gorn_dim@sibmail.com

Nikolay N. Mikhaylov⁵, Senior Staff Scientist, Candidate of Physical and Mathematical Sciences ¹ RD&P Center ORION, join-stock company

9, Kosinskaya st., Moscow, 111538 Russia

² Moscow Institute of Physics and Technology

9, Institutskiy lane, Dolgoprudny, Moscow region, 141701 Russia

MIREA – Russian Technological University
 Vernadskogo Ave., Moscow, 119454 Russia
 Tomsk State University

36, Lenina st., Tomsk, 634050 Russia
⁵ Rzhanov Institute of Semiconductor Physics of the Siberian Branch of the Russian Academy of Sciences 13, Akademika Lavrentyeva Ave., Novosibirsk, 630090 Russia

Received December 12, 2024 Revised December 27, 2024 Accepted February 7, 2025 Scientific specialty code: 1.3.11

© K. O. Boltar, I. D. Burlakov, N. I. Iakovleva, M. V. Sednev, A. V. Trukhachev, N. A. Irodov, A. A. Lopukhin, E. V. Permikina, A. V. Voytsekhovsky, D. I. Gorn, N. N. Mikhaylov, 2025

PHOTOELECTRONICS =

UDC 621. PACS: 85, 85.60.–q

EDN: AYVMCY

Uncooled 640×512 photosensor array for the spectral range of 0.4–2.0 μm from colloidal quantum dots PbS with a hole transport layer based on *p*-PbS-EDT CQDs

V. P. Ponomarenko, V. S. Popov, M. A. Pankov, K. A. Khamidullin, A. D. Deomidov, A. A. Fedorov, G. Yu. Deev, D. E. Dragunov, O. V. Epifanov, P. S. Lazarev, E. V. Mirofyanchenko, D. V. Ilyinov, V. A. Petrushina, I. D. Burlakov, A. V. Polessky, V. V. Startsev, S. B. Brichkin, M. G. Spirin, S. A. Tovstun, M. V. Gapanovich, V. Yu. Gak, A. V. Gadomskaya, D. N. Pevtsov, A. V. Katsaba, A. S. Kirichenko, D. V. Dyomkin, V. A. Ivanova, V. V. Ivanov, V. F. Razumov

The architecture and main characteristics of the 640×512 photosensor array (15 µm pitch) with spectral range sensitivity of 0.4–2.0 µm developed on the basis of PbS colloidal quantum dots are presented. The layer for generating the main fraction of photocarriers is made on the basis of n-PbS CQDs by replacing the initial ligand (oleic acid) with iodine during the treatment of the CQD layer with tetra-n-butylammonium iodide (TBAI). Transport layers for electrons and holes were produced based on n-ZnO and p-PbS EDT CQDs, where the hole transport layer of p-PbS-EDT CQDs was created by replacing the initial ligand by treating the CQD layer with ethane-1,2-dithiol (EDT).

Keywords: colloidal quantum dot; photosensor; ligand; photosensitivity.

DOI: 10.51368/1996-0948-2025-1-45-54

1. Introduction

The unique properties of low dimensional semiconductor structures increasingly attract attention of researchers in fields as photonics, biomedicine, microelectronics, etc. Recently, the progress reached with the use of quasi-zerodimensional quantum dots in the creation of solar energy devices [1], biomarkers [2], focal plane arrays (FPA) [3], lasers [4], etc., is particularly noticeable.

Currently, there are two companies leading the industrial production of optoelectronics using colloidal quantum dots:

SWIR Vision (USA) and Quantum Solutions (UK), which mass-produce wide-spectrum full-format photosensors array and night video cameras based on them with a photosensitivity range from 0.4 to 2.0 µm, manufactured using hybrid-monolithic **SWIR** technology. In 2020, Vision demonstrated uncooled 640×512, 1280×1024, and 1920×1080 FPA, on lead sulfide colloidal quantum dots with a photosensitive element (PSE) pitch of 15 µm. Currently, company's product line includes 5 types of photosensor arrays, including and 3064×2040 photosensors of the with a PSE pitch of $7 \, \mu m$. In 2024, Quantum Solutions introduced a 640×512 FPA made of lead sulfide colloidal quantum dots with the smallest pitch of $5 \, \mu m$ achieved to date in industrial samples of IR FPA. Both companies produce compact night vision cameras using self-engineered FPAs made from colloidal quantum dots.

Previously, in [5], we described a single-element photosensor developed by us for the spectral range of 0.4–2.0 µm, made of colloidal PbS nanoparticles on a Si/SiO₂ substrate with the architecture shown Figure 1*a*. Small-sized $12\times12~\mu m$ in photosensitive elements of diode type with an energy barrier of the p-n junction type at the contact of layers of colloidal quantum dots (CQD) of lead sulfide (PbS) of *n*- and *p*-type conductivity were studied. The p-n junction was obtained energy barrier modifying the CQD surface with appropriate ligands. The PbS CQD layer of the electron conductivity type (n-type) was created by replacing the initial ligand used in the synthesis of CQDs (oleic acid C₁₈H₃₄O₂) with iodine (I) by treating the PbS CQD layer with tetra-n-butylammonium iodide [(C₄H₉)₄N]I (TBAI). Similarly, a p-type PbS CQD layer was created by replacing the original ligand after treating the PbS CQD layer with ethane-1,2-dithiol $C_2H_6S_2$ (EDT). The absorption of radiation from the spectral interval of 0.4–2.0 µm was mainly performed *n*-PbS-TBAI the CQD electronic conduction type layer due to its significantly

greater thickness compared to the *p*-PbS-EDT CQD layer. The *p*-PbS-EDT CQD layer was used as an electron blocking layer near the anode of the photosensitive structure and, at the same time, served as a hole transport channel.

The PbS CQD for I- and p-type conductivity layers had a diameter of 7.6 nm and 3.1 nm, respectively, which created an additional energy heterobarrier at the contact of these layers, facilitating the efficient separation of photocarriers formed after the decay of photoexcitons in the n-PbS-TBAI CQD layer. Lead chloride (PbCl₂) used as the lead precursor and N,N'-diphenylthiourea (SC(NHPh)₂) was used as the sulfur precursor. A layer of n-ZnO nanoparticles with electron conductivity served as a layer for blocking the flow of holes in the area near the cathode and, at the same time, as a channel for transporting electrons to the cathode. The upper radiationtransparent electrode was created by aerosol printing of a layer based on silver nanowires (AgNW), with an optical transmittance in the wavelength range of 0.4–2.0 µm of about 65-70 % and high conductivity [6], which conductive sets them apart from coatings made of carbon nanowires or ITO $(In_2O_3)_{0.9}$ - $(SnO_2)_{0.1}$ (see Fig. 1b). Thus, the architecture of the photosensors developed in [5] had the form Cr/Ni/n-ZnO/n-PbS-TBAI CQD/p-PbS-EDT CQD/AgNW. The energy structure of the individual layers of this structure is shown in Figure 2.

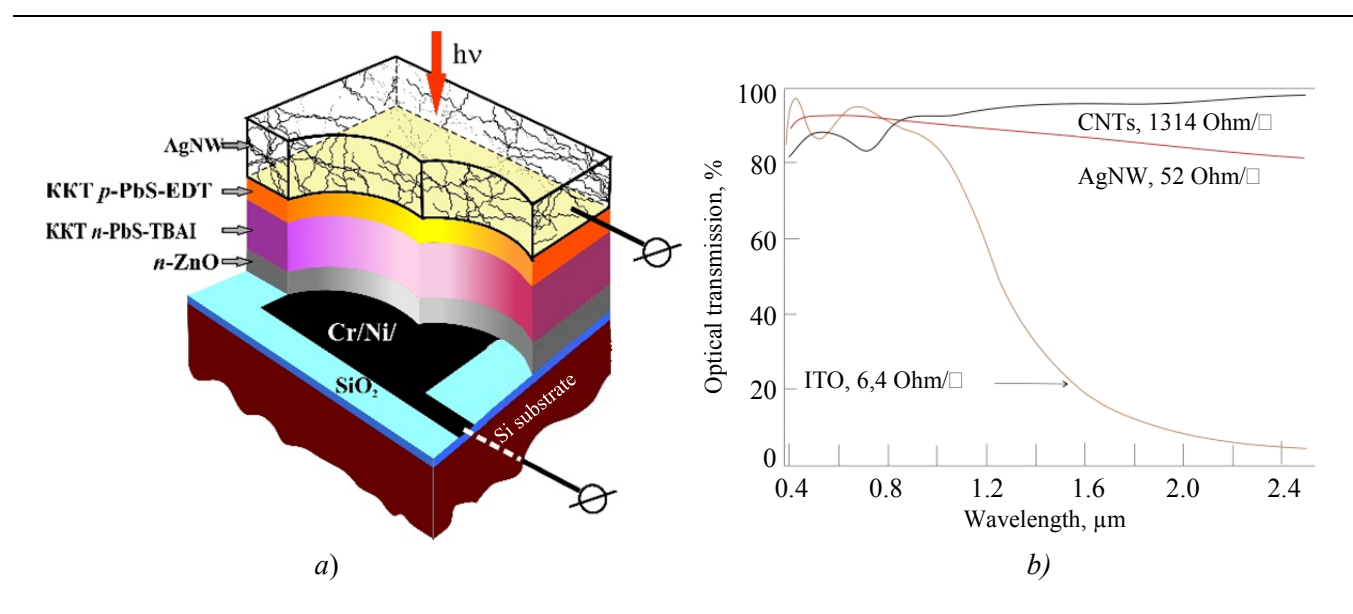


Fig. 1 Single-element photosensor based on colloidal quantum dots PbS CQD with transport layers for electrons and holes made of n-ZnO nanoparticles and p-PbS-EDT CQD, respectively: a) – photosensor architecture [5]; b) – optical transmittance and specific resistance of layers of carbon nanotubes (CNTs), silver nanowires (AgNWs) and coatings of (In₂O₃)_{0.9}-(SnO₂)_{0.1} (ITO) [6]

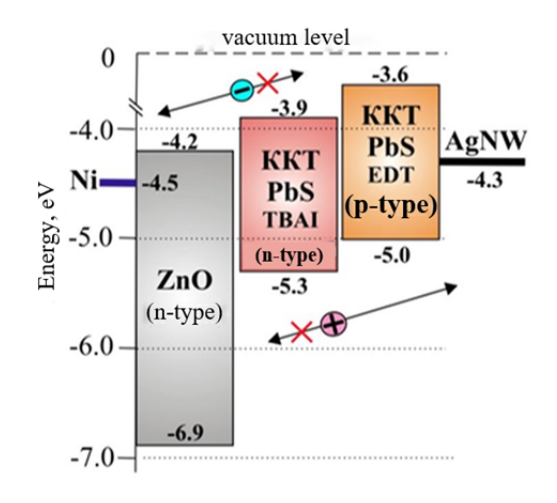


Fig. 2 Energy structure of layers of the Cr/Ni/n-ZnO/CQDn-PbS-TBAI/CQDp-PbS-EDT/AgNW structure, on the basis of which a single-element photosensor is manufactured [5]

The spectral dependence of the relative sensitivity of the sensor is shown in Figure 3a. The current-voltage characteristics (CVC) curves of the photosensors had a shape typical for semiconductor structures with an energy barrier and differential resistance of

the dark CVC at zero bias, lying within the range of $(2-20)\times10^{10}$ Ohm. The values of specific detectability of $(2-4)\times10^{12}$ cm·Hz^{1/2}·W⁻¹ (Fig. 3*b*) were achieved when the photosensor was illuminated by radiation from a blackbody with a temperature of 1273 K.

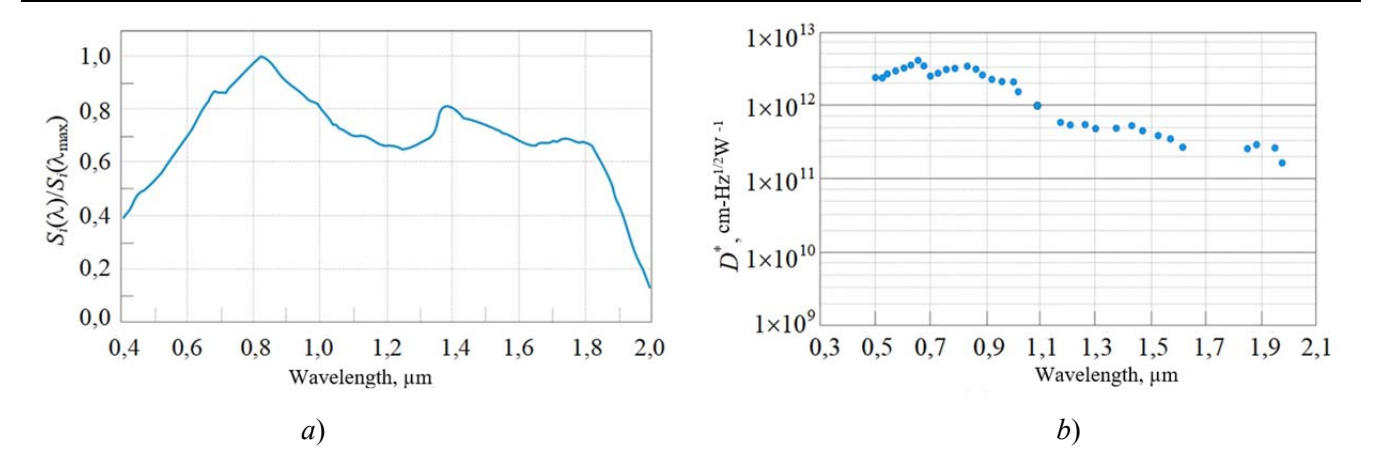


Fig. 3 Spectral dependences of the relative photosensitivity (a) [5] and specific detectability (b) of a single-element photosensor based on colloidal PbS quantum dots with the Cr/Ni/n-ZnO/CQD n-PbS-TBAI/CQD p-PbS-EDT/AgNW architecture

2. Architecture of the 640×512 photosensor array

In this paper, we describe a new FPA developed by us for the spectral range of $0.4\text{--}2.0\,\mu\text{m}$ in the 640×512 format with a photosensitive elements pitch of 15 μm , made of colloidal quantum dots PbS CQD on the surface of a silicon ROIC for reading p-channel photo signals. The architecture of this MPD is shown in Figure 4.

The production of this FPA is based on the direct formation of a photosensitive structure on the surface of a silicon readout integrated circuit (ROIC). The photosensitive and functional layers of the sensor are produced by successive applying pre-synthesized liquid suspensions of nanoparticles with a given composition and viscosity using the spin-coating technique or the aerosol printing method. This ensures the production of a monolithic structure without the use of indium or other microcontacts, which are typical for the classical technology of hybridization (combining) of photodiodes or photoresistors array based on layers of bulk or epitaxial 3D semiconductor materials with microelectronics for reading photo signals. technology This manufacturing for photosensors, called hybrid-monolithic, is described in general terms in [3, 5, 7–9]. It ensures the removal of critically important restrictions on the pitch of sensitive elements, as a result of which the pitch is limited only by the diffraction limit and the pitch of the ROIC, which is determined by the circuitry of the readout cell and the topological norm of the CMOS technology by which the silicon ROIC is manufactured.

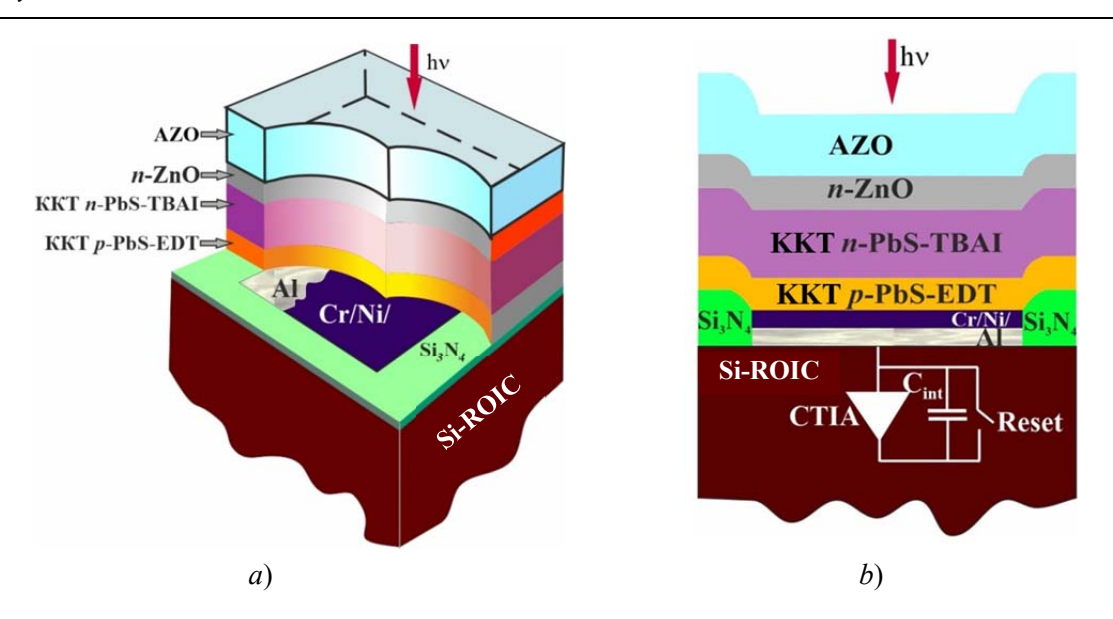


Fig. 4 640×512 photosensor array based on PbS CQD with transport layers for holes and electrons from p-PbS-EDT and n-ZnO CQD, respectively: a) – photosensor architecture; b) – cross-section of the photosensitive element with the input device of the silicon ROIC readout cell (CTIA – transimpedance amplifier, Reset – reset key, C_{int} – photo signal accumulation capacitance)

The architecture of each photosensitive element developed by the authors of the new PbS CQD based 640×512 photosensor array has the form Cr/Ni/p-PbS-EDT CQD/n-PbS-TBAI CQD/n-ZnO/AZO. The energy structure of individual layers demonstrating the directions of electron and hole transport in the layers of the photosensor is shown in Figure 5.

As in the case of the single-element photosensor [5] described above, the main proportion of photocarriers is generated by radiation in the *n*-PbS-TBAI COD layer. After the decay of photoexcitons, electrons and holes are separated by an energy barrier of the p-n junction type at the contact of the *n*-PbS-TBAI CQD and *p*-PbS-EDT CQD layers. The *n*-ZnO and *p*-PbS-EDT CQD layers serve to block holes and electrons in the regions located near the anode and cathode. They are also channels for transporting electrons and holes.

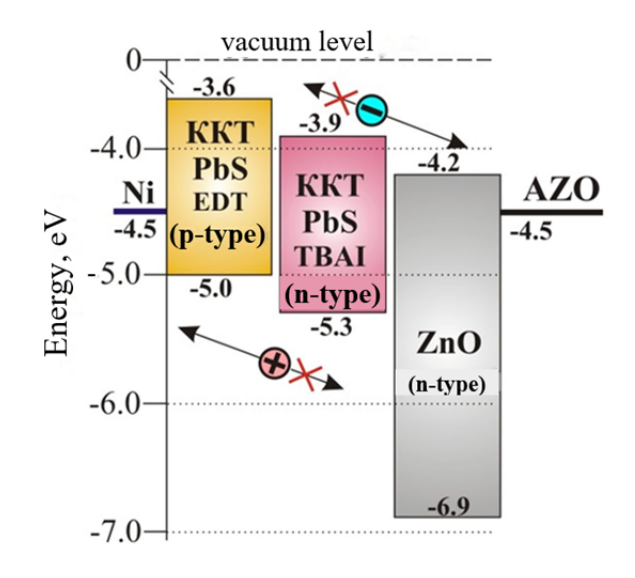


Fig. 5 Energy structure of layers of the Cr/Ni/p-PbS-EDT CQD/n-PbS-TBAI CQD/n-ZnO/AZO structure, on the basis of which the 640×512 photosensor array is made, demonstrating the directions of electron and hole transport

Manufacturing of PbS CQD layers of electronic and hole conductivity types is

carried out by replacing the initial ligand (oleic acid) after treatment with tetra-nbutylammonium iodide (n-type) and ethane-1,2-dithiol (p-type). As in work [5], lead chloride and N,N'-diphenylthiourea are used as precursors of lead and sulfur in the synthesis of PbS CQD. In addition, in contrast the above-described single-element photosensor with the Cr/Ni/n-ZnO/n-PbS-TBAI CQD/p-PbS-EDT CQD/AgNW architecture, here, instead of a layer based on AgNW nanowires, we used a coating of zinc oxide doped with aluminum to form a solid solution in $ZnO-Al_2O_3$ (AZO) system radiation-transparent electrode [10].A photograph of the manufactured 640×512 photosensitive element array based on PbS CQD with a silicon ROIC for reading and pre-processing photo signals and an upper electrode made of Al:ZnO (AZO), mounted on a raster for research, is shown in Figure 6.

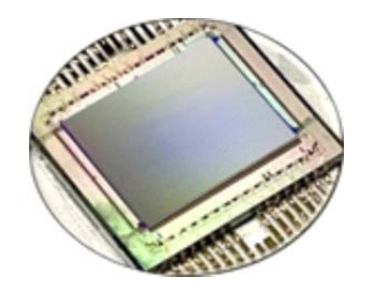


Fig. 6 Photograph of a 640×512 photosensitive element array with a ROIC on a raster

3. Properties of a 640×512 photosensor array with a hole transport layer based on *p*-PbS-EDT CQD

High-resolution transmission electron microscopy (TEM) was used to control the size of the synthesized colloidal quantum dots. The spectral dependences of the optical absorption of a suspension of colloidal quantum dots of lead sulfide in a solution of *n-octane*, synthesized by the above-described

method using PbCl₂ as a lead precursor, were studied. The first exciton absorption peak was observed with a maximum located at a $\lambda_{\text{max}} \approx 1,85 \, \mu\text{m}$ wavelength. Its full width at half maximum (FWHM) was 220 nm, which indicates a sufficiently high monodispersity of PbS nanocrystals in the absorbing layer of n-PbS-TBAI CQD. Figure 7 shows the spectral dependence of the photosensitivity $S_i(\lambda)/S_i(\lambda_{\text{max}})$ reduced to unity for the manufactured 640×512 matrix photosensor with a silicon integrated circuit for reading and pre-processing photo signals.

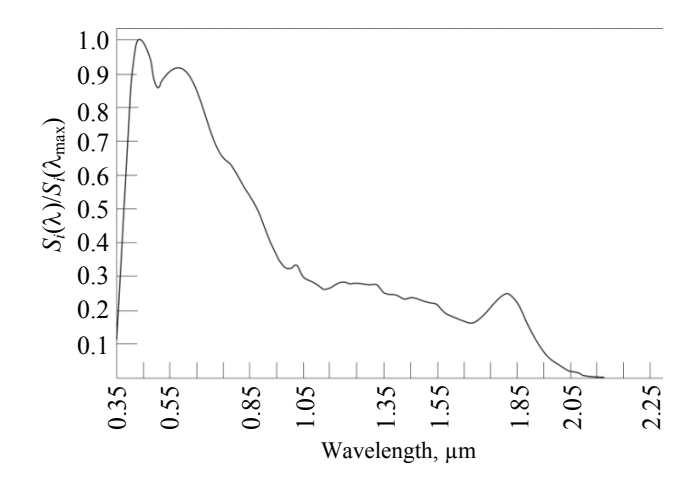


Fig. 7 Spectral dependence of photosensitivity at room temperature reduced to unity for a 640×512 photosensor array with a silicon ROIC for reading and pre-processing photo signals

The use of the empirical relationship $E_0 = 0.41 + (0.025d^2 + 0.283d)^{-1}$ that establishes the connection between the energy of optical transitions E0 in the optical absorption spectra of the CQD solution and the diameter d of the nanoparticles, obtained in [11], showed that the diameter of the colloidal quantum dots we used is $d \approx 9.5 - 10$ nm. A study of the shape of the nanoparticles using high-resolution transmission electron microscopy showed that it is close to a truncated octahedron. Each colloidal quantum dot has eight faces (111) and six faces (100).

Figure 8 shows fragments of images of fan blades and a human face obtained in the daytime at an illumination of the observed scene of 300-500 lux using a 640×512 photosensor array (15 µm pitch). Single-point correction and signal calibration using a defocused image were used.

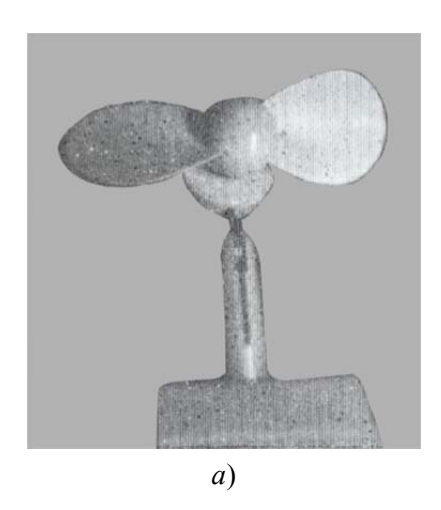




Fig. 8 Image fragments obtained using an uncooled 640×512 (15 µm pitch) photosensor array based on PbS colloidal quantum dots for the spectral range of 0.4–2.0 µm with the Cr/Ni/p-PbS-EDT QCD/n-PbS-TBAI QCD/n-ZnO/AZO architecture

4. Conclusion

One of the areas of improvement of night vision devices (NVD) is the expansion

oftheir spectral sensitivity areas. The sensitivity of modern mass-produced electro-optical converters (EOCs), including 3+ generation with photocathodes based on gallium arsenide with negative electron affinity, is limited to a spectral range of 0.4-0.9 µm. This results in a number of drawbacks of modern night vision devices, due to which the requirements for range, probability of detection and identification may not be met. The main one is the insufficient range of vision of the night vision devices at night illumination of the observed scene below 2×10^{-3} lux. This type of illumination is typical for objects located in mountain gorges, tunnels, on unlit city streets, under the forest canopy, etc. It is caused by diffuse or direct light from the moon, stars, zodiacal light, the proper radiation of the upper layers of the atmosphere associated with the recombination of ions formed during the day, etc. Figure 9a shows the spectral dependence of the power density of natural night illumination (NNI) on a vertical surface [12].

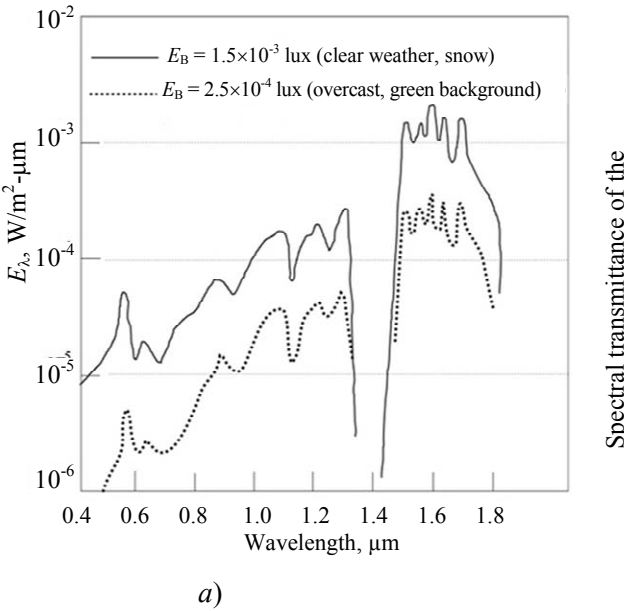
It is evident that the illumination level increases significantly in the wavelength range of $\Delta\lambda = 0.4-1.8$ µm compared to the range of $\Delta\lambda = 0.4-0.9 \,\mu \text{m}$ typical for modern mass produced EOCs. Thus, the average value of NNI in the absence of the moon in the wavelength range of 0.6-0.8 µm in clear weather (snow $(1.5-3.0)\times10^{-5} \text{ W/m}^2\cdot\mu\text{m}$ background) is while in the range of 1.4-1.8 µm, even with continuous cloud cover (green background), increases to $(6.0-7.0)\times10^{-4} \text{ W/m}^2\cdot\mu\text{m}$. The source of illumination here is the radiation of atmospheric oxygen. Along with the increase in illumination, a significant gain in optical transmission of the atmosphere occurs when moving from the spectral region of $0.4-0.9 \,\mu m$ to the region of $0.4-1.8 \,\mu m$ (Fig. 9b). The attenuation of the luminous flux by the atmosphere is associated with the

absorption of light by water vapor and carbon dioxide and scattering by fluctuations in the density of the gaseous medium of the atmosphere and by various solid dust particles. The assessment carried out in [13] showed that with a meteorological viewing range of $S_{\rm M}=10$ km, the transmittance of 1 km thick atmospheric layer at a wavelength of $\lambda=0.6$ µm is 0.72, and in the center of the transparency window of 1.4–1.8 µm it increases to a value of 0.93.

Photosensors array based on epitaxial In₀₅₃Ga₀₄₇As with an InP substrate, which technology has developed increasingly, easily implement a long-wave photosensitivity limit of $\lambda_{co} \cong 1.6$ µm. However, to ensure visible sensitivity in the range. production requires the use of special technological operations to thin the InP substrate after hybridization with the ROIC [14] for photo signal reading. The remaining InP layer, which is approximately 0.2 µm

thick, still limits the quantum efficiency of the photosensor in the visible range to ≤ 60 %. The need to use indium or copper microcontacts for hybridization of the photosensitive elements (PSE) array made of InGaAs with Si ROIC–limits the minimum step of the PSE to a value of about 5 μ m.

COD matrices adopt frontal illumination and no substrates that limit photosensitivity in the visible range of electromagnetic radiation. Also, no metal microcontacts are required for hybridization of the photosensitive elements array with the Si ROIC. The use of hybridmonolithic manufacturing methods [7] allows to create wide-spectrum matrices based on CQD with a 0.4–2.0 µm sensitivity range and a pitch of photosensitive elements limited only by the diffraction limit of the recorded radiation, the circuitry of the reading cell, and topological norm the of the **CMOS** technology, according to which the Si ROIC is manufactured.



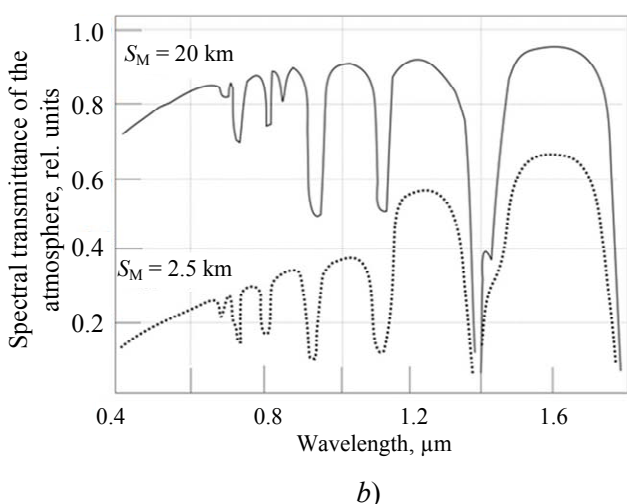


Fig. 9. a) – spectral dependence of the power density of natural night illumination on the vertical surface E_B under conditions of continuous cloudiness (green background), and for the case of clear weather against the background of a surface covered with snow; b) – spectral dependence of the transmission of an atmospheric layer 1 km thick for cases of meteorological vision range $S_M = 20$ km and $S_M = 2.5$ km [12]

This work was supported by the Advanced Research Foundation.

REFERENCES

- 1. You H. R., Park J. Y., Lee D. H., Kim Y. and Choi J., Appl. Sci. 10, 975 (2020). https://doi.org/ 10.3390/app10030975
- 2. Panja A. and Patra P., Inorganic Nanoparticle Luminphore: Design and Application 6 (4) (2023). https://doi.org/10.1051/fopen/2022020
- 3. Ponomarenko V. P., Popov V. S., Shuklov I. A., Ivanov V. V. and Razumov V. F., Russ. **93** (4), 5113 Chem. Rev. **RCR** (2024).https://doi.org/10.59761/RCR5113
- 4. Wang Y. and Sun H., Progress in Quantum Electronics **60**, 1 (2018).

https://doi.org/10.1016/j.pquantelec.2018.05.002

5. Popov V. S., Ponomarenko V. P., Dymkin D. V., Gadomska A. V., Shuklov I. A., Brichkin S. B., Lavrentiev N. A., Gak V. U., Mirofyanchenko A. E., Mirofyanchenko E. V., Katsaba A. V., Corresponding Arsenov P. V., Member of the RAS Ivanov V. V. and Corresponding Member of the RAS Razumov V. F., Doklady Physics **68** (7), 233–236 (2023).

https://doi.org/10.31857/S2686740023040120

6. Langley D., Mayousse C., Giusti G., Celle C., Bellet D. and Simonato J.-P., Nanotechnology 24 (45), 452001 (2013). https://doi.org/10.1088/0957-4484/24/45/452001

- 7. Popov V. S., Ponomarenko V. P. and Popov S. V., Journal of Communications Technology and Electronics 69 (4-6), 219-226 (2024). https://doi.org/ 10.51368/1996-0948-2023-6-45-53
- 8. Malinowski P. E., Georgitzikis E., Maes J., Vamvaka I., Frazzica F., Van Olmen J., De Moor P., Heremans P., Hens Z. and Cheyns D., Sensors 17, 2867 (2017). https://doi.org/10.3390/s17122867
- Gregory C., 9. Klem E. J. D., Lewis J., Cunningham G. and Temple D., Proc. of SPIE 8353, 835337 (2012).
- 10. Ajili M., Jebbari N., Turki N. K. Castagné M., International Renewable Congress (IREC2010, November 5–7, Tunisia), pp. 305-310.
- 11. Moreels I., Lambert K., Smeets D., Nollet T., Martins J. C., De Muynck D., Vanhaecke F., Vantomme A., Delerue C., Allan G. and Hens Z., ACS Nano 3 (10), 3023–3030 (2009). https://doi.org/ 10.1021/nn900863a
- 12. Gusarova N. I., Koshchavtsev N. F. and Popov S. V., J. Commun. Technol. 61 (10), 1211-1214 (2016).

https://doi.org/10.1134/S1064226916100144

- 13. Koshchavtsev N. F., Koshchavtsev A. N. and Fedotova S. F., Applied Physics, No. 3, 66-69 (1999) [in Russian].
- 14. Burlakov I. D., Grinchenko L. Y., Dirochka A. I. and Zaletaev N. B., Advances in Applied Physics 2 (2), 131–136 (2014) [in Russian].

Vladimir P. Ponomarenko^{1,2}, Chief Designer, Head of the Department, Doctor of Physical and Mathematical Sciences, Professor

Viktor S. Popov^{1,2}, Head of the Center, Head of the Laboratory, Associate Professor, Candidate of **Chemical Sciences**

E-mail: popov.vs@mipt.ru

Mikhail A. Pankov¹, Head of Laboratory, Candidate of Physical and Mathematical Sciences

Kamil A. Khamidullin¹, Group Leader, Head of the Department

Aleksandr D. Deomidov¹, Lead Engineer **Artem A. Fedorov**¹, Engineer of the 2nd Category German Yu. Deev¹, Engineer of the 2nd Category Denis E. Dragunov¹, Engineer of the 1st Category Oleg V. Epifanov¹, Lead Engineer Pavel S. Lazarev¹, Lead Engineer Ekaterina V. Mirofyanchenko¹, Group Leader,

Candidate of Technical Sciences

Denis V. Ilyinov¹, Engineer of the 1st Category Viktoriya A. Petrushina¹, Process Engineer **Igor D. Burlakov**¹, Deputy Director General for Innovations and Science, Doctor of Technical Sciences, Professor

Alexey V. Polessky¹, Chief Designer for Research and Development, andidate of Technical Sciences

Vadim V. Startsev¹, Director General, Candidate of Technical Sciences

Sergey B. Brichkin^{2,3}, Head of the Department, Chief Researcher, Candidate of Chemical Sciences

Maksim G. Spirin^{2,3}, Senior Staff Scientist, Senior Research Scientist, Candidate of Chemical Sciences **Sergey A. Tovstun**^{2,3}, Senior Staff Scientist,

Candidate of Physical and Mathematical Sciences, Associate Professor

Mikhail V. Gapanovich^{2,3}, Senior Staff Scientist, Candidate of Chemical Sciences

Vladimir Yu. Gak^{2,3}, Staff Scientist

Anna V. Gadomskaya^{2,3}, Staff Scientist, Candidate of Chemical Sciences

Dmitry N. Pevtsov^{2,3}, Process Engineer, Junior Staff Scientist

Alexey V. Katsaba², Senior Staff Scientist – Deputy Head of the Laboratory, Candidate of Physical and Mathematical Sciences

Alexey S. Kirichenko², Senior Staff Scientist, Candidate of Physical and Mathematical Sciences **Dmitry V. Dyomkin**², Junior Staff Scientist **Valeriya A. Ivanova**², Staff Scientist, Candidate of

Physical and Mathematical Sciences **Viktor V. Ivanov**², Director of the Institute of Quantum Technologies of Moscow Institute of Physics and Technology, Doctor of Physical and Mathematical Sciences, Corresponding Member of the Russian Academy of Sciences

Vladimir F. Razumov^{2,3}, Chief Staff Scientist – Head of the Laboratory, Doctor of Physical and Mathematical Sciences, Professor, Corresponding Member of the Russian Academy of Sciences ¹ RD&P Center ORION, join-stock company 9, Kosinskaya st., Moscow, 111538 Russia ² Moscow Institute of Physics and Technology 9, Institutskiy lane, Dolgoprudny, Moscow region, 141701 Russia

³ Federal Research Center of Problems of Chemical Physics and Medicinal Chemistry RAS 1, Academika Semenova Ave., Chernogolovka, Moscow region, 142432 Russia

Received January 9, 2025 Revised February 6, 2025 Accepted February 10, 2025 Scientific specialty code: 1.3.11

© V. P. Ponomarenko, V. S. Popov, M. A. Pankov, K. A. Khamidullin, A. D. Deomidov, A. A. Fedorov, G. Yu. Deev, D. E. Dragunov, O. V. Epifanov,

P. S. Lazarev, E. V. Mirofyanchenko, D. V. Ilyinov, V. A. Petrushina, I. D. Burlakov, A. V. Polessky.

V. V. Startsev, S. B. Brichkin, M. G. Spirin,

S. A. Tovstun, M. V. Gapanovich, V. Yu. Gak,

A. V. Gadomskaya, D. N. Pevtsov, A. V. Katsaba,

A. S. Kirichenko, D. V. Dyomkin, V. A. Ivanova,

V. V. Ivanov, V. F. Razumov, 2025

= PHOTOELECTRONICS =

UDC 538.975 PACS: 73.63.-b

Photomemristive switching in bismuth selenide crystals

A. V. Zotov, G. N. Panin, N. A. Tulina, D. N. Borisenko, N. N. Kolesnikov

An effect of optical switching of resistive states in structures based on chalcogenide Bi_2Se_3 compounds with copper and graphene electrodes was discovered. Authors proposed a physical model which describes the processes occurring during switching. The obtained results indicate the possibility of using the studied photomemristive structures as artificial synapses for neuromorphic computing, which weighting coefficients can be set both electrically and optically.

Keywords: chalcogenides; photomemristors; resistive switching; photomemristive states.

DOI: 10.51368/1996-0948-2025-1-55-59

Introduction

The high energy efficiency of biological "computing and detection systems" compared to the enormous energy consumption of modern computing and detection devices developed by humans to detect and analyze big data related to visual information stimulates great interest to research of operational principles of neuromorphic systems. Today, detection and processing of visual information is carried out using the Von Neumann architecture, where sensory, memory, and computing units are divided.

This requires converting the optical signal into an electrical one, transmitting it to the computer, to the memory and back. Machine learning algorithms in such systems are implemented at the software level, which undoubtedly results in the poor quality of the issue solution and increases energy costs and the time for processing visual data. The development and implementation of "analog" artificial synapses and neurons is a critical task to improve energy efficiency and accelerate processing speed of electrical [1–3] and optical signals [4–6].

Aleksandr V. Zotov¹, Junior Staff Scientist E-mail: taba@iptm.ru

Gennady N. Panin¹, Senior Staff Scientist, Candidate of Physical and Mathematical Sciences

Natalya A. Tulina², Senior Staff Scientist, Candidate of Physical and Mathematical Sciences

Dmitry N. Borisenko², Senior Staff Scientist, Candidate of Physical and Mathematical Sciences **Nikolay N. Kolesnikov**², Doctor of Technical Sciences

¹ Institute for Problems of Microelectronics Technology and High-Purity Materials of the Russian Academy of Sciences 6, Osipyana st., Chernogolovka, Moscow region, 142432 Russia

² Osipyan Institute of Solid-State Physics of the Russian Academy of Sciences

2, Academician Osipyana st., Chernogolovka, Moscow region, 142432 Russia

Received August 2, 2024 Revised November 20, 2024 Accepted February 1, 2025 Scientific specialty code: 1.3.11

© A. V. Zotov, G. N. Panin, N. A. Tulina, D. N. Borisenko, N. N. Kolesnikov, 2025

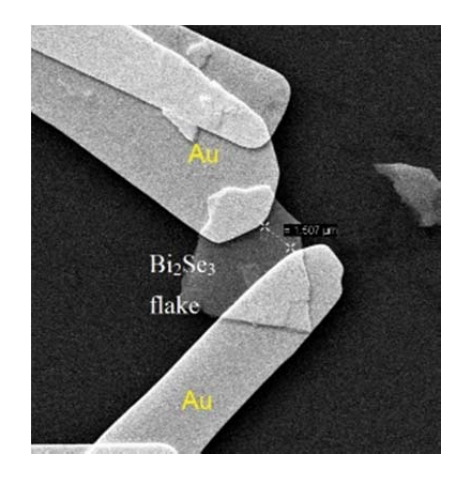
Chalcogenide memristors, control of resistive states by electric field

Layered chalcogenide materials such as bismuth selenide Bi_2Se_3 consist of two layers of Bi and three layers of Se (so-called quintuples, which are about 1 nm thick). These layers are linked together by Van der Waals bonds. This allows bulk crystals to be split along these layers, allowing to obtain very high-quality microscopic structures with quite simple methods. The possibility of memristive switching in bismuth selenide crystals ($E_g = 0.3-0.8 \text{ eV}$) was previously demonstrated [7, 8].

From Bi_2Se_3 crystals obtained by the Bridgman method, cleavages were prepared along the quintupule layers, with characteristic dimensions of 3–4 mm along the layers and 200–300 μ m across, which were then transferred to a copper substrate served as the lower electrode. The transferred crystals were pressed mechanically onto the substrate using a beryllium bronze rod, which

served as the top electrode. Samples were also made from layered Bi₂Se₃ crystals obtained by exfoliating a bulk crystal with adhesive tape and transferred to a Si/SiO₂ substrate, followed by the production of gold electrodes for them using electron beam lithography (Fig. 1, left). The obtained structures were studied for their currentvoltage characteristics (CVC) and the time parameters of electrical and optical switching using a Keithley 2450 source meter, a GW Instek AFG 73021 arbitrary waveform generator, a LeCroy WaveSurfer 24Xs-A oscilloscope, and laser excitation wavelength of 650 nm.

The structure produced with Au-Bi₂Se₃-Au gold electrodes exhibited a linear CVC without resistive switching features (Fig. 1, right). The absence of resistive switching and an ohmic CVC were also observed in the structure with silver electrodes made to the edges of the crystal using RS PRO Silver Conductive silver glue.



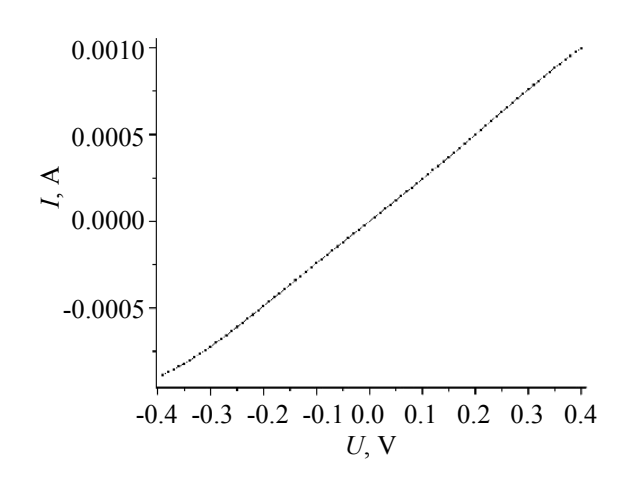


Fig. 1. Layered Bi₂Se₃ crystals transferred onto a Si/SiO₂ substrate (by exfoliating the bulk crystal with adhesive tape) with gold electrodes produced with electron beam lithography (left) and the CVC of the Au/Bi₂Se₃/Au structure (right)

The vertical structure with copper electrodes $Cu\text{-Bi}_2Se_3\text{-Be}Cu$ showed a change in resistance in a range of values from $R_{\text{high}} = 100 \text{ Ohm}$ to $R_{\text{low}} = 5 \text{ Ohm}$. The reproducibility of the resistance value

was about 10 %, which made it possible to obtain 9 memristive states (Fig. 2) of the sample when it was treated by electrical pulses. Thus, it was shown that memristive states in a vertical structure can be achieved

with an "active" copper electrode. Based on these experimental data, X-ray diffraction analysis and analysis of previously published data, it was concluded that the observed resistive switching is caused by the migration of active metal compounds, percolation of these compounds into Van der Waals gaps [9] and transport of point structural defects (such as selenium vacancies) the surface modified layer [10].The application of an electric field of one polarity results in formation of a conductive channel, which is maintained when the external electric field is switched off, and is destroyed when treated with an electric field of reverse polarity.

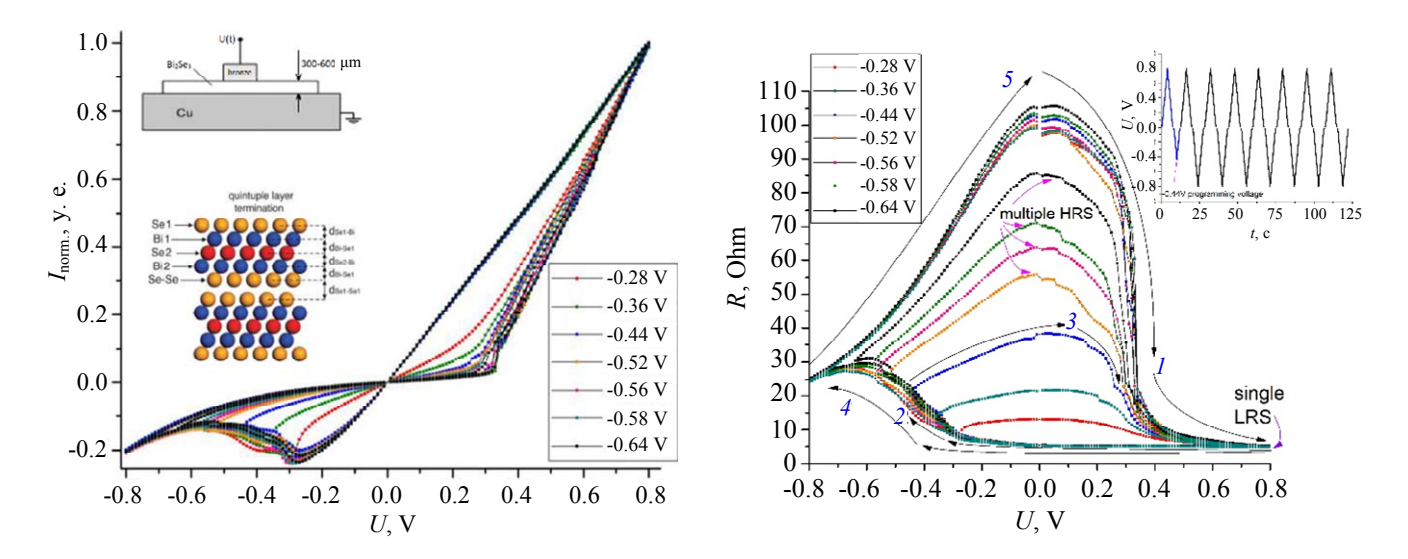


Fig. 2. Control of resistive states of the Cu-Bi₂Se₃-BeCu structure by an electric field. structure CVC (left).

Inserts: Layout view of the sample (top left) and the structure of Bi₂Se₃ (bottom left).

Dependence of the resistance of the Cu-Bi₂Se₃-BeCu structure on the bias voltage (right).

Insert: Time sweeping of offset voltage

Optical response

The optical response of the Cu-Bi₂Se₃-BeCu structure was also investigated (Fig. 3). The sample treated by optical radiation (650 nm laser), turned into a low-resistance state at different bias voltages. When the

optical pulse was turned off, the structure "electrically" returned to the resistance value caused by the electric field. Transitions to intermediate optical states, as we assume, are possible when the radiation parameters (wavelength, pulse duration) vary.

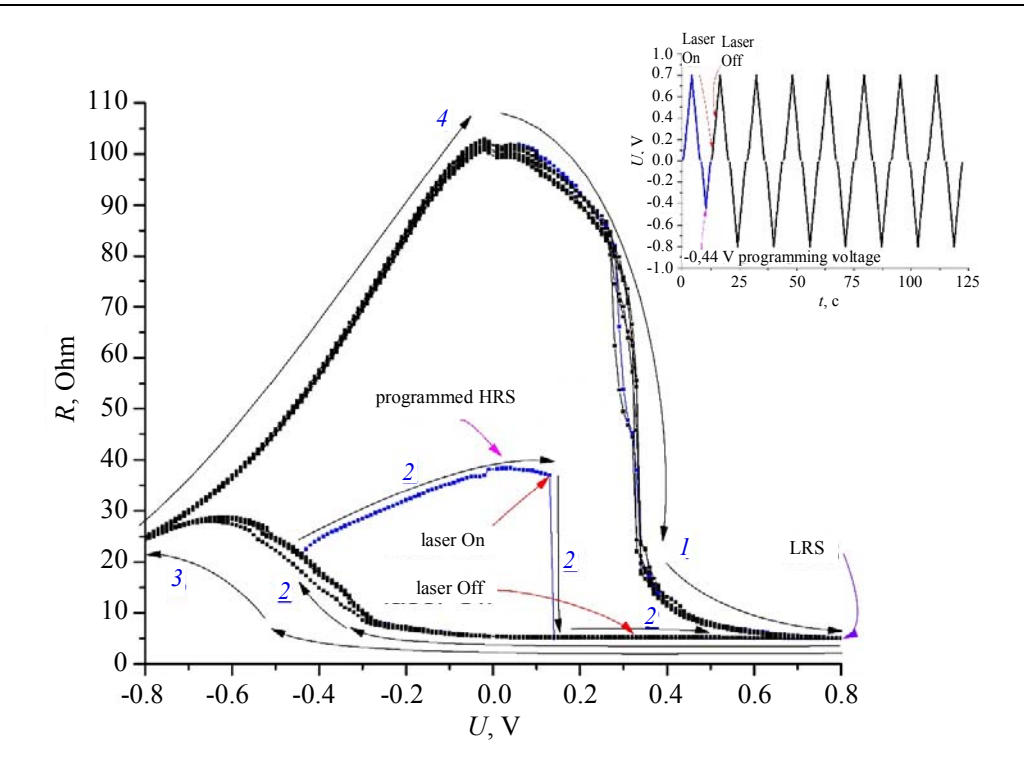


Fig. 3. Control of resistive states of the Cu-Bi₂Se₃-BeCu structure electrically and optically. Inset: time sweeping of bias voltage of the structure with programming and optical excitation by 650 nm laser

Active electrode made of oxidized graphene

The studied vertical Bi₂Se₃ structures demonstrated photomemristive properties in the presence of an active electrode, when the current flows across the quintupole layers and the modified layer formed on the Bi₂Se₃ surface. For optical applications [11], vertical structures with a transparent active electrode are of particular interest. In this work, such electrode was made of oxidized graphene (OG), which can serve as a source of oxygen modifying the surface layer of the structure when exposed to an electric field or optical radiation [6].

Figure 4 shows the dependence of the resistance of the produced Au/Bi₂Se₃/OG structure on the bias voltage under electrical and optical excitation. The top electrode to the structure was made from OG transferred onto a plastic substrate (Fig. 4, insert). The structure with the OG clamping electrode exhibited resistive properties similar to those

of the Cu-Bi₂Se₃-BeCu structure, but less stable, which may be due to the defective structure of the thin OG clamping layer. This did not allow HRS programming to be performed. From cycle to cycle, the HRS instabilityexceeded 20 % (LRS 1 ~150 kOhm was more stable). This parameter can be improved by enhancing the contact between graphene and Bi₂Se₃ by direct transfer of the graphene electrode to the crystal surface, which requires refining the transfer technique to low-dimensional structures.

Upon optical excitation. the Au/Bi₂Se₃/OG structure switched to a low-resistance state LRS 2 (~100 kOhm), lower than LRS 1, to which the structure was switched from HRS by an electric field. Still the LRS 2 state did not turn to HRS in this range of bias voltages, indicating that it may depend on duration, intensity, and wavelength of the laser pulses The obtained results were reproduced on several fabricated structures, all of them, having similar CVC and R(U), switched reversibly by an electric field from HRS to LRS 1 and irreversibly by optical excitation from HRS to LRS 2. This indicates a more complex mechanism of resistive switching in such heterostructures during their optical

excitation under changing electric field. A system of coordinated control of the duration and intensity of optical and electrical pulses will allow such experiments to be carried out in more details.

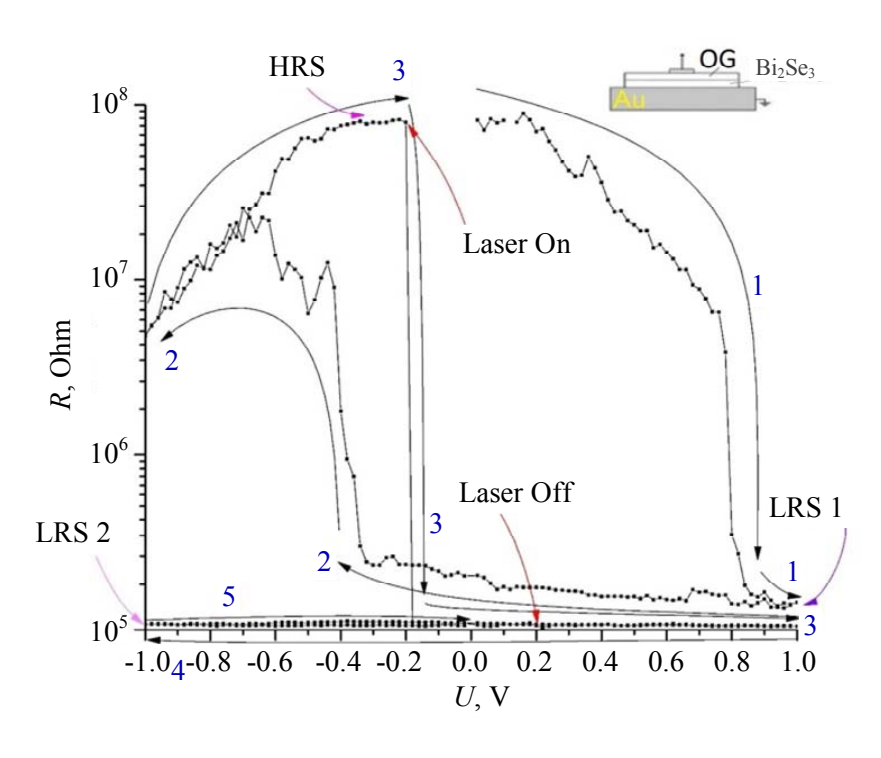


Fig. 4. Control of resistive states of the Au/Bi₂Se₃/OG structure electrically and optically. Insert: schematic representation of the sample under study

Conclusion

Authores produced and studied two types of structures, Cu/Bi₂Se₃/BeCu and Au/Bi₂Se₃/OG, showing resistance plasticity under electrical and optical excitation. The obtained results indicate the potential of memristive structures based on layered Bi₂Se₃ chalcogenides for the implementation of artificial synapses for neuromorphic computing and optical signal processing in photosensors.

The work was carried out with the financial support of the Russian Science Foundation, project No. 23-49-00159. Work on the installations of Institute for Problems of Microelectronics Technology and High-Purity Materials of the Russian Academy of Sciences was carried out

and supported within the framework of state assignment No. 075-00296-24-00.

REFERENCES

- 1. Chua L. O., Nat Electron 1, 322 (2018).
- 2. Kapitanova O. O., Emelin E. V., Dorofeev S. G., Evdokimov P. V., Panin G. N., Lee Y. and Lee S., J. Mat. Sci. Tech. **38**, 237 (2020).
 - 3. Panin G. N., Electronics 11, 619 (2022).
 - 4. Wang W. et al., Sci. Rep. 6, 31224 (2016).
 - 5. Fu X. et al., Small **15** (45), 1903809 (2019).
 - 6. Fu X. et al., Light Sci. Appl. 12, 39 (2023).
- 7. Zotov A. V. et al., Chaos, Solitons & Fractals **141**, 110542 (2021).
- 8. Sirotkin V. V., Russian Microelectronics **52**, 363 (2023).
- 9. Mao Ye et al., The Journal of Physical Chemistry C **125** (3), 1784–1792 (2021).
- 10. Mihailovic I. A. et al., Journal of Micromechanics and Microengineering **31** (9), (2021).
- 11. Yin J. et al., Nature Communications 9, 3311 (2018).

= PHOTOELECTRONICS =

UDC 621.383.4/5: 621.315.59 PACS: 07.07 Df, 07.57.-c, 81.05.Ea, EDN: IJAWEC 81.65.Rv

Characteristics of small-format matrix photodetectors

A. A. Lopukhin, E. V. Permikina, K. V. Barysheva, A. N. Grishina

Small-format matrix photodetectors of the $3\div 5~\mu m$ spectral range based on matrices of indium antimonide photodiodes with minimal defects and uniform sensitivity are investigated. It is shown that the selection of plates from InSb ingots for the production of photosensitive element matrix in accordance with the analysis of statistical data and the use of group thinning and washing allowed to obtain 22 % defect-free of the total number of matrix photodetectors (MPDs) with a defect-free central region. It has been established that treatment of the viewing side of the photodiode matrix with argon ions significantly improves the homogeneity of the sensitivity distribution over the MPD area.

Keywords: matrix photodetectors (MPD); medium-wave spectral range; indium antimonide; defects; homogeneity of sensitivity; group thinning; ion etching; recombination.

DOI: 10.51368/1996-0948-2025-1-60-63

Introduction

Photodetectors (PDs) based on photodiode matrices made of indium antimonide (InSb) are widely used in modern thermal imaging and heat source direction finding systems for the mid-infrared spectral

Alexey A. Lopukhin, Head of the Site, Candidate of

Technical Sciences

E-mail: alexmatr0@mail.ru

Elena V. Permikina, Lead Engineer

Ksenia V. Barysheva, Engineer of the 1st Category **Anna N. Grishina**, Engineer of the 1st Category RD&P Center ORION, join-stock company 9, Kosinskaya st., Moscow, 111538 Russia

Received December 12, 2024 Revised January 10, 2025 Accepted February 1, 2025 Scientific specialty code: 1.3.11

© A. A. Lopukhin, E. V. Permikina, K. V. Barysheva, A. N. Grishina, 2025

range [1]. Currently, small-format matrix PDs in demand for recognizing most high-speed objects. The small photoelectric coupling of photosensitive elements (PEs) of small-format matrices allows thermal images with clear outlines, reducing the blurring of object boundaries. On thinned MPEs (matrix photosensitive elements), the short-range coupling in the region of element does not exceed 5 % [2]. Good homogeneity of sensitivity over the area of the photodiode matrix and minimization of the number of photoelectric defects to zero allow for the recognition of objects with maximum accuracy [3, 6].

The structure of small-format MPDs (matrix photodetectors) based on InSb is a 64×64 matrix of photosensitive elements, hybridized with a LSI readout on a raster and a filter. To improve the quantum yield, an antireflective coating is applied to the illuminated side of the MPE. The thickness of the PE matrix of $10\div20~\mu m$ is determined by

the balance between achieving the optimal quantum yield and the relationship caused by the lateral diffusion of minor charge carriers [4].

Defectiveness of the MPEs

Statistical processing and analysis of data on the defectiveness of the MPEs obtained from indium antimonide ingot plates showed that plates taken from the middle of the ingots are most suitable for the production of photodiode matrices with optimal characteristics. The selection of plates for the production of MPEs in accordance with the analysis of statistical data allowed us to increase the percentage of defect-free MPDs.

Figure 1 shows the integral distribution of defects of matrix photodetectors. Defect-free photodetectors accounted for 22 % of the total number of MPDs, and those with one photoelectric defect accounted for 48 % (with a defect-free central region) for group thinning. Evidently, the defectiveness

of most MPDs does not exceed 10 elements. On average, there were ≈ 2 defects (368 MPDs measured).

Improving the homogeneity of the sensitivity distribution (current or volt) over the area of the matrix of photosensitive elements is determined by the homogeneity of the MPEs by thickness, since the number of absorbed photons and generated charge carriers is located in the volume of the semiconductor matrix and depends on its thickness. The most optimal method to obtain PE matrices with homogeneous thickness and implement mass production of photodetectors is to use group MPD thinning and washing Group chemical-dynamic [5]. polishing during thinning of photodiode matrices from the side of illumination allowed to reduce edge effects associated with over-thinning of matrices along the perimeter of the MPE, and therefore to reduce the areas of hypo sensitivity at the edges of the matrices. MPDs based on such matrices allowed to obtain more homogeneous images to improve the recognition of objects.

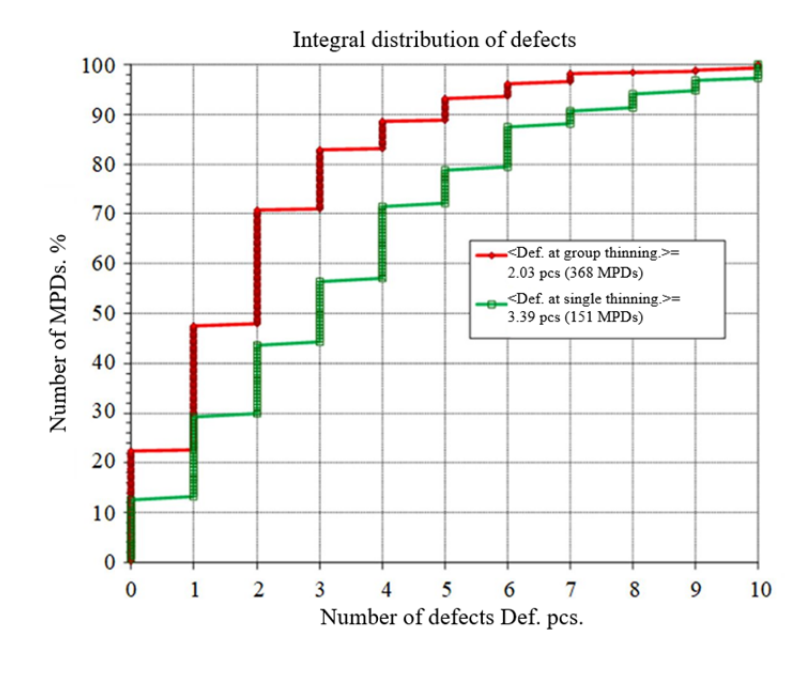


Fig. 1. Integral distributions of defects of matrix photodetectors

Homogeneity of sensitivity

Figure 2 shows the integral distributions of the spread in sensitivity of matrix photodetectors manufactured using single and group thinning of the PE matrices.

On average, the spread of sensitivity for group processing methods decreased to 3.7 % (4.2 % for single thinning).

Another factor impacting the improvement of sensitivity homogeneity is

the maximum reduction of regions with an increased recombination rate of photogenerated current carriers, determined by the high density of additional energy levels in the restricted zone. When optical radiation falls from the side of the clarified surface of the MPE, some of the photocarriers can gather along the diffusion length at the interface between the PE matrix and the clarifying coating and recombine due to the high density of electron states.

Recombination of charge carriers which occurs due to non-uniform thickness and composition of oxide films on the surface of the PE matrices and other defects formed during technological processing, suggests the appearance of additional states in the restricted zone, resulting in an increase in the recombination rate in localized areas of the matrix, which contributes to an increase of sensitivity range.

The use of ion treatment of the surface of the MPE with a low-energy flow of positively charged argon ions (high-frequency cathode sputtering with argon ions with an energy of less than 0.25 keV removes a damaged layer up to 0.5 µm) allows to remove mechanically damaged, and partially or completely (depending on the number of ion treatments) damaged layer of the material. changing the magnitude of the surface charge, preventing the flow of mobile charge carriers the near-surface region and their subsequent recombination [6, 7]. Treatment with argon ions before clarification forms a positive built-in charge on the surface of the back side of the matrix, providing a significant bending of the semiconductor's restricted zone, but not exceeding the width of the restricted zone, which forms a repulsive field for minor charge carriers. That is why the amorphous surface layer formed during the process of exposure to a low-energy flow of positively charged ions, which is less than 50 Å thick [8] and has a high value of surface recombination, does not impact significantly on the effective recombination rate and does not create additional dark currents of the photodiodes.

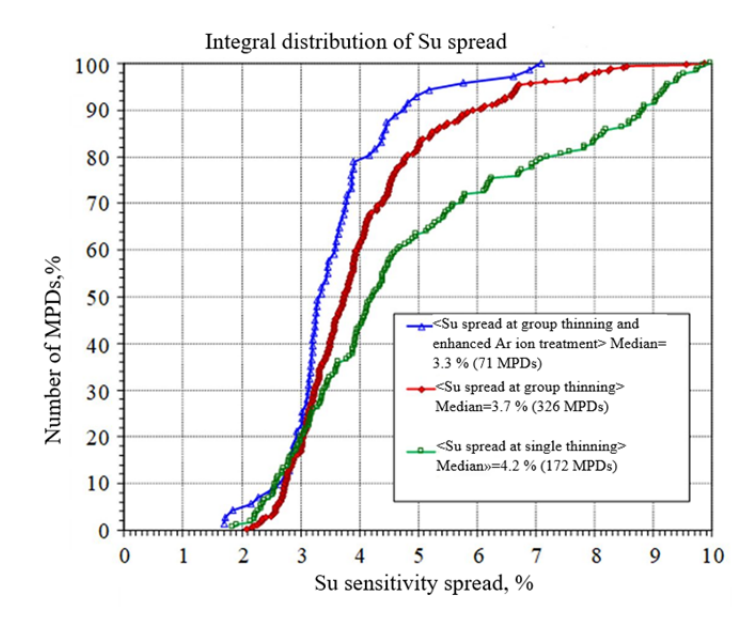


Fig. 2. Integral distributions of the spread of sensitivity of matrix photodetectors

The homogeneity of sensitivity over the area of the MPD was improved during group thinning due to enhanced ion treatment of the back surface [6, 7] (see Fig. 2). Ion treatment removed a significant portion of the damaged

surface material and initiated a large positive built-in charge at the interface on the incident radiation side. The increase of surface potential formed a repulsive field for minor charge carriers and inhibited the recombination of photocarriers on the surface, due to which the sensitivity range (current or volt) over the area of the MPE decreased several times.

Conclusion

- 1. It is shown that the selection of plates from InSb ingots for the production of small-format MPE in accordance with the analysis of statistical data and the use of group thinning and washing made it possible to obtain 22 % defect-free of the total number of matrix photodetectors with a defect-free central region.
- 2. It has been established that treatment of the viewing side of the photodiode matrix with argon ions significantly improves the homogeneity of the sensitivity distribution over the MPD area.

REFERENCES

1. Boltar K. O., Burlakov I. D., Iakovleva N. I., Vlasov P. V. and Lazarev P. S., Usp. Prikl. Fiz. (Advances in Applied Physics) **10** (2), 170–182 (2022) [in Russian].

- 2. Boltar K. O., Vlasov P. V., Lazarev P. S., Lopukhin A. A. and Chishko V. F., Applied Physics, No. 1, 18–24 (2020) [in Russian].
- 3. Lopukhin A. A., Boltar K. O., Grishina A. N. and Shishigin S. E., Usp. Prikl. Fiz. (Advances in Applied Physics) **10** (1), 14–22 (2022) [in Russian].
- 4. Lopukhin A. A., Boltar K. O., Vlasov P. V., Eroshenko V. V., Chishko V. F., Koshchavtsev N. F. and Larionov N. A., Usp. Prikl. Fiz. (Advances in Applied Physics) **8** (5), 334–340 (2020) [in Russian].
- 5. Lopukhin A. A., Eroshenkov V. V., Irodov N. A., Savostin A. V., Barysheva K. V., Vlasov P. V., Permikina E. V. and Grishina A. N. Method of group fabrication of a thinned hybridized assembly for a matrix photodetector. Patent No. 2811380 (RF). 2023.
- 6. Lopukhin A. A., Permikina E. V., Boltar K. O. and Grishina A. N., Usp. Prikl. Fiz. (Advances in Applied Physics) **11** (5), 421–431 (2023) [in Russian].
- 7. Vlasov P. V., Grishina A. N., Lopukhin A. A., Permikina E. V. and Shishigin S. E. A method for manufacturing a thinned multi-element photodetector based on indium antimonide with improved uniformity and increased mechanical strength. Patent No. 2811379 (RF). 2023.
- 8. Chulkyun Seok, Minkyung Choi, Sehun Park, Jinwook Jung, Yongjo Park, In-Sang Yang and Euijoon Yoona, ECS Solid State Letters **3** (3), P27–P29 (2014).

= PHOTOELECTRONICS =

PACS: 85.60.-g UDC 621. **EDN: IXOEGF**

Synthesis of colloidal quantum dots of lead sulfide in decene-1 as a solvent

I. A. Shuklov, D. V. Dyomkin, O. V. Vershinina

A new approach to the synthesis of lead sulfide colloidal quantum dots is proposed, in which decene-1 is used for the first time as a solvent for the synthesis of nanocrystals. PbS CQDs with a long-wavelength exciton absorption peak in the range from 1.17 to 1.53 µm were obtained. The influence of temperature and reaction time on the spectral characteristics of the obtained PbS quantum dots was studied.

Keywords: lead sulfide; high-temperature colloidal synthesis; precursor; quantum dots.

DOI: 10.51368/1996-0948-2025-1-64-69

Introduction

Colloidal quantum dots have been the subject of intensive research over the past decades to create cheap and readily available solar cells, photodetectors, lasers, and LEDs. The ability to easily tune the spectral range and the availability of applying solutions of these nanomaterials make them particularly interesting for applications in electronics, in particular for the creation of photodetectors [1]. The combination of a large Bohr exciton radius in the bulk material (18 nm) and a band

Ivan A. Shuklov. Senior Staff Scientist. Associate Professor, Dr. rer. nat.

E-mail: shuklov.ia@mipt.ru

Dmitry V. Dyomkin, Junior Staff Scientist, Graduate Student

Olesya V. Vershinina, Junior Staff Scientist, **Graduate Student** Moscow Institute of Physics and Technology 9, Institutsky lane, Dolgoprudny, Moscow region,

Received October 2, 2024

141701 Russia

Revised January 24, 2025 Accepted January 29, 2025 Scientific specialty code: 1.3.11 gap of 0.41 eV makes PbS CQDs particularly attractive [2]. This allows changing the position of the maximum of the exciton absorption peak in the range from 800 nm to 2100 nm with a change in the average size of nanoparticles from 2 to 10 nm. changing the range of spectral sensitivity in photodetectors based on them.

industrial first samples megapixel format matrix photodetectors were created in recent years using PbS CQDs [3]. The simplicity of the technology provides new possibilities for reducing the cost of matrix photodetectors and expanding their possible applications.

The synthesis of colloidal nanocrystals currently uses a standard set of high-boiling solvents and reagents that have proven themselves well in terms of efficiency and reproducibility, as well as low cost. One such reagent is octadecene-1. This long-chain alkene is often used in the syntheses of colloidal quantum dots such as PbS, CdSe, and InP as a high-boiling non-coordinating solvent [4–6]. Less frequently, octadecene-1 is used as a reagent for the preparation chalcogen precursors: sulfur [7] or selenium [8]. In modern conditions, there is a

need to find an affordable Russian analogue of this reagent. An important factor for use in the synthesis of nanocrystals is also the possibility of using such substances not only after maximum purification, but also in a commercially available form. It is known that the purity of reagents can greatly influence the results of nanocrystal synthesis. E.g., impurities in trioctylphosphine critically affect the nucleation of CdSe [9]. Impurities in oleylamine have a major impact on the solubility of lead halides and, as a result, on the quality of PbS nanocrystals obtained in this solvent [10].

One of the possible candidates for replacing octadecene-1 is decene-1. This substance is available in the "pure" grade from a number of Russian manufacturers. Compared to octadecene-1, it has a lower boiling point of 171 °C, which allows it to be used in the synthesis of lead chalcogenides.

In the context of studies on the production and study of the properties of PbS CQDs, carried out in our laboratory, we were attracted by the possibility of finding an alternative to octadecene-1 [11–14]. In this work, the production of colloidal quantum dots of lead sulfide was investigated using decene-1 as a solvent for the lead precursor and, accordingly, in the synthesis of lead sulfide CQDs. For the use of this reagent in the synthesis of nanocrystals, it is important both to be able to use it with the highest degree of purity and to use it in a commercially available form.

Experimental section

Reagents

The following chemicals were used in the synthesis of PbS CQDs without further purification: lead oxide (99.99 %, Lanhit), sulfur (special purity grade, Reakhim), oleic acid (90 %, Vekton), 1-octadec (90 %, Aldrich), decene-1 ("Ch", Vekton), n-hexane (99 % HPLC grade, Macron Fine Chemicals), ethanol (reagen tgrade, Khimmed), and oleylamine (80–90 %, Acros), which was pre-dried under reduced pressure and at 90 °C.

Measurement methods

The following methods and measurement tools were used to study the properties of nanoparticles: TEM (JEM-2100, JEOL), spectrophotometer (JASCO V-770, JACSO), gas chromatograph (Chromatec 5000.2, VR-1 column, 60 m), IR Fourier spectrometer (Spectrum 100, PerkinElmer) with a HATR Accessory (ATR), equipped with a Ge prism (angle of incidence 45°, number of reflections 25).

Discussion of the results

Decene-1, like octadecene-1, is alkene with a terminal double bond. In industry, it is obtained by oligomerization of ethylene or cracking of high-boiling fractions of oil followed by distillation [15]. Decene-1 is an important starting material in the production of poly-alpha-olefins used in the automotive and aviation industries as lubricating oils. which determines its availability and low cost [16]. Impurities in decene-1 depend on the method of its production. Thev can be saturated hydrocarbons. and unsaturated Gas chromatography showed the content of the main substance, decene-1, to be about 98 %. The commercial decene-1 used also contains at least two impurities, each with a content of about 1 mol% (Fig. 1a). ¹NMR spectroscopy also showed the presence of aldehydes and derivatives aromatic ofbenzene in commercial decene-1 at concentrations of the order of tenths of a percent (Fig. 1a).

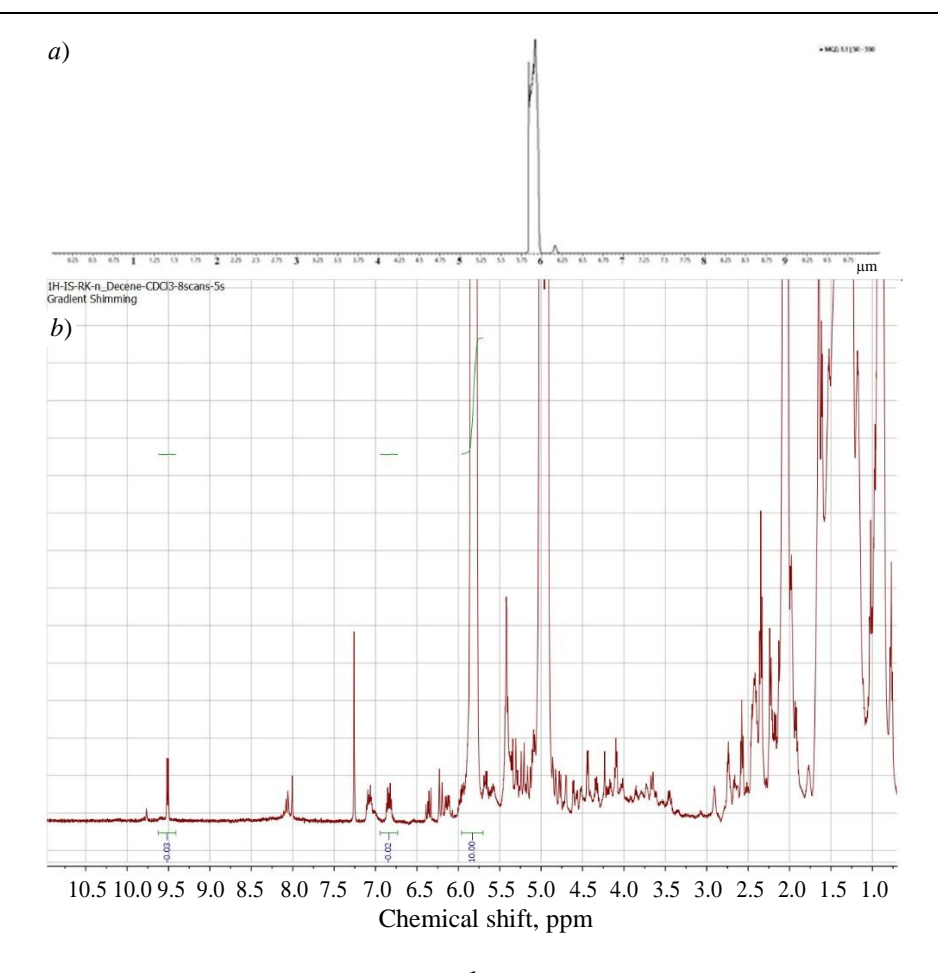


Fig. 1. a) – GC-Chromatogram and b) enlarged ¹NMR spectrum of decene-1 used in the synthesis

The authors established that synthesis of lead sulfide CQDs is possible in commercial decene-1 produced in Russia using a method similar to that previously published by us [13]. It was found that replacing octadecene-1 with decene-1 does not result in a change in particle size when using the same reaction conditions, i.e., temperature, synthesis time concentrations of the remaining reagents. When synthesizing at 120 °C, samples were obtained with practically identical positions of the exciton peak at 1530 nm with FWHM 171 nm in decene-1 and 1525 nm with **FWHM** 170 in octadecene-1 (Fig. 2). distribution The of nanoparticle according to spectroscopic data also did not change: FWHM 171 in decene-1 and FWHM 170 in octadecene-1. Moreover, even without additional purification, decene-1 does not inhibit the nucleation and growth of lead sulfide nanocrystals.

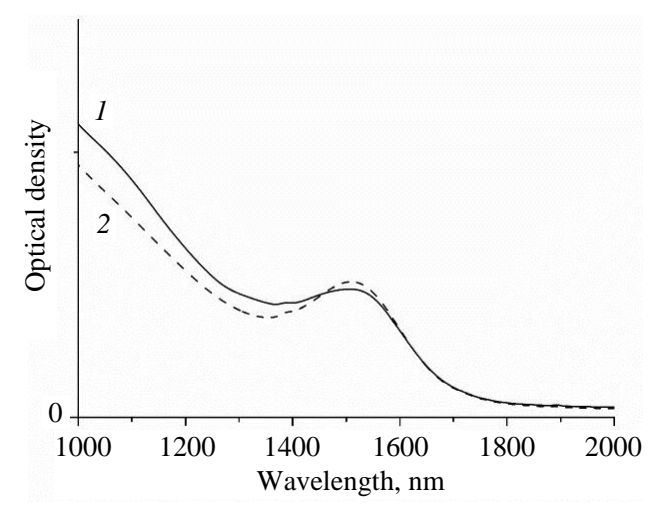


Fig. 2. Absorption spectra of PbS CQD samples obtained in decene-1 (1) and octadecene-1 (2) at 120 °C

By varying the synthesis temperature from 80 °C to 120 °C, it is possible to obtain particles with the position of the exciton absorption peak maximum from 1170 nm at 80 °C to 1530 nm at 120 °C (Fig. 3). The spectrum of nanoparticles obtained

at 100 and 120 °C shows a pronounced exciton peak with FWHM of 173 and 171 nm. In the sample obtained at 80 °C, the exciton peak is weakly expressed.

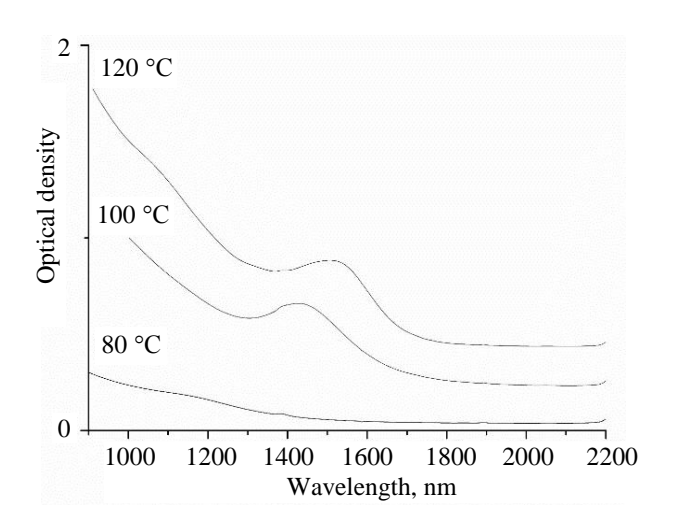
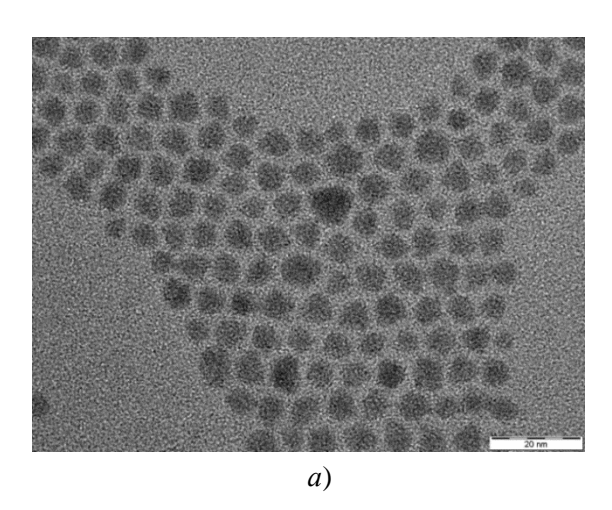


Fig. 3. Absorption spectra of PbS CQD samples obtained in decene-1 at different temperatures: $1-80 \, \text{ C}; \, 2-100 \, \text{ C}; \, 3-120 \, \text{ C}$

For the reaction carried out at 100°, the kinetics was investigated (Fig. 4). As for the similar system based on lead oxide in oleic acid in octadecene, the greatest growth is observed in the first two minutes of synthesis and the first sample has the first exciton absorption peak at 1350 nm. Samples at 8 and 15 minutes showed a slight increase to 1440 and 1480 nm, respectively. The observed exciton absorption peak of the 15 min sample is more pronounced compared to earlier samples with FWHM 180 nm.



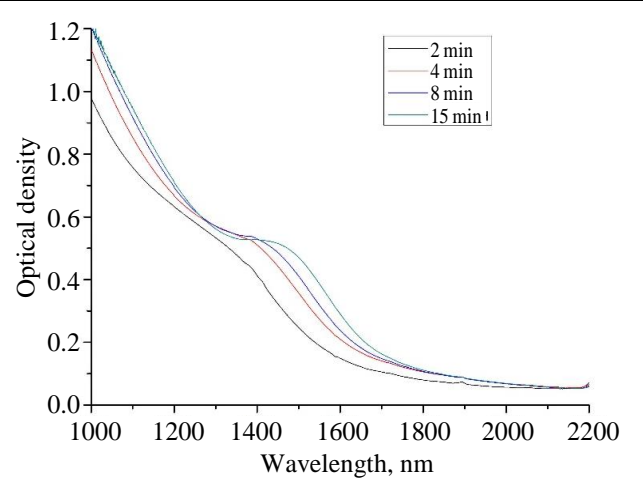


Fig. 4. Absorption spectra of PbS CQD samples collected during synthesis at a temperature of 100 °C at the following time points: 1-2 min; 2-4 min; 3-8 min; 4-15 min after mixing the reagents

PbS nanoparticles obtained by this method at a temperature of 100 °C have a spherical shape. To determine the crystalline phase of nanocrystals, the selected area electron diffraction (SAED) method was used (Fig. 5a, b). In the SAED electron diffraction pattern, reflections from the planes (111), (200) and (220) are observed, characteristic of the cubic syngony, confirming the structure of galena [17]. These PbS CQDs have an average diameter of 5.5 nm according to TEM data, which is in good agreement with the measured absorption spectra and the size calculation using the relationship between the transition energy and the nanoparticle diameter [18]:

$$E_0 = 0.41 + \frac{1}{0.0252d^2 + 0.283d}$$

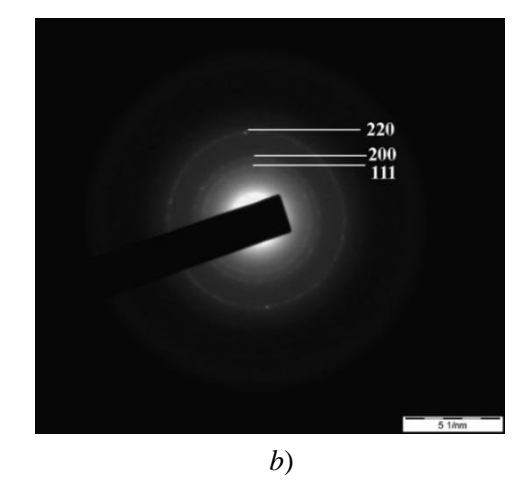


Fig. 5. TEM image and SAED electron diffraction pattern of PbS quantum dots obtained at 120 °C

Measurement of the Fourier-transform IR spectra of a thin film of PbS CQDs obtained by evaporating the solvent from the film of PbS CQD sol on Ge crystals of the ATR attachment showed (Fig. 6) that the most intense signals of asymmetric and symmetric vibrations of CH₂ groups are 2923 cm⁻¹ 2854 cm⁻¹. and observed The signals of medium intensity at 1525 cm⁻¹ and 1403 cm⁻¹ correspond to asymmetric and symmetric vibrations of the carboxylate anion COO of oleic acid from the ligand shell. The presence of two carboxyl anion peaks in the spectrum of quantum dots indicates bidentate coordination of oleate on surface of PbS CQDs. Thus, the Fourier IR spectroscopy data confirm the presence of oleic acid in the ligand shell of the PbS CQD nanoparticles and its coordination.

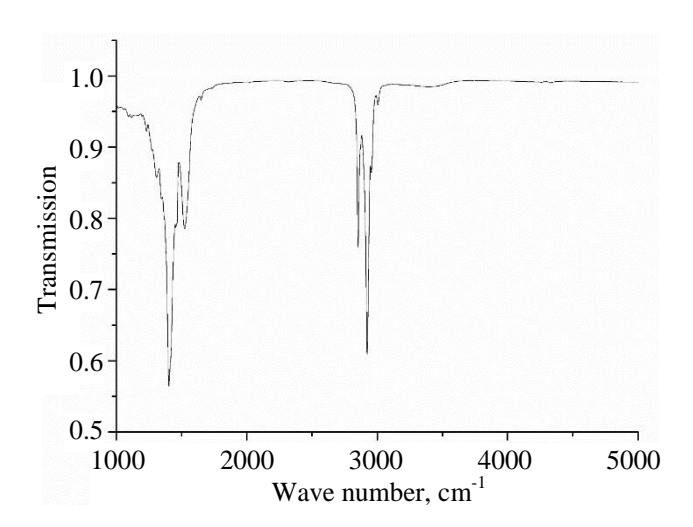


Fig. 6. ATR-FTIR spectrum of PbS CQD thin film

Conclusion

In this work, it was shown for the first time that decene-1 can be used to obtain nanoparticles and, in particular, PbS CQDs as a solvent. It was established that commercial pure grade decene-1 of Russian production, containing aromatic hydrocarbons as impurities, is suitable. Using our method, it is possible to obtain PbS CQD samples with the first exciton peak in the wavelength range

from 1170 to 1530 nm. It has been shown that it is possible to vary the sizes of the obtained PbS CQDs by varying the reaction temperature, while the size distribution does not change significantly with temperature. Using Fourier-transform IR spectroscopy, the composition of the ligand shell of the obtained CQDs was shown.

The authors express their gratitude to *P. N. Pilipenko for the chromatogram of decene-1.*

The work was carried out with the financial support of the Russian Science Foundation project No. 23-23-00300.

REFERENCES

- 1. Ponomarenko V. P., Popov V. S., Shuklov I. A., Ivanov V. V. and Razumov V. F., Russ. Chem. Rev. **93**, RCR5113 (2024).
- 2. Shuklov I. A. and Razumov V. F., Russ. Chem. Rev. **89**, 379 (2020).
- 3. Hinds S., Klem E., Gregory C., Hilton A., Hames G. and Violette K., Infrared Technology and Applications XLVI. SPIE **11407**, 11–19 (2020).
- 4. Bullen C. R. and Mulvaney P., Nano Letters **4** (12), 2303–2307 (2004).
- 5. Antanovich A., Prudnikau A. and Artemyev M., The Journal of Physical Chemistry C **118** (36), 21104–21109 (2014).
- 6. Lucey D. W., MacRae D. J., Furis M., Sahoo Y., Cartwright A. N. and Prasad P. N., Chemistry of Materials **17** (14), 3754–3762 (2005).
- 7. Li Z., Ji Y., Xie R., Grisham S. Y. and Peng X., Journal of the American Chemical Society **133** (43), 17248–17256 (2011).
- 8. Chen O., Chen X., Yang Y., Lynch J., Wu H., Zhuang J. and Cao Y. C., Angewandte Chemie International Edition **47** (45), 8638–8641 (2008).
- 9. Evans C. M., Evans M. E. and Krauss T. D., Journal of the American Chemical Society **132** (32), 10973–10975 (2010).
- 10. Baranov D., Lynch M. J., Curtis A. C., Carollo A. R., Douglass C. R., Mateo-Tejada A. M. and Jonas D. M., Chemistry of Materials **31** (4), 1223–1230 (2019).
- 11. Ganeev R. A., Shuklov I. A., Zvyagin A. I., Dyomkin D. V., Bocharova S. I.,

- Popov V. S., Toknova V. F., Lizunova A. A., Ovchinnikov O. V. and Razumov V. F., Optical Materials **121**, 111499 (2021).
- 12. Shuklov I. A., Toknova V. F., Lizunova A. A. and Razumov V. F., Materials Today Chemistry **18**, 100357 (2020).
- 13. Shuklov I. A., Toknova V. F., Demkin D. V., Lapushkin G. I., Nikolenko L. M., Lizunova A. A., Brichkin S. B., Vasilets V. N. and Razumov V. F., High Energy Chemistry **54** (3), 183–188 (2020).
- 14. Shuklov I. A., Dyomkin D. V., Konavicheva V. A., Popov V. S. and Razumov V. F., J. Commun. Technol. Electron. **68** (2), S184–S189 (2023).

- 15. Ullmann's encyclopedia of industrial chemistry. Elvers B.: Verlag Chemie Hoboken, NJ, 1991.
- 16. Brennan J. A., Industrial & Engineering Chemistry Product Research and Development **19** (1), 2–6 (1980).
- 17. Beygi H., Sajjadi S. A., Babakhani A., Young J. F., van Veggel F. C. J. M., Appl. Surf. Sci. **457**, 1–10 (2018).
- 18. Moreels I., Lambert K., Smeets D., De Muynck D., Nollet T., Martins J. C., Vanhaecke F., Vantomme A., Delerue C., Allan G. and Hens Z., ACS Nano 3, 3023.1 (2009).

PHOTOELECTRONICS =

UDC 551.46.0 PACS: 07.20.Ka EDN: ZZEFNY

Hybrid photodetection module for optical-television underwater imaging systems

Yu. K. Gruzevich, P. S. Alkov, L. M. Balyasny, D. V. Volkov

The possibility of creating laser optical television active-pulse underwater imaging systems based on photodetection modules (PDMs) with a sensitive structure of a third-generation electro-optical converter (EOC) with a "blue" GaAs photocathode, sensitive in the spectral range of seawater transparency $\Delta\lambda = (400 \div 550)$ nm coupled via fiber-optic elements with large-format digital CMOS matrices that enable the formation of video images of underwater objects in scattering seawater, is demonstrated.

Keywords: underwater imaging; EOC; active-pulse system; pulse laser; photocathode; quantum efficiency.

DOI: 10.51368/1996-0948-2025-1-70-77

Introduction

High sensitivity of the third-generation EOC with a "blue" GaAs photocathode in the spectral range of $\Delta\lambda = (400 \div 550)$ nm is

Yury K. Gruzevich^{1,2}, Deputy Director General,

Candidate of Technical Sciences, Professor E-mail: yukg@mail.ru

Pavel S. Alkov¹, Deputy Technical Director,

Candidate of Technical Sciences E-mail: pavel_alkov@mail.ru

Dmitry V. Volkov¹, Lead Engineer E-mail: mitya_volkov_7554@bk.ru **Lev M. Balyasny**¹, Chief Designer

E-mail: baliaska@mail.ru

OAO NPO GEOFIZIKA-NV

Bd. 2, 23, Matrosskaya Tishina st., Moscow, 107076 Russia

² Bauman Moscow State Technical University Bd. 1, 5, 2-nd Baumanskaya st., Moscow, 105005 Russia

Received January 28, 2025 Revised February 10, 2025 Accepted February 14, 2025 Scientific specialty code: 1.3.11

© Yu. K. Gruzevich, P. S. Alkov, D. V. Volkov, L. M. Balyasny, 2025

ensured by optimizing the thickness and composition of the buffer layer of the photocathode unit (PCU) of the third-EOC. generation By changing the composition and design of the buffer layer of the PCU, the scientists gained to obtain a GaAs photocathode with negative electron (NEA photocathode) affinity composition of PDM samples with a quantum efficiency of up to 30 % at a second harmonic wavelength of 532 nm of a pulsed Nd:YAG laser.

One of the scopes of development of optoelectronic systems underwater for operations related to the search, detection, and identification of unmanned underwater vehicles, sunken objects, as well as the detection of mine danger and sea saboteurs, combating sea terrorism, monitoring pipelines, underwater cables and wells is the creation of optical television systems that provide data on underwater objects not only for the purpose of their detection and location, but also for their recognition and identification by obtaining images.

Images of underwater objects can be using laser optical television obtained active-pulse underwater imaging systems (APUIS), which generate video images of underwater objects in scattering sea water based on the use of the active-pulse observation method proposed by the Russian Professor A. A. Lebedev in 1936 The method consisted of illuminating the observed space with pulses of optical radiation with a duration shorter than the propagation time of the pulses to the objects of observation, and in the synchronized reception of optical signals reflected from these objects of observation. This method ensures observation of a limited depth of the surrounding underwater space and sharply reduces the dependence of observation on the illumination conditions of the observed objects and the surrounding backgrounds (overlying water or bottom surface), as well as natural optical interference such as sea water and algae, as well as dissolved and suspended substances of organic and inorganic origin contained in it. Thus, the use of the active-pulse method of forming underwater video images allows eliminating the "parasitic" effect of backscatter interference of the illuminating radiation, which is superimposed on the useful image of the observed underwater objects, reducing their contrast and. consequently, visibility range, and often completely losing visibility of underwater objects, especially with reduced transparency of sea water.

The implementation of active-pulse mode technology has led to the creation of devices that provide underwater imaging on a monitor due to combined optical television, laser, and optical technical solutions. The practical significance of the active-pulse mode lies in achieving record-breaking ranges for forming images of underwater objects compared to other optical and optoelectronic devices, including high-frequency sector-scanning sonars operating under identical conditions [2].

The transition to a whole new level of obtaining visual information has expanded the naturally limited capabilities of the human eye for observing underwater objects in the spectral range of sea water transparency, at levels of illumination certain underwater observation space, ensuring the observation range depending on the transparency of sea water and allowing the operator to conduct observation underwater in complete darkness even in the absence of solar radiation. This ensures high-quality imaging of distant underwater objects in highly scattering seawater, where the use of standard cameras operating in conjunction with searchlights does not allow to detect and recognize underwater objects.

To solve the problem, APUIS can be located on underwater manned and unmanned complexes, remotely controlled underwater vehicles, and other underwater objects (Fig. 1a). However, to solve a number of problems, the use of APUIS as part of underwater vehicles is associated with major technical difficulties. In such cases, it is advisable to carry out search and rescue operations using APUIS installed on aircraft (A), e.g., a helicopter (Fig. 1b) or unmanned aerial vehicles (UAVs). At the same time, the search time for underwater objects from an aircraft is significantly reduced due to the increased area of coverage.

In this regard, the task arises of forming images of underwater objects and assessing the quality of the image recorded by the laser APUIS through the disturbed air-water interface, which deteriorates mainly due to the influence of the following key factors:

- most of the radiation falling on the sea surface is absorbed and scattered by sea water, which leads to a limitation of the depth of the observed space;
- the reflected signal from underwater objects is very weak, and the background noise of the ocean is high, which directly affects the processing and formation of the image;

- multiple scattering and fluctuations in the distribution of underwater illumination caused by the random nature of the refraction of radiation on a rough surface leads to blurring of the image of underwater objects and disruption of the image topology.

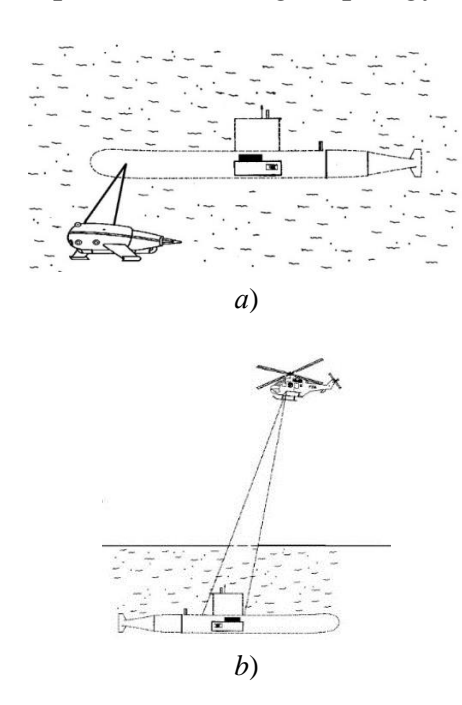


Fig. 1. Schematic diagram of image formation by an active-pulse underwater vision system

To obtain an image of underwater objects and solve the problem of assessing the image quality, the theory of transferring the image of underwater objects through a disturbed water surface and the water column is used. Until now, the main efforts have been focused establishing analytical relationships between statistically average image characteristics and the conditions of observation of an incompletely averaged image. The task of correctly describing the characteristics of a not fully averaged image can be significantly simplified under the condition that the time of propagation of one probing laser pulse to the observed underwater object and back through the airwater interface, as well as the inertia of the PDM of the optical television recording channel of the system, must be much shorter than the characteristic time of change in the shape of the disturbed sea surface, which can

be considered "frozen" during the formation of a single image. With this approach, it is possible to estimate the distortions introduced into the statistically average image by the processes of multiple scattering and absorption of radiation in an aqueous medium and random refraction at a disturbed boundary [2].

Therefore, for the practical use of this method for the detection and recognition from an aircraft of small-sized underwater objects in real time and in conditions of disturbed scattering sea water, the recording channel of the APUIS should be created on the basis of a high-speed PDM, highly sensitive in the spectral range of sea water transparency, and the illumination channel should be based on the highly efficient pulsed laser emitting in the spectral range of sea water transparency.

The spectral characteristic of sea water transmission in the optical spectral range is shown in Fig. 2, from which it is evident that sea water is transparent only in the spectral range $\Delta\lambda = (400 \div 550)$ nm. At the same time, the absorption of optical radiation in the UV spectral range is ~10⁹ times greater, and in the IR spectral region ~10⁶ times greater, than the absorption in the working (blue-green) spectral range [3].

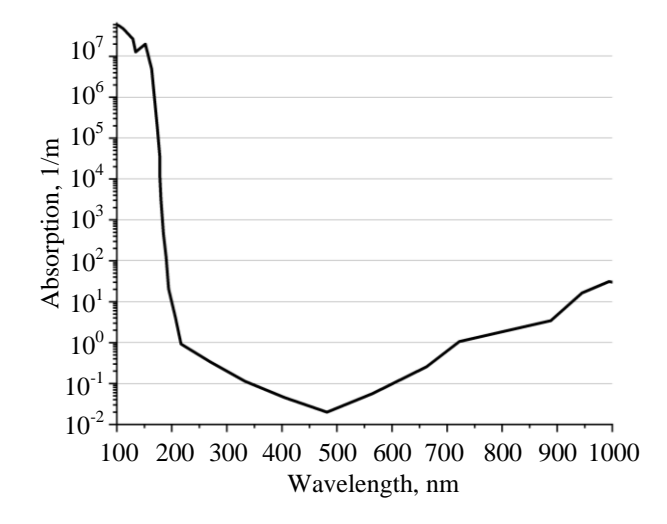


Fig. 2. Spectral characteristic of sea water transmission

Currently, there are no optical television underwater imaging systems on the market

that fully satisfy modern requirements. Therefore, the work on the creation of the APUIS required conducting comprehensive fundamental develop research to technologies fundamentally new and technical solutions that would significantly increase the range of the APUIS installed on an aircraft and improve the quality of the generated image of underwater objects by creating:

- high-speed, high-resolution digital PDMs, highly sensitive in the spectral range of seawater transparency $\Delta\lambda = (400 \div 550)$ nm;
- high-speed, highly efficient, smallsized pulsed lasers emitting in the spectral range of seawater transparency, used to illuminate various underwater objects;
- a tunable digital controller that generates synchronizing and control pulses sent to the PDM and the illuminating pulsed laser, as well as distributes laser pulses within the strobe according to a specified law, reducing the impact of backscatter interference from natural optical noise on the target observation image;
 - specialized computers and software.

The key element that ensures detection and recognition of small-sized, lowcontrast underwater objects in the absence of illuminating solar radiation, at great depths against the background of the seabed and in conditions of a highly scattering aquatic environment, is the PDM specially developed by OAO NPO Geofizika-NV based on a third-generation EOC, sensitive in the spectral range of seawater transparency, coupled with a high-resolution digital CMOS matrix, which will ensure the high-speed formation of multiply enhanced images of underwater objects [4]. OAO NPO Geofizika-NV carried out research on the creation and active-pulse modernization of optical television systems based on third-generation EOC with GaAs NEA photocathode. Fig. 3 shows the spectral characteristics of various photocathodes sensitive in the spectral range of seawater transparency $\Delta \lambda = (400 \div 550)$ nm [4].

From the given characteristics it is evident that at a wavelength of 532 nm the following photocathodes have sensitivity in the spectral range $\Delta\lambda = (400 \div 550)$ nm:

- thin multi-alkali photocathode S-20
 (up to 15 % quantum efficiency);
- GaAs-based NEA photocathode (at least 25 % quantum efficiency);
- GaAsP-based NEA photocathode
 (more than 50 % quantum efficiency) [5].

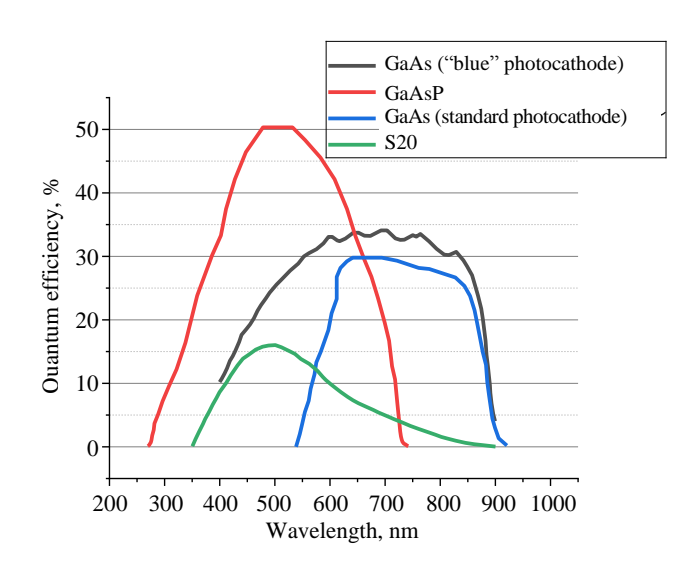


Fig. 3. Spectral characteristics of photocathodes

The analysis showed that the II+ generation EOCs based on S-20 multi-alkaline photocathodes have a number of disadvantages that limit their use in the composition of the ODM for the APUIS:

- firstly, they have significantly lower photosensitivity compared to other types of photocathodes;
- secondly, they have high specific resistance of photocathodes, which will not allow strobing with short pulses (up to tens of nanoseconds).

Fig. 3 shows the spectral characteristics of a standard NEA photocathode based on GaAs, which is intended for third-generation EOC used in night vision devices. Considering that the short-wavelength limit of the NEA photocathode photosensitivity is determined by the thickness and composition of its buffer layer, which is located on the surface of the input window of the EOC in

front of the active GaAs layer, the quantum efficiency of a standard GaAs photocathode at a wavelength of 532 nm is even less than that of the S-20 multi-alkali photocathode.

Currently, OAO NPO Geofizika-NV produces third-generation EOC with standard GaAs-based photocathodes with a Ga $_{0.4}$ Al $_{0.6}$ As buffer layer of about 1 μ m and an active GaAs layer of about 1.5 μ m. With such a ratio of the thicknesses of the PCU layers, the spectral range of operation of the third-generation EOC based on this PCU is $\Delta\lambda = (590 \div 930)$ nm, and such EOC is intended for operation in night vision devices, in which the sensitivity of the PCU in the blue-green region of the spectrum worsens the operation of night vision devices.

To ensure high sensitivity of the third-generation EOC with GaAs-based NEA photocathodes in the spectral transmission range of sea water (Fig. 2), it is necessary to provide a thin buffer layer of about $0.01~\mu m$ in the design of the PCU. However, when manufacturing a PCU with such a thin layer, it may be damaged by mechanical and chemical influences. Therefore, it was decided to produce, in addition to the thin buffer layer, a layer of variable composition (gradient layer) with a total thickness of $0.1~\mu m$.

The design of this PCU structure is shown in Fig. 4. The single-crystal substrate 6 is chemically removed by etching after thermocompression bonding with the glass, and the stopper layer 7 is chemically removed after etching off the substrate 6.

To ensure the matching of the layers of the heteroepitaxial structure of the PCU according to the parameters of the crystal lattice, the maximum permissible amount of aluminum in the buffer layer should not exceed 70 %, which also ensures good optical transmission of the PCU. The thickness of the active layer of the PCU is also of great importance.

Reducing the thickness of the working layer from 1.5 μ m to 0.35–0.45 μ m reduces unwanted absorption of IR radiation, which reduces the contrast of the image of underwater objects. In addition, the SiO₂ antireflection coating with a thickness of about 1.0 nm for the IR region of the spectrum, is not optimal for the blue-green spectral range of seawater transparency, for which the optimal thickness of the SiO₂ anti-reflection coating is about 0.7÷0.75 nm.

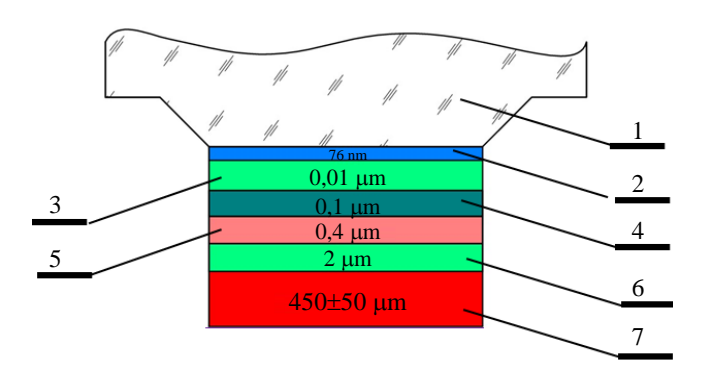


Fig. 4. Schematic diagram of the design of a third-generation EOC PCU with a NEA photocathode based on GaAs. 1 – glass entrance window; 2 – anti-reflection and diffusion barrier layer SiO₂; 3 – buffer layer Ga_xAl_{1-x}As; 4 – gradient layer; 5 – active layer GaAs; 6 – stopper layer; 7 – single-crystal substrate GaAs

The discussed remarks have been implemented by OAO NPO Geofizika-NV in the upgraded design of the heteroepitaxial structure of the PCU, the values of which are presented in Table 1, used to create third-generation EOC with NEA photocathodes based on GaAs, which exhibit high sensitivity in the spectral range of seawater transparency. Such EOCs are called third-generation EOCs with a "blue" photocathode.

After the production of the PCU, the process of its activation and assembly of the vacuum block of the third-generation EOC with a "blue" photocathode is carried out in an ultra-high-vacuum final assembly unit (FAU) [4].

Tabla	1
1 abie	1

Seq. No.	Layer name	Layer composition	Alloying level, cm ³	Layer thickness, µm
1	2	3	4	5
1	Anti-reflective diffusion-barrier	SiO_2	_	0.076
2	Buffer	p-Al _{0.7} Ga _{0.3} As:Zn	5.9×10 ¹⁷	0.01
3	Gradient variable composition	p-Al _{0.7} Ga _{0.3} As	5.9×10 ¹⁷	0.1
		<i>p</i> -GaAs:Zn		
4	Active	p-GaAs:Zn	6.6×10^{18}	0.4
5	Blocking	p-Al _{0.6} Ga _{0.4} As:Zn	5.9×10 ¹⁷	2.0
6	Substrate	n-GaAs:Si (100)	5×10 ¹⁷	450±25

Thermal cleaning and activation of the PCU with cesium and oxygen are carried out in a separate chamber, and the assembly of the vacuum block is carried out in another sealing chamber, which ensures a low noise level and high sensitivity of the PCU.

To obtain a high quantum yield in the required spectral range, the photocathode is activated by filtering the exciting radiation, for example, using colored glass ZS8 or an interference filter.

As a result of the work carried out by OAO NPO GEOFIZIKA-NV, samples of the third-generation EOCs with a "blue" photocathode with a quantum efficiency of up to 25 % at a wavelength of 532 nm were created. The spectral sensitivity characteristics of the created samples of the third-generation EOC are shown in Fig. 5.

Considering that at present the most promising photocathode for solving underwater imaging problems is the NEA photocathode based on the ternary compound GaAsP, the spectral characteristics of such a photocathode from HAMAMATSU PHOTONICS are shown in Fig. 3, and OAO NPO Geofizika-NV is actively working in this direction.

To create an APUIS based on the developed third-generation EOC with a

"blue" photocathode, highly sensitive in the spectral range of seawater transparency, specialists at OAO NPO Geofizika-NV have developed a highly efficient ODM of the FPM-5-1 type, in which the third-generation EOC is coupled with a high-resolution and high-speed digital CMOS matrix through a direct fiber-optic element (FOE) to obtain video images [4].

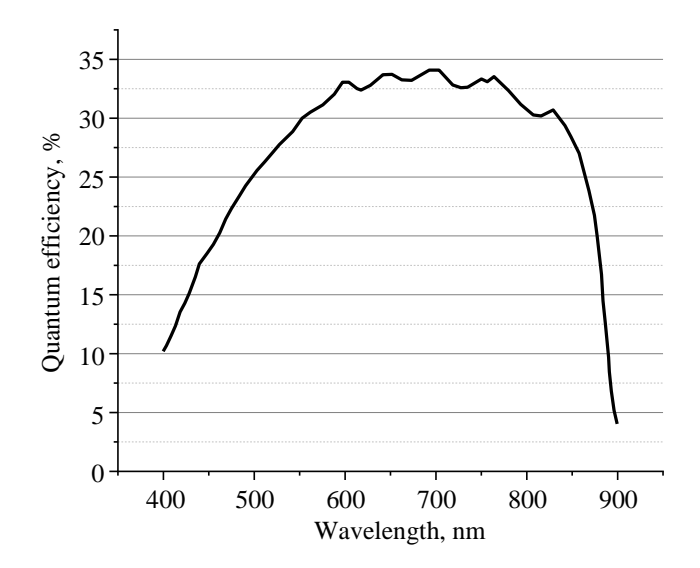


Fig. 5. Spectral characteristics of the third-generation EOC with a "blue" photocathode with a buffer layer optimized in thickness and composition

The main parameters of the developed PDM type FPM-5-1 are given in Table 2.

Table 2

Parameter Parameter va	
Spectral sensitivity range, μm	0.4-0.7
Integral sensitivity, µA/lm	2500
Spectral sensitivity (530 nm), mA/W	150
Working television resolution by field, TVL	450
Maximum frame rate, Hz	100
Signal to noise ratio ($E = 10^{-4} \text{ lux}$)	20
Power supply voltage, V	12
Consumption current, mA	250
Output frame format, pixel	2200×1024
Output signal bit depth, bit	12

Fig. 6 shows the external appearance of the FPM-5-1 type module [4].



Fig. 6. Appearance of FPM-5-1 type photoreceiving modules and the EOC vacuum block coupled with a camera based on a CMOS matrix

The use of a fiber optic transfer lens results in losses in spatial resolution and characteristics of the transferred energy optical image. The most promising development of the receiving system is the use of designs in which a digital CMOS matrix is placed inside the vacuum volume of the EOC and is excited directly by an electron beam containing information about the image of underwater objects. At the same time, losses are significantly reduced, since there is no focon for image transfer, and amplification of the electron flow is achieved by bombarding the back side of a specially thinned **CMOS** matrix. The noise characteristics of this hybrid device are significantly better than those of a traditional PDM Currently, both in Russia, in particular at OAO NPO Geofizika-NV, and abroad, the development of promising hybrid PDMs is underway, which are also photosensitive in the spectral range of sea water transparency.

The active-pulse method of forming underwater images is closely connected with the development of pulsed illumination means, and, above all, with the creation of highly efficient pulsed lasers. The working body is a Nd:YAG crystal. Development of modern highly efficient pulsed lasers. The pumping of the laser's active medium is carried out by diode light-emitting arrays, and O-switching is performed by an electroshutter. The doubling optical of generation frequency (at a wavelength of 532 nm) is achieved by an element based on a (potassium titanyl phosphate KTiOPO₄) crystal, which ensures radiation in the spectral region of seawater transparency (Fig. 2). The developed Nd:YAG lasers provide a pulse duration (at the 0.5 level) of the order of tens of ns with a pulse energy from several hundred µJ to tens of mJ.

An assessment of the average power of laser radiation, carried out by various authors, including during full-scale tests of a model of an underwater imaging camera developed at OAO NPO Geofizika-NV, shows that due to the significant absorption and scattering of laser radiation by a layer of sea water, significant pulse energy and average laser power are required. For each specific application, it is necessary to evaluate the required parameters of the illuminating laser radiation, according to which a specific laser is selected.

Conclusion

The article shows the possibility of creating laser optical television active-pulse underwater imaging systems based on photodetection modules (PDMs) with a sensitive structure of a third-generation EOC with a "blue" GaAs photocathode, sensitive in the spectral range of seawater transparency $\Delta\lambda = (400 \div 550)$ nm coupled via fiber-optic elements with large-format digital CMOS matrices that enable the formation of video images of underwater objects in scattering seawater, is demonstrated.

High sensitivity of the third-generation EOC with a "blue" GaAs photocathode in the spectral range of $\Delta\lambda = (400 \div 550)$ nm is ensured by optimizing the thickness and composition of the buffer layer of the photocathode unit (PCU) of the third-generation EOC. By changing the composition and design of the buffer layer of the PCU, it was possible to obtain a NEA GaAs photocathode in the composition of

PDM samples with a quantum efficiency of up to 25 % at a second harmonic wavelength of 532 nm of a pulsed Nd:YAG laser.

Further improvement of the APUIS can be associated with the development of NEA photocathodes based on the GaAsP structure, which currently has a quantum efficiency of up to 50 % at a wavelength of 532 nm [5].

REFERENCES

- 1. Volkov V. G., Special Technics, No. 5 (2001).
- 2. Karasik V. E. and Orlov V. M., Laser location vision systems. Moscow, N. E. Bauman MGTU, 2013.
- 3. Dolin L. S. and Levin I. M., Theory of underwater vision. Leningrad, Gidrometeoizdat, 1991.
- 4. Gruzevich Yu. K., Optoelectronic night vision devices. Moscow, FIZMATLIT, 2014.
- 5. Catalog of the company «HAMAMATSU PHOTONICS»:

https://www.hamamatsu.com/content/dam/hamamatsu

photonics/sites/documents/99_SALES_LIBRARY/etd /II_TII0007E.pdf (date of access: 01.02.2025).

PHYSICAL SCIENCE OF MATERIALS

UDC 538.975 PACS: 82.35 Np EDN: KKUECG

Mechanisms of interaction of polyvinyl alcohol molecules and carbon nanoparticles in aqueous solutions

S. V. Likhomanova, N. V. Kamanina

The paper presents the results of the study of the spectral characteristics and viscosity parameters of aqueous solutions of polyvinyl alcohol (PVA) sensitized with an aqueous solution of graphene oxide at various concentrations (with reference to the dry substance of PVA) and carbon nanoparticles (fullerene C_{70} and single-walled carbon nanotubes (SWCNT)) at a concentration of 0.1 wt.%. The obtained electronic spectra of PVA clear solutions exhibit absorption at a wavelength of 275–280 nm of the functional carbonyl group (C=O), which is a part of polyvinyl alcohol. The graphene oxide applied in the form of an aqueous solution neutralizes the electronic transition of the carbonyl group, which results in the absence of an absorption peak in the UV band. Sensitization with C_{70} nanoparticles and SWCNT preserves all the transitions typical of polyvinyl alcohol. The decrease in viscosity of PVA-graphene oxide solutions is associated with the increased spacing between polyvinyl alcohol molecules due to the graphene oxide layers placed between them. The increase in viscosity for PVA aqueous solutions sensitized with C_{70} and SWCNT is due to the presence of large clusters of carbon nanoparticles that do not interact with PVA polymer molecules.

Keywords: polyvinyl alcohol; graphene oxide; carbon nanotubes; fullerenes; electronic transitions; dynamic viscosity.

DOI: 10.51368/1996-0948-2025-1-78-83

Introduction

Polyvinyl alcohol is a polymer material featuring unique characteristics that make it

an attractive item to be researched with an aim of improving mechanical, optical, electrical and other parameters [1–5]. An ability to form flexible and durable

Svetlana V. Likhomanova^{1,2,3}, research assistant, assistant professor, Candidate of of Physics and Mathematics

E-mail: lsv-87@bk.ru

Natalia V. Kamanina^{1,3,4}, leading research assistant, head of department, Doctor of Physics and Mathematics

¹ JSC "Research and Production Corporation S. I. Vavilova"

Bd. 1, 36, Babushkina st., Saint Petersburg, 192171 Russia

² Saint Petersburg State University of Aerospace Instrumentation.

67, Bolshaya Morskaya st., Saint Petersburg, 190000 Russia

³NRC "Kurchatov Institute" – PNPI

1, Orlova Roshcha microdistrict, Gatchina, Leningrad region, 188300 Russia

⁴ETU "LETI"

5, Professora Popova st., Saint Petersburg, 197022 Russia

Received August 19, 2024 Revised December 27, 2024 Accepted January 14, 2025

© S. V. Likhomanova, N. V. Kamanina, 2025

optically transparent films can be distinguished among main advantages of PVA. Due to its film-forming properties, PVA can be used as a basis for creating thin-film polarizers. It should be noted that the ability to control the polarized light is widely used in modern optoelectronic applications, for example, in liquid crystal displays [6, 7].

A number of earlier studies have shown the progress in optical characteristics of polarizers based on polyvinyl alcohol, the volume of which was sensitized with carbon (graphene oxide, C₇₀ fullerene and shungite) and quartz nanoparticles [8, 9]. The results of the work demonstrate an increase in the transmission of the parallel light component in the wavelength range of 500-750 nm. To explain the data observed, an assumption has been made that PVA polymer chains are oriented more uniaxially due to the formation of an additional orienting framework of carbon nanoparticles. According to the classic technology of producing iodine-polyvinyl alcohol polarizers, after the transparent PVA film is colored in the iodine solution. moistened films are exposed to mechanical stretching. The degree of stretching impacts the arrangement of PVA lamellas relative to each other. Since PVA chains where iodine atoms are built in are oriented strictly in parallel, maximum absorption of the crossed light component takes place. If molecules are located at certain angles, the resulting polarization will be partial.

The aim of this work was to study the mechanisms of interaction of PVA polymer molecules and carbon nanomaterials by measuring the dynamic viscosity and absorbency of PVA-carbon sensitizer solutions.

Experimental section

To study the mechanisms of interaction of a PVA polymer molecule with carbon nanosensitizers, the optical parameters of 1 % aqueous solutions of polyvinyl alcohol were analyzed. PVA grade 40/2 was used for preparing a solution [10]. The above-mentioned grade of polyvinyl alcohol is recommended for making optical polarizers based on Russian-manufactured components. The PVA concentration was 1 wt.% of a solvent (distilled water). The required amount of dry PVA was left in distilled water for twentyfour hours for the polymer molecules to swell, after which a homogeneous transparent aqueous solution of PVA was obtained by stirring at a water bath temperature of 100 °C continuously. for four hours Carbon sensitizers were added to the main solution after it had cooled down to a temperature of about 35 °C (Fig. 1). The sensitized solution of PVA was mixed additionally. An aqueous solution of graphene oxide, C₇₀ fullerenes and single-walled carbon nanotubes played a role of sensitizers. The concentration of fullerene and SWCNTs was 0.1 wt.% relative to dry PVA. Fullerene C₇₀ powder with a mixture purity of 97%, as well as carbon nanotubes (SWCNTs, type #704121, with a diameter varying in the range of 0.7–1.1 nm), were purchased from Aldrich Co. A polyvinyl solution with graphene alcohol at three concentrations of was studied the sensitizer: 0.05, 0.1, and 0.15 wt.%. These concentrations were considered as part earlier polarization of studies of characteristics of iodine-polyvinyl alcohol polarizers [11]. It should be noted that graphene oxide was purchased from a Russian manufacturer, NanoTechCenter LLC in Tambov. After analyzing the data shown in Figure 1 (see bottles Nos. 2–4) for such

compounds, on can say that homogeneous composites were obtained, and the change in

their color is associated with an increased concentration of the graphene sensitizer.

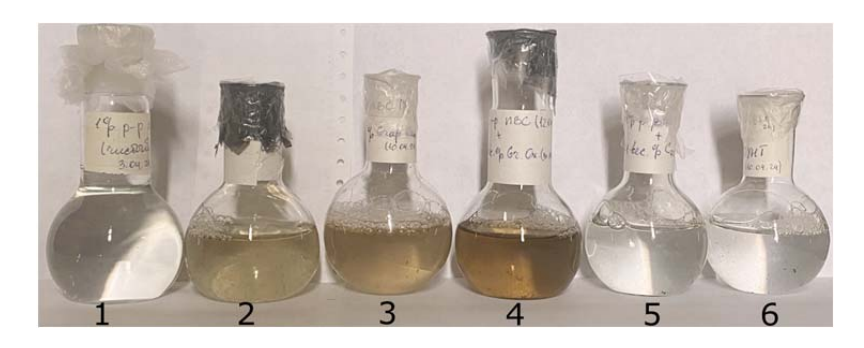


Fig. 1 Aqueous solutions of 1% polyvinyl alcohol after being sensitized: $1 - \text{non-sensitized } PVA \text{ solution; } 2 - 0.05 \text{ wt. } \% \text{ of graphene oxide; } 3 - 0.1 \text{ wt. } \% \text{ of graphene oxide; } 4 - 0.15 \text{ wt. } \% \text{ of graphene oxide; } 5 - 0.1 \text{ wt. } \% \text{ of } C_{70} \text{ fullerene; } 6 - 0.1 \text{ wt. } \% \text{ single-walled carbon nanotubes}$

The transmittance spectra in the UV and visible bands of 1% PVA solutions with carbon sensitizers were studied with SF-26 spectrophotometer. The absorbency (*D*) of samples was calculated based on the transmittance values obtained. The data are shown in Figure 2.

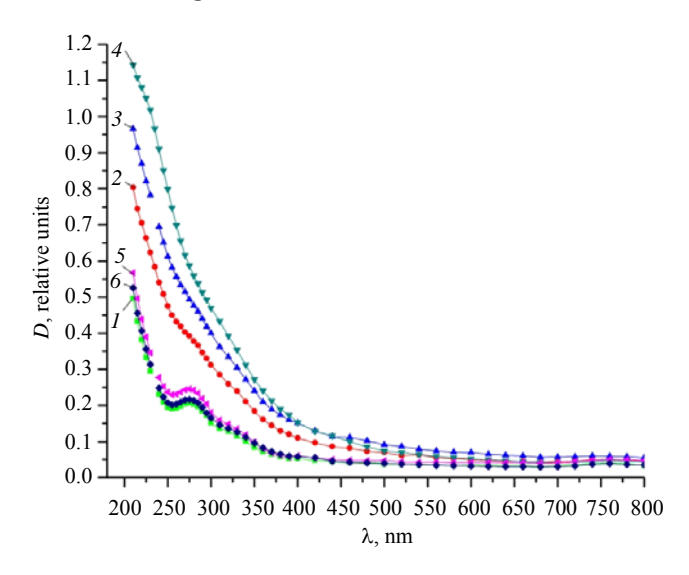


Fig. 2 Absorbency of 1% aqueous solutions of polyvinyl alcohol after being sensitized:

1 – non-sensitized PVA solution; 2 – 0.05 wt. % of graphene oxide; 3 – 0.1 wt. % of graphene oxide; 4 – 0.15 wt. % of graphene oxide; 5 – 0.1 wt. % of C₇₀ fullerene; 6 – 0.1 wt. % single-walled carbon nanotubes

Analysis of the curves has shown that sensitization with graphene oxide results in the change of solutions' absorbency in the UV band. For a 1% solution of polyvinyl alcohol with graphene oxide, at a wavelength of 275-280 nm and at all the considered concentrations of the nanomaterial, there are no peaks (Fig. 2, curves 2-4) typical of nonsensitized PVA (curve 1). The dynamic viscosity of the solutions was also measured SV-1A vibroviscometer using (A&D Company Limited (Japan)). The dynamic viscosity values in the work are expressed in relative units (η) , because the task was to compare the data for sensitized and nonsensitized 1 % solution of polyvinyl alcohol (Fig. 3).

Sensitization of an aqueous 1 % solution of polyvinyl alcohol with graphene oxide reduces the viscosity by 5–13 % relative to the non-sensitized PVA solution. The PVA solutions with C_{70} fullerene and SWCNTs have a higher viscosity value differing by 13 % and 8 %, respectively.

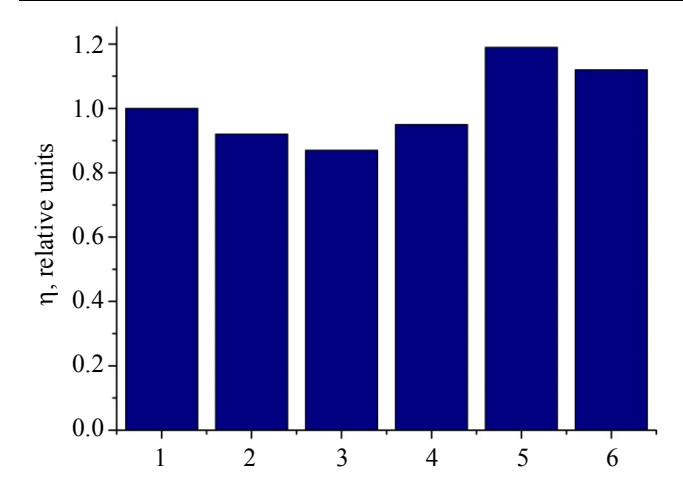


Fig. 3. Dynamic viscosity of 1% aqueous solutions of polyvinyl alcohol after being sensitized: 1 – non-sensitized PVA solution; 2 – 0.05 wt. % of graphene oxide; 3 – 0.1 wt. % of graphene oxide; 4 – 0.15 wt. % of graphene oxide; 5 – 0.1 wt. % of C70 fullerene; 6 – 0.1 wt. % single-walled carbon nanotubes

Discussion of the results

Polyvinyl alcohol has the chemical $(CH_2CHOH)_n$. However, formula molecule may contain small amounts of other chemical groups: carbonyl, acetate, ether bridges and other structural heterogeneities [12]. The absorbency curve shown in Figure 2 features an absorption peak at a wavelength of 270–280 nm for the non-sensitized PVA solution and PVA solutions with added C_{70} fullerene and SWCNTs (Fig. 1, curves 1, 5 and 6). This peak is attributed to the $n \to \pi^*$ transition of the carbonyl group C=O, which disappears in an acidic environment [13]. According to the literature data, aqueous solutions of graphene oxide have a high [14,pH = 2.1-3.5. acidity 15] with Thus, when polyvinyl alcohol is sensitized with the graphene oxide solution, an unshared electron pair in the oxygen atom of the PVA carbonyl group is exposed to protonation. One of the earlier studies [11] presented a model of intermolecular interaction between PVA and graphene oxide, which was based

on the assumption that hydrogen bonds formed between the PVA hydroxyl groups and the oxygen ions of graphene functional groups. The relationship observed in this study between the molecules under study confirms their chemical interaction to form a stable compound. In terms of practical use, it is worth noting that a sensitizer based on graphene oxide suits more for enhancing the transmittance of a parallel light component during manufacture of thin-film light polarizers [11].

The results of viscosity measurements demonstrate its growth in solutions with fullerene nanoparticles and CNTs. The decrease in viscosity values for solutions with graphene oxide can be explained by the following reasons. First of all, the sensitizer under consideration, namely the graphene oxide, is used in the form of an aqueous solution. Thus, its addition to the PVA solution reduces the PVA concentration relative to water. The viscosity values do not decrease anymore because the volume of graphene oxide solution remains relatively small. As a second reason, a model of formation of a chemical compound between graphene oxide planes and PVA polymer molecules can be considered. Interaction including the formation of new bonds can result in an increased distance between alcohol chains, polyvinyl which, consequently, leads to lower resistance forces between PVA layers. The lowest viscosity (0.87 relative units relative to the nonsensitized solution) is observed for the PVA solution with 0.1 wt.% of graphene oxide; the use of a smaller (0.05 wt.%) and larger (0.15 wt.%) mass of the sensitizer results in the relative dynamic viscosity decreased by 8 % and 5 %, respectively. This dependence can be interpreted as estimation of the optimal concentration of the sensitizer - a small addition of graphene oxide is not sufficient to separate PVA layers most effectively, and

with a larger addition, the viscosity is contributed by graphene oxide A significant increase in viscosity of PVA with carbon nanoparticles is also associated with the presence of undissolved clusters of fullerenes and carbon nanotubes. The size of a single link of a polyvinyl alcohol molecule is about 0.257 nm [12], the diameter of a carbon nanotube varies from 0.5 to 2 nm [16], the size of an ellipsoidal C₇₀ molecule is $0.69 \text{ nm} \times 0.78 \text{ nm}$ [17]; the thickness of graphene nanoplates is as large as 2-6 nm operating principle [18].The viscometer is based on the simultaneous oscillation of two metal plates of the sensor. Accordingly, the viscosity increase can be caused by the presence of large particles in a solution, which interact with the sensor plates, thus exercising a higher resistance, and as a result, the viscosity value increases.

Conclusion

The work shows that sensitization of the polyvinyl alcohol aqueous solution with the graphene oxide solution, a bond is formed between PVA molecules and functional groups of graphene oxide. The new bond results in the change of absorbency in the sensitized PVA solution at the wavelength of 275–280 nm. Since PVA is a basis for producing optical polarizers and light filters, the observed effect, from a practical point of view, allows creating optical PVA elements with uniform increase in transmittance throughout the light spectrum.

Graphene oxide added to the PVA solution also results in decreased dynamic viscosity, while sensitization with fullerene and carbon nanotubes increases its value. Thus, it is possible to produce PVA solutions for further formation of optical films, including an option of varying the friction force between the polymer layers, and,

therefore, the final thickness of resulting films.

Finally, we note that the earlier studies of the spectral and polarization characteristics of iodine-polyvinyl alcohol polarizers sensitized with carbon nanomaterials showed an increase in the listed characteristics. The findings of the studies presented in this work along with the earlier results allow considering the sensitization of polyvinyl alcohol with carbon nanoparticles as a method for obtaining optical elements with varying parameters (optical transmittance, thickness, polarization degree).

The study was supported by a grant from the Russian Science Foundation No. 24-23-00021, https://rscf.ru/prjcard_int?24-23-00021.

REFERENCES

- 1. Mohaimeed A. A., Iraqi Journal of Nanotechnology, synthesis and application, No. 3, 59–70 (2022).
- 2. Cutroneo M., Silipigni L., Malinsky P., Slepicka P., Franco D. and Torrisi L., Polymers **16**, 1390 (2024).
- 3. Alkhaldi H., Alshorafa Z., Albarqi W., Alzahrani M. and Madani M., Materiali in tehnologije / Materials and technology **56** (1), 19–26 (2022).
- 4. Changzhi Z., Fei F., Ziyang Z., Hongliang L. and Shengjiang C., Optics and Lasers in Engineering **149**, 106798 (2022).
- 5. Majeed A. H., Nawras K. Al. Sh. and Alaa A. M., Optical and Quantum Electronics **55**, 1016 (2023).
- 6. Liu S., Li Y. and Su Y., Crystals **13**, 1639 (2023).
- 7. Choi T.-H., Lee H. W. and Uk Ha J., Appl. Opt. **62** (3), 584–591 (2023).
- 8. Kamanina N., Fedorova L., Likhomanova S., Zubtcova Y. and Kuzhakov P., Nanomaterials **14**, 737 (2024).
- 9. Kamanina N. V., Fedorova L. O. and Likhomanova S. V., Liq. Cryst. and their Appl. **24** (2), 75–82 (2024) [in Russian].
 - 10. GOST 10779-78

- 11. Likhomanova S. V., Zubtsova Y. A. and Kamanina N. V., Journal of Optical Technology **90** (7), 414–416 (2023).
- 12. Rosenberg M. E. Polymeri na osnove vinylacetata. Leningrad, Chimia, 1983 [in Russian].
- 13. Brel A. K., Vasilkova E. A., Niiazov L. N., Chaidarov A. A. and Achmedov V. N. Spectralnye metody analiza organicheskich soedinenii. Buchara, Izdatelstvo "Durdona", 2019.
- 14. Klímová K., Pumera M., Luxa J., Jankovský O., Sedmidubský D., Matějková S. and

- Sofer Z., J. Phys. Chem. C **120** (42), 24203–24212 (2016).
- 15. Dimiev A. M. Graphene oxide: a formation mechanism, a structure and chemical properties: Diss. Doctor chemical science. Kazan, KSU, 2022.
- 16. Torres-Dias A. C., Carbon. **123**, 145–150 (2017).
- 17. Eletskiĭ A. V. and Smirnov B. M., Physics-Uspekhi **36** (3), 202–224 (1993).
- 18. Melezhyk A. V. and Tkachev A. G., Nanosystems: physics, chemistry, mathematics **5** (2), 294–306 (2014).

PHYSICAL SCIENCE OF MATERIALS

UDC 551.46.9 PACS: 74.6 EDN: LPWZNH

Superconducting microcrystalline ceramics YBCO: correlation of the structure and properties

A. E. Rabadanova, S. Kh. Gadzhimagomedov, D. K. Palchaev, M. Kh. Rabadanov, Sh. P. Faradzhev, Zh. Kh. Murlieva, S. A. Mayorov, G. B. Ragimkhanov, R. M. Emirov

Ceramics of $YBa_2Cu_3O_{7-\delta}$ composition has been manufactured by solid-phase sintering to have the specified density and optimal oxygenation and demonstrate the signs of prevailing crystallite orientation along axis C. The precision X-ray diffraction analysis of the lattice thermal deformation has been performed for $YBa_2Cu_3O_{7-\delta}$ sample in the superconducting state. Raman scattering spectra have been studied with locations of peaks refined using the Lorentz function. The oxygen content and superconducting transition temperature have been estimated by studying the structure, electrical and thermal properties. The superconducting transition onset determined by the temperature dependence of electrical resistance has been shown to be accompanied by the lattice contraction followed by the growing volume in the area of T_c median values. After the transition to the superconducting state is completed, the volume change tends to zero.

Keywords: superconductivity; YBa₂Cu₃O_{7-δ}; thermal expansion; heat capacity; structure; electrical properties.

DOI: 10.51368/1996-0948-2025-1-84-91

Introduction

Superconducting materials are in demand in various practical areas, including transport, electronics, energy, medicine and aerospace industry, and are extensively used in the manufacture of engines, generators, [1-3].cables, coils, etc. Numerous experimental and theoretical studies of the structure and properties of YBa₂Cu₃O_{7-δ} (YBCO) high-temperature superconductors have been conducted recently to increase their superconducting transition temperature, T_c , and critical current density, j_c , through substitutions in the system and addition of oxides or perovskites.

YBCO superconductor has a perovskite-like structure consisting of two corrugated CuO₂ planes divided by the layer of yttrium atoms, two layers of BaO and CuO. This is an anisotropic compound with an anisotropy parameter equaling to 5. In case of high oxygen content, the material features an orthorhombic symmetry (Pmmm space group). The superconductivity and transition temperature of this material are highly dependent on the content and ordering of oxygen atoms. The oxygen nonstoichiometry for YBCO is considered to be related to the copper's mixed valence (2 and 3), which also impacts the correlation of oxygen content and lattice parameters. In the orthorhombic phase,

lattice parameters a and c decrease with the oxygen content growing while parameter b increases [4, 5].

Many essential questions concerning the superconductivity mechanism and nature of charge carriers pairing in these complex compounds remain unresolved to this day. However, it is obvious, that the high temperature of transition is caused by crystal instability and/or the abnormal lattice behavior of the phonon spectrum. particular, this instability shows as anomalies in the phonon spectrum, thermal expansion coefficient, $\alpha(T)$, at low temperatures, and singularity of elastic and acoustic properties [6-9].

The abnormal lattice parameters discovered in [9] for YBCO monocrystals near T_c , which have opposite signs in \boldsymbol{a} and \boldsymbol{b} directions, are highly dependent on the oxygen content. The paper [10] notes that lattice anomalies are caused by the dynamic, rather than static, nature of the splitting of the Cu-O bond in the CuO₂ plane. While oscillations of oxygen ions in a doublewell potential are a common property for all superconductors having a perovskite lattice. The thermal expansion coefficient anomalies observed are most likely a fundamental property of superconductors and require comprehensive study. At the first stage, to anomalies, in particular, typical thermal expansion, high-quality samples of oxide high-temperature superconductors (HTS) shall be manufactured [11].

In this work, YBCO-based samples featuring the high content of superconducting phase (up to ~ 95 %) and showing the signs of prevailing crystallite orientation along axis c have been manufactured. Findings of precision X-ray diffraction analysis of the lattice thermal deformation for the YBCO sample in the superconducting state are presented.

Experiment procedure

Microcrystalline samples were produced by solid-phase sintering using simple reagents such as Y_2O_3 (~ 99.9 %), BaCO₃ (~ 99.9 %) and CuO (~ 99.9 %) taken in equivalent proportions, according to the following reaction:

$$Y_2O_3 + 4BaCO_3 + 6CuO \rightarrow 2YBa_2Cu_3O_{7-\delta} + 4CO_2\uparrow$$

The initial reagents were mixed in an agate mortar for 5–10 hours with ethyl alcohol added. The mixed powders were pressed at a pressure of ~100 MPa and then synthesized in a furnace at a temperature of 900 °C for 20 hours at a heating rate of 3 °C/min. After the first stage, the samples were crushed, re-mixed, pressed and sintered by being heated to 850 °C for 8 hours (heating rate of 1.7 °C/min), then the temperature was increased up to 910 °C within 6 hours, to which they were exposed for 12 hours. Oxygenation was carried out at 450 °C for 10 hours.

Figure 1 shows the diagram of sintering conditions and morphology of YBa₂Cu₃O_{7- δ} compound after sintering at 910 °C for 12 hours. A ceramic surface can be seen to have a polycrystalline structure with various grain orientation on the YBCO morphology. Along with agglomerates with the size of several microns that are formed from grains of approximately ~300 nm, pores (up to ~10 μ m) and fairly large monolithic grains (up to ~30 μ m) of irregular shape but with a typical facet pattern can be seen. The findings of studying the elemental composition in various areas prove their single-phase pattern.

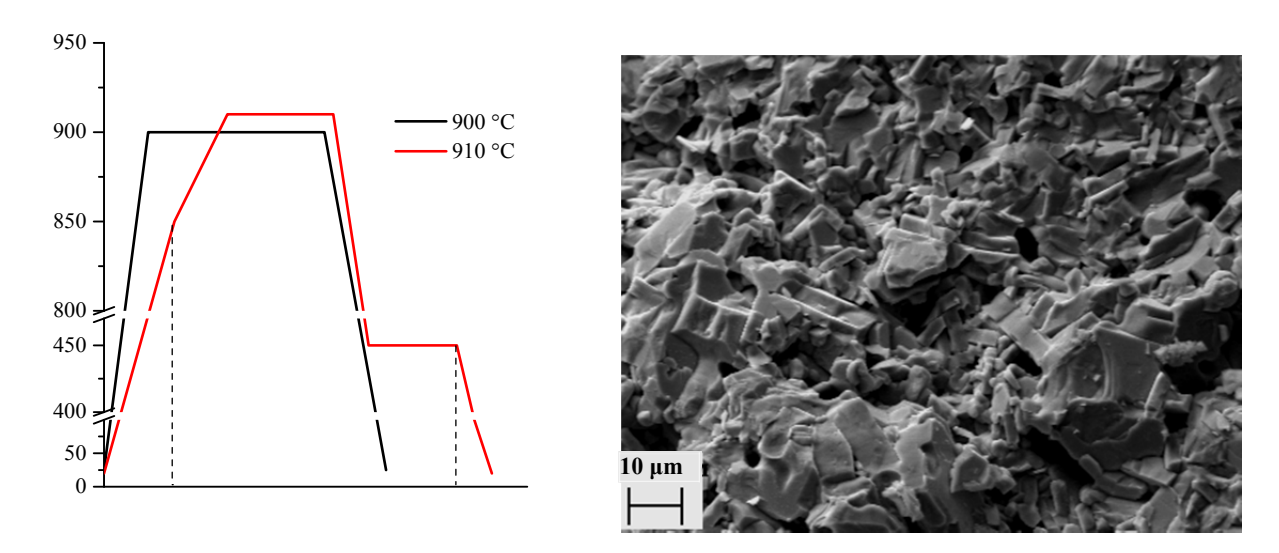


Fig. 1. Diagram of sintering conditions and morphology of YBCO compound after sintering at 910 °C

Diffraction analysis was carried using SIEMENS D-500 diffractometer equipped with a low-temperature cryostat. The sample was loaded at the room temperature and then cooled down to nitrogen temperatures. The survey was carried out on a single-crystal silicon wafer with sample cuvette a sized 15×20 mm. Scanning was carried out using $CuK\alpha_{1,2}$ X-rays in a secondary monochromator setup within the angular range of $2\theta = 5 \div 70^{\circ}$ with an interval of 0.02° and 12-second exposure at each point. Lattice parameters were estimated using High Score plus software. The morthology determined with the help of ASPEX Express scanning electron microscope based on Omega Max EDX detector. The Raman spectra of samples were analyzed using Ntegra Spectra (NT-MDT) atomic force microscope (Raman mode). The electrical resistance of samples was measured in the automated setup by the standard 4-probe method on rectangular samples within the range of 84–300 K temperature using Keithley 2002 digital multimeter. Conductive silver paste was used to attach copper leads to the samples. The temperature was recorded with a copper-to-constantan thermocouple. The rate of sample temperature change before

transition to the superconducting state did not exceed $\sim 10 \text{ K/min}$, and in the transition region $-\sim 0.1 \text{ K/min}$. The total measurement error of the samples electrical resistance did not exceed 3 %, the temperature measurement error $-\pm 0.25 \text{ K}$. The heat capacity was studied using the ac-calorimetry method within the temperature range of 20-160 K.

Findings and discussion

Figure 2a shows the diffraction pattern obtained for a microcrystalline sample of YBCO. Structure analysis findings were obtained using a crystalline structure model from ICSD (PDF-2) database No. 98-004-4113 for Pmmm space group, Y(1/2 1/2 1/2), Ba (1/2 1/2 0.18386), Cu1 (0 0 0), Cu2 (0 0 0.35501), O1 (0 1/2 0), O2 (1/2 0 0.37825), O3 (0 1/2 0.37825), O4 (0 0 0.15867). The analysis findings showed the following divergence coefficients: weighted profile $\omega R_p = 5.35 \%;$ $R_p = 3.68 \%$; "goodness of the fit" $\chi^2 = 5.4$; Bragg coefficient $R_B = 2.3$ %. The Rietveld method revealed the following of lattice cell parameters: a = 3.827533; b = 3.886522; c = 11.68327; V = 173.7979.

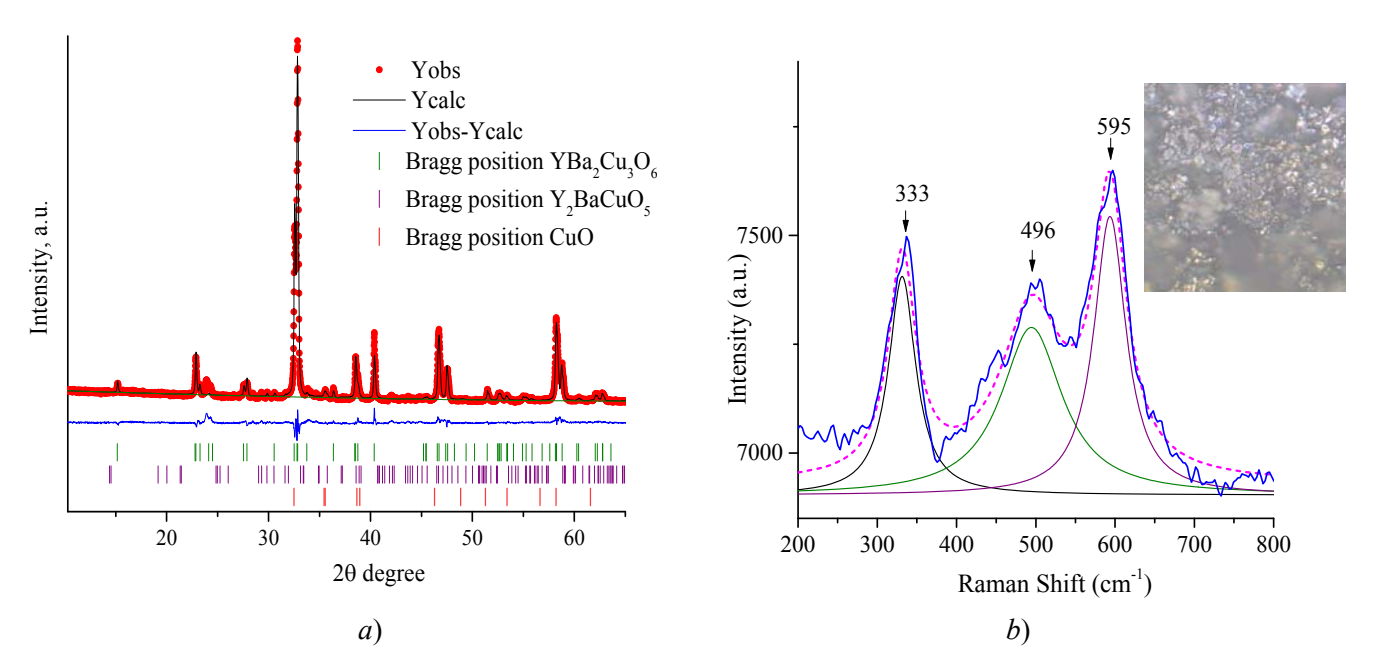


Fig. 2. Experimental (red), calculated (black) and differential (blue) diffraction patterns of the YBCO sample at a room temperature – a); Raman spectra – b). The inset shows the sample surface area sized $100 \times 100 \mu m$.

The crystallographic density of a lattice cell is $\sim 6.36 \text{ g/cm}^3$. In addition to the base peaks of YBCO, the diffraction pattern shows minor peaks corresponding to the Y-211 and CuO phases. The oxygen content is ~6.92, which is agreed to the optimal oxygen content in the YBCO structure with occupied O(1) positions in CuO chains along axis \boldsymbol{b} . Figure 2b shows the results of the Raman study with the peak positions spectra refined using the Lorentz function. The microcrystalline YBCO demonstrates vibrational modes at ~ 333 cm⁻¹ matching the vibrations of oxygen atoms O(2) and O(3) in the CuO_2 planes $(O(2, 3)-B_{lg})$ mode) and two peaks at ~ 496 cm⁻¹, which are vibrations of apical oxygen O(4) along axis c (O(4)- A_{σ} and $\sim 595 \text{ cm}^{-1}$ mode) associated with vibrations of Cu(1) and O(1) atoms [12], the peak intensity indicates the number of such cationic disturbances or breaks in the Cu-O chains. The oxygen content [13] based on the peak frequency value in O(4)-A_g expressed in cm $^{-1}$ is ~ 6.86, which is close to the value determined by the X-ray structural analysis.

Figure 3 shows the results of study $\rho(T)$ for the sample sintered at a temperature of 910 °C. The dependence $\rho = f(T)$ is metallic, the value of ρ_{300} is $4.55 \times 10^{-3} \,\Omega$ ·cm. In the range from 300 to 110 K, the temperature coefficient of resistance is $1.86 \times 10^{-4} \, \text{K}^{-1}$. The transition to the superconducting state begins at ~90.5 K. The sample contains several superconducting phases with different doping levels and has a transition width $(\Delta T) \sim 4 \, \text{K}$. The oxygen content found based on T_c (~89.2 K) is ~6,86. The relatively large peak width confirms that the sample contains superconducting phases close in terms of oxygen content.

Heat capacity values of the YBCO sample within a wide temperature range from 20 to 160 K are shown in Figure 3b. The inset shows the behavior of C_p/T around T_c , where a deviation from the common pattern can be seen below ~90 K. The range of the anomaly observed is ~5-6 K, which slightly exceeds the width of transition the superconducting estimated state by dependence $\rho(T)$. As it can be seen, the temperature deviation starts at the value of 90.2~K, which is slightly lower (by ~0.3 K)

than the start of transition in the temperature dependence of electrical resistance.

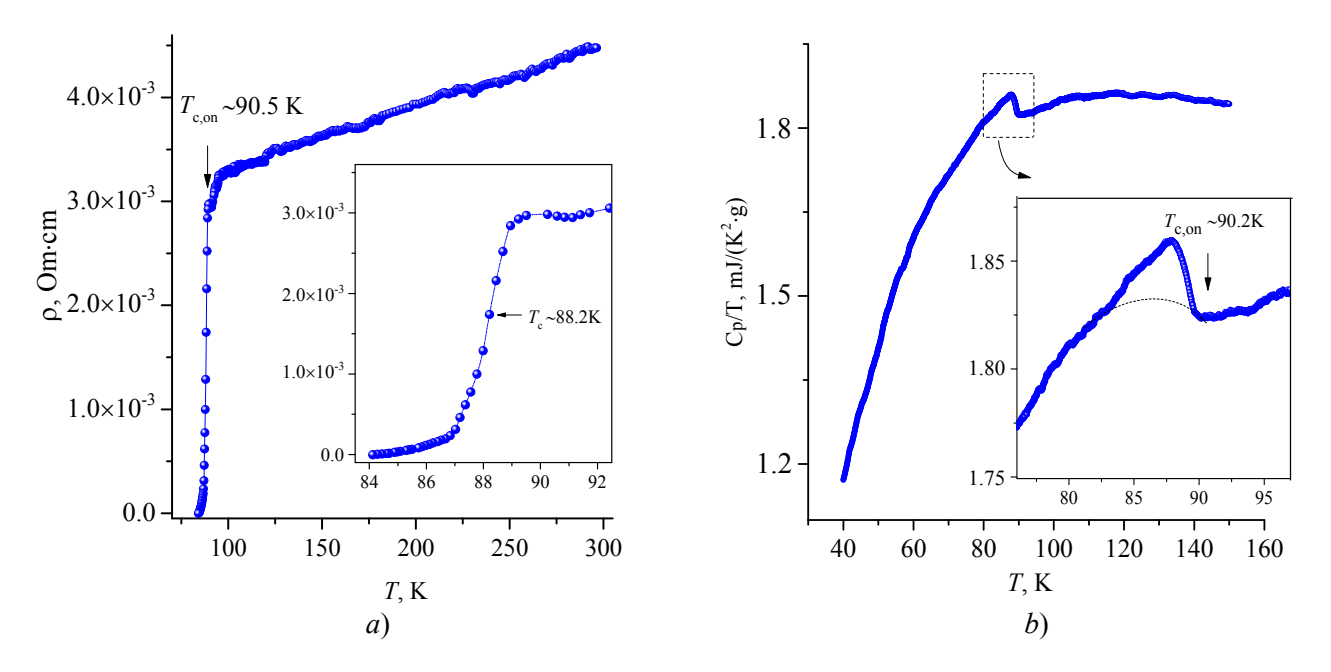


Fig. 3. Temperature vs. specific electrical resistance of YBCO - a) and heat capacity - b). The insets show the corresponding dependences in the region of superconducting transition.

This microcrystalline sample was subjected to the X-ray structural analysis in the region of transition to the superconducting state, based on the results of which structural parameters were determined in HighScorePlus software.

Figure 4 shows the temperature dependences of the electrical resistance $\rho(T)$ and $d\rho/dT$, lattice volume V and heat capacity C_p/T in the region of the superconducting transition. The transition onset at ~ 90.5 K manifests itself in all properties of this sample as an increase to the extremal for $d\rho/dT$ dependence and as a volume decrease to the minimum, which is followed by its sharp increase with an inflection point at a temperature of ~90,5 K. The maxima on dependence, temperature $d\rho/dT$ determine the value of T_c temperature during transition, within the error of estimate $d\rho/dT$,

fall on the volume striction temperatures. These temperatures with align temperature of ~89 K on the heat capacity anomaly obtained by extrapolating temperature dependence of heat capacity on low and high temperatures. The onset of the superconducting transition, which is determined by the temperature dependence of the electrical resistance, is accompanied by lattice contraction, which is followed by the volume increase in the region of T_c average values, and after the transition to superconducting state is completed, the volume change becomes insignificant.

The temperature dependence of the electrical resistance shows that it is very sensitive to thermal deformation of the lattice. The onset of superconductivity strongly correlates with the specific features of the deformation behavior of the HTS lattice.

The effects of excitation and relaxation of elementary charge excitations in the system of interacting polarized atoms [14] accompanied by the work aimed at bringing the system out of the equilibrium state and returning it to a new state after thermal exposure. According to [15], the detailed charge equilibrium in YBCO is restored as a result of distortion of lattice parameters as compared to the idealized lattice state due to redistribution of the electron density around nuclei, which is different from the electron density in neutral atoms. The stability of the crystalline structure is determined L. Pauling's which consider rules. the polarization capacity of ions [15] and their screening. The dielectric screening of local

non-uniformity of ion charges within the YBCO lattice cell is performed by changing the concentration of shared charge excitations with the lattice deformed to a minor degree [15, 16]. Lattice contraction leads to an increase in the doping level, which is indicated by the relationship [4, 17] between oxygen content and $T_{\rm c}$ value as parameter cdecreases. This contraction is explained by the energy gain during transition to the superconducting state [18]. An interesting effect observed near T_c is due to the type of electron instability [19]. Therefore, the sensitivity of the band structure of elementary charge excitations towards minor structural changes accounts for the observed high sensitivity of T_c to such structural changes.

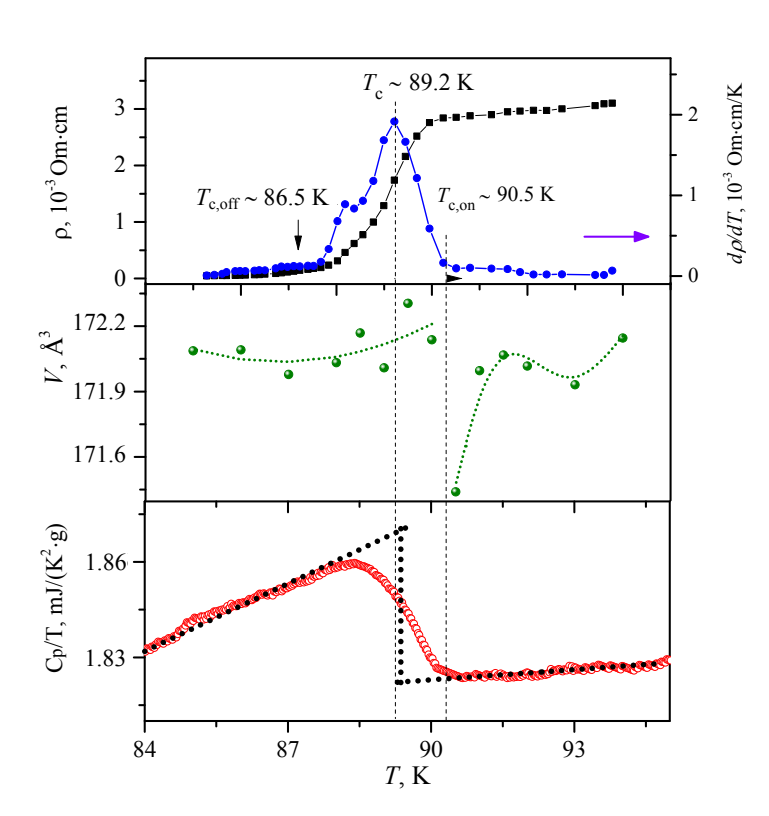


Fig. 4. Temperature dependences of ρ , $d\rho/dT$, V and C_p/T in the region of the superconducting transition

Thus, the thermodynamics of processes in these systems is directly related to the quantum electrodynamics observed during formation of elementary charge excitations by being induced, with lattice deformed appropriately.

Conclusion

This paper presents the precision X-ray diffraction analysis of the lattice thermal deformation for the YBCO sample in the superconducting state. It has been found out

that the nature of dependence ρ –T is metallic, transition to the superconducting state starts at ~90.5 K, which falls within the estimation error limits determined as a result of studying the structure and thermal properties. The onset of transition to the superconducting state manifests itself in all properties as abnormal increase to the extremal for $d\rho/dT$ and C_p/T on T dependences, and as a decrease in the specific volume to the minimum, after which it sharply increases at the inflection point, which is followed by tending to zero. It has been shown that the maxima on $d\rho/dT$ temperature dependence, which determine temperature value $T_{\rm c}$ during the transition, fall volume striction temperatures. An attempt was made to explain the transition to the superconducting state considering the specific features of HTS lattice deformation.

This work was supported by the Russian Foundation of Fundamental Research as part of research project No. 20-32-90170 and State Assignment FZNZ-2020-0002, as well as by the Ministry of Science and Higher Education of the Russian Federation (State Assignment No. 075-00269-25-00).

The studies were carried out using equipment of the Nanotechnologies Research and Education Center of the Dagestan State University. Experimental data concerning the temperature dependences of the lattice parameters were obtained at the Institute for Solid State Physics of the Russian Academy of Sciences. Heat capacity studies were carried out in the Institute of Physics of the Dagestan Federal Research Center of the Russian Academy of Sciences.

REFERENCES

1. Yazdani-Asrami M., Sadeghi A. and Atrey M. D., International Journal of Refrigeration **140**, 70–81 (2022).

- 2. Kumar S., Dahiya M. and Khare N., Applied Physics A **130** (10), 1–8 (2024).
- 3. Sivasubramaniam K., Zhang T., Lokhandwalla M. et al., IEEE Transactions on applied superconductivity **19** (3), 1656–1661 (2009).
- 4. Cava R. J., Hewat A. W. and Hewat E. A., Physica C: Superconductivity **165** (5-6), 419–433 (1990).
- 5. Benzi P., Bottizzoa E. and Rizzi N., Journal of crystal growth **269** (2-4), 625–629 (2004).
- 6. Srinivasan R., Girirajan K. S., Ganesan V., Radhakrishnan V. and Rao G. S., Physical Review B, **38** (1), 889 (1988).
- 7. Titova S. G., Lukoyanov A. V., Pryanichnikov S. V., Cherepanova L. A. and Titov A. N., Journal of Alloys and Compounds **658**, 891–897 (2016).
- 8. Talantsev E. F., Strickland N. M., Wimbush S. C., Storey J. G., Tallon J. L. and Long N. J., Applied Physics Letters **104** (24), 242601 (2014).
- 9. Meingast C., Pasler V., Nagel P., Rykov A., Tajima S. and Olsson P., Physical Review Letters **86** (8), 1606 (2001).
- 10. Menushenkov A., Journal of Synchrotron Radiation **10** (5), 369–370 (2003).
- 11. Rabadanova A. E., Palchaev D. K., Rabadanov M. Kh. et al., Herald of Dagestan State University **36** (3), 37–50 (2021).
- 12. Thomsen C. and Kaczmarczyk G., Handbook of vibrational spectroscopy, 2002, pp. 2651–2669.
- 13. Huong P. V., Bruyere J. C., Bustarret E. and Granchamp P., Solid State Communications 72 (2), 191–194 (1989).
- 14. Slater J. C., Insulators, Semiconductors and Metals. New York, McGraw-Hill, 1967.
- 15. Cava R. J., Batlogg B., Rabe K. M., Rietman E. A., Gallagher P. K. and Rupp Jr L. W., Physica C **156**, 523–527 (1988).
- 16. Bo'zin E. S., Huq A., Shen B., Claus H., Kwok W. K. and Tranquada J. M., Physical Review B **93**, 054523 (2016).
- 17. Liang R., Bonn D. A. and Hardy W. N., Physical Review B **73**, 180505 (2006).
- 18. Anshukova N. V., Golovashkin A. I., Ivanova L. I. et al., Physics of the Solid State **46**, 1394–1397 (2004).
- 19. Hardy F., Adelmann P., Löhneysen H. V., Wolf T. and Meingast C., Physical review letters **102** (18), 187004 (2009).

Aida E. Rabadanova¹, lecturer, junior research assistant

Sultanahmed Kh. Gadzimagomedov¹, senior lecturer, senior research assistant, Candidate of Physics and Mathematics

Dair K. Palchaev¹, Professor, Doctor of Physics and Mathematics

Murtazali Kh. Rabadanov¹, Professor, Doctor of Physics and Mathematics

Shamil P. Farajev¹, leading engineer, junior research assistant

Zhariyat Kh. Murlieva¹, Professor, Doctor of Physics and Mathematics

Sergey A. Mayorov², leading research assistant, Doctor of Physics and Mathematics

Gadzhimirza B. Ragimkhanov¹, assistant professor, Candidate of Physics and Mathematics E-mail: gb-r@mail.ru

Ruslan M. Emirov¹, lecturer, junior research assistant ¹ Dagestan State University.

43a, M. Gadzhieva st., Makhachkala, 367001 Russia

² Joint Institute for High Temperatures of the Russian Academy of Sciences

Bd. 2, 13, Izhorskaya st., Moscow, 125412 Russia

Submitted for publication on 1/9/2025 After revision on 1/23/2025 Accepted for publication on February 1, 2025 Scientific specialty code: 1.3.8

© A. E. Rabadanova, S. Kh. Gadzhimagomedov, D. K. Palchaev, M. Kh. Rabadanov, Sh. P. Farajew, Zh. Kh. Murlieva, S. A. Mayorov, G. B. Ragimkhanov, R. M. Emirov, 2025